Escola Tècnica Superior d'Enginyeries Industrial i Aeronàutica de Terrassa

UNIVERSITAT POLITÈCNICA DE CATALUNYA

Study of the performance of an inertial measurement unit on board a launcher

- REPORT -

Author: Xavier Laguna Benet

Tutors: Gisela Detrell Domingo (ETSEIAT),
Elena Fantino (ETSEIAT)
Collaborator: Eduard Diez Lledó (GTD)

Enginyeria Superior Aeronàutica

March 2014

Abstract

Current predictions indicate that by 2020 the available launchers will not cover the market niche of small satellites. The Aldebaran launcher is intended to cover this market niche. Aldebaran will perform an aerial launch because the initial launcher mass is significantly reduced compared with the ground launch option. Due to the navigation requirements and the precision of the release manoeuvre, Aldebaran will need a hybrid navigation system.

Aldebaran will have a strapdown navigation system on board. Gimbaled and floated systems are more precise, but they are heavier and mechanically more complicated than strapdown systems.

The sensor output error sources are modelled and the user can specify which parameters are going to be corrected by the navigation algorithm and which not. The random walk is modelled with a dynamic method. The Van Allan variance methods have not been implemented because the validation of this model in some MEMS inertial sensor is still under study.

The gravity model used in the navigation algorithm (truncated at the J_2 zonal harmonic) is a requirement imposed. However, it has been checked that this requirement is compatible with the required performance.

The sensor redundancy has been analysed. We have determined that the Aldebaran launcher will not use ISAs in a non-orthogonal configuration because the sensor output correction algorithm in this case is more complicated than in orthogonal configurations and because the detection of the failed sensor is made by probabilistic analysis.

The hybridization corrects the errors of the vertical channel instability and stabilizes it. Therefore, the implementation of an altitude sensor has been discarded because the vertical channel instability problem has been solved.

The model has been validated by three sets of tests. The first set validates the attitude determination, the second validates the INS standalone trajectory and finally the hybridization has been validated. The trajectory validation has been executed with real flight data.

Finally, the navigation system sensitivity to some parameters has been evaluated with the model. The results show that the accelerometer parameters do not have such a strong influence as the gyroscope parameters. The reason is that, in the

navigation algorithm modelled, position and velocity are corrected periodically with GNSS data but the attitude is not corrected.

The model implemented in Simulink in this project is the cornerstone of a brand new navigation system model. Such model must be able of evaluating the performance of navigation systems in a wide range of conditions and sensors.

Index

Abbreviations

ALAC	Air Launch Aerospace Corporation
CATS	Cheap access to space
CEP	Circular Error Provable
CNES	Centre National d'Etudes Spatiales
DLR	German Aerospace Center
GEO	Geostationary Earth orit
GNSS	Global navigation satellite sysem
GPS	Global positioning system
GTO	Geostationary Transfer Orbit
Gyros	Gyroscopes
HAAL	High altitude aerial launch
IEEE	Institute of electrical and electronic engineers
ISA	Inertial Sensor Assembly
IRU	Inertial Reference Unit
IMU	Inertial Measurement Unit
INS	Inertial Navigation System
LEO	Low Earth Orbit
MEMS	Microelectromechanical system(s)
MLA	Micro launcher
MRWE	Maximum random walk error
MTBF	Mean time between failures
NASA	National Aeronautics and Space Administration
RFCM	Reference frame change matrix
RFS	Reusable first stage
SFE	Scale factor error
SSO	Sun Synchronous Orbit
UAV	Unnamed air vehicle
USAF	United States Air Force

List of figures

List of tables

Scope of the project

The scope of this project is to model and validate the inertial navigation system in the context of a launcher. The model is specified for the case of the Aldebaran launcher.

The reasons why the Aldebaran launcher will carry a hybrid navigation system will be detailed. Therefore, the inertial navigation system model will be developed in the context of a hybrid navigation system. Nonetheless, the global navigation satellite system model will not be developed. The detailed hybridization between the two navigation systems will neither be developed. A simple model of the hybridization will be defined in order to correctly frame the inertial navigation model. Modelling the global navigation satellite system and the hybridization are within the scope of other GTD projects.

The main characteristics of the inertial navigation systems are going to be detailed. This project must be able of modelling any sensor that can possibly be placed on board the Aldebaran launcher.

The navigation performances will be clearly defined as functions of the mission trajectory, navigation algorithm and sensor specifications. The Aldebaran trajectory will be estimated in order to perform the sensitivity analyses with the correct trajectory input. As a result of the parametric study, the sensitivity of the navigation system with respect to each parameter identified will be analysed.

1 Justification

The project consists in a model of an INS implemented in a Matlab/Simulink environment. The model is specified for the case of the Aldebaran launcher.

1.1 Aldebaran Introduction

This project has been proposed by the company GTD in the context of the Aldebaran project. GTD is responsible of new technology studies in avionics, including electric and electronic onboard equipment. GTD must evaluate the hybrid navigation, the autonomous flight security and other navigation aspects that are not related to this project [2]. In the following pages the Aldebaran project evolution and main characteristics are detailed, as this project is part of the Aldebaran project.

Aldebaran is a system demonstrator. Its main objective is to promote, help and test the subsystem's improvements that should allow the design of one or two European next-generation launch vehicles (Figure 1). This means that the final Aldebaran launcher should permit different subsystem designs in order to test and validate these subsystem designs. The Aldebaran demonstrator will combine new technologies, new techniques and new launch system concepts. Aldebaran will replace the projects that were being developed in 2008 and should serve as a prototype for the future launcher subsystems [1]. As Figure 1 shows, the Aldebaran launcher should serve as a subsystem test bench. Then, the subsystems could achieve the category of flight proven before being delivered to the final launcher target. Nonetheless, the Aldebaran project should be profitable for the investors.

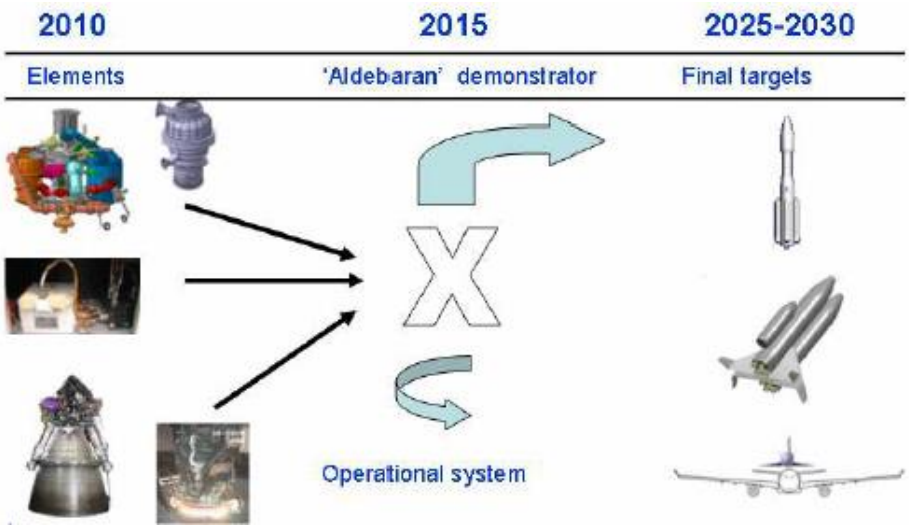

Figure 1: Aldebaran context.

The Aldebaran project is a CDTI (Spain), DLR (Germany) and CNES (France) project, but these institutions are willing to receive new partners and investors [8]. CDTI, DLR and CNES started this project with the aim of placing the European launcher industry on a privileged position among other regional industries.

It is expected that the European launchers currently used will finish their commercial life around 2025. Until then, it is expected to fill all the s/c weight and volume ranges resulting from the institutional and commercial needs with Ariane 5, Soyuz and Vega launched from the French Guiana. As the Aldebaran launcher will be just an experiment for future launchers, it should have a reasonable cost for the agencies and industries involved in the project. This is the reason why the Aldebaran launcher should be small (less than 15000 Kg). Nonetheless, the market niche of the micro and nano satellites should be covered with the Aldebaran demonstrator[1]. Figure 2 shows Aldebaran's market niche based on historical data. Figure 3 shows how there are no current or close future launchers that would cover it.

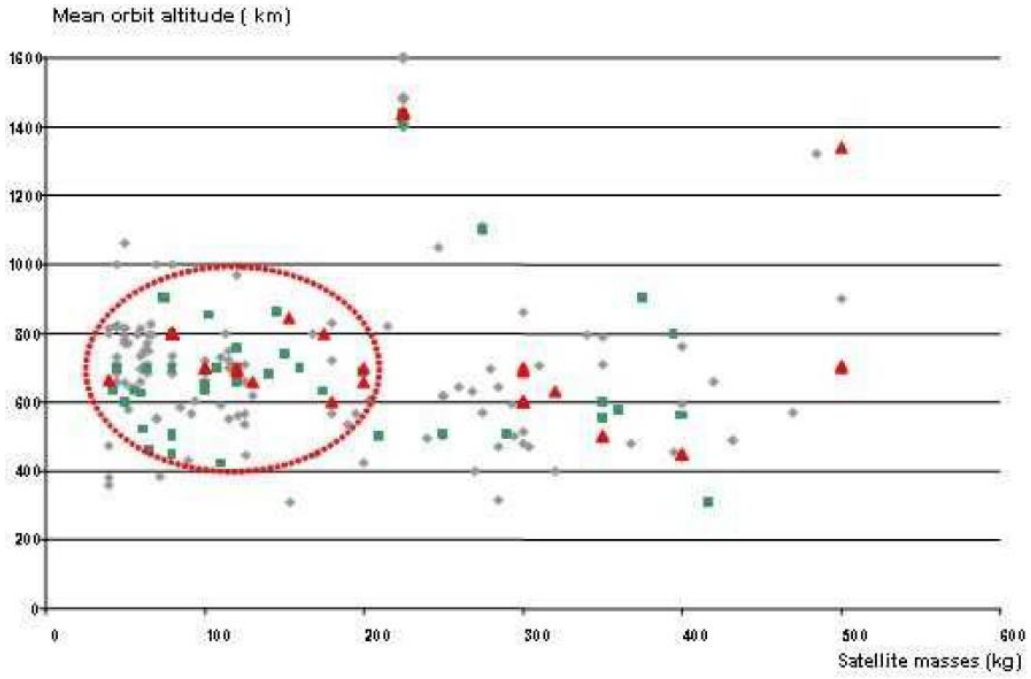

Figure 2: Distribution of small satellites launched from 1996 to 2009 by mass and altitude.

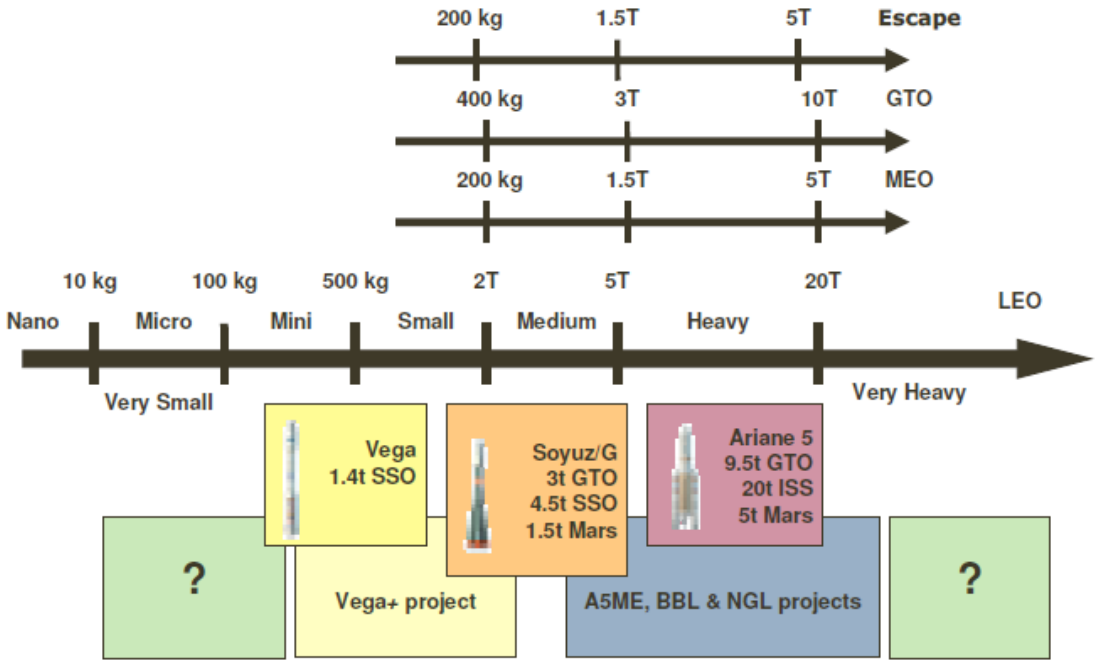

Figure 3: Current and near future domain coverage of the European launchers.

The improvements that the Aldebaran demonstrator shall provide to the next-generation launchers should be related with life cycle cost, reliability, safety, availability, operational flexibility and flight environments [1].

The launch campaign shall last less than five days, and the ground means shall be transportable as far as possible [3]. The development costs shall be less than 400 FY09€M, from the beginning of phase B to the end of the first technological flight [4]. The launch cost for different payload masses were constrained at the beginning of the project: taking as a reference a 800 Km height Sun Synchronous Orbit (SSO), the launch cost should be less than [3]:

- 2.5 FY09€M for a 50 Kg performance
- 5 FY09€M for a 150 Kg performance
- 7 FY09€M for a 300 Kg performance

1.2 Aldebaran Phase 0

Phase 0 was completed at the end of 2008 and saw seven concepts in competition. In 2009 CNES predicted the first flights for 2015. But in 2009 the financial support decreased and the project was delayed until new budgets were assigned to this project. At the time when the project was stopped, phase A was starting with three concepts out of the original seven [1]:

- **Airborne concept launched from a fighter aircraft:** The concept consists in a small airborne launch vehicle located below a combat

aircraft. Its weight should be 6 tonnes for the linear two stages launch demonstrator and up to 11 tonnes for the commercial version. The two stages launch demonstrator should be compatible with two European fighters (Eurofighter and Rafaele). The launch procedure should consist in a high-energy manoeuvre at Mach 0.5, altitude 15000 m. and a release angle of approximately 40º. Each fighter used for this concept should have their launcher operative version optimised with the fighter characteristics. The airborne launchers proposed for Eurofighter and Rafaele are shown in Figure 4. Eurofighter has the launcher connected by one point. Rafaele has the launcher weight supported by fuselage and both wings.

Figure 4: Isometric views of two possible final versions of this concept.

- **Airdropped concept launched from a cargo aircraft:** The concept consists in a linear structure with three stages. The first two stages are solid engines and the third is propelled by O_2 and CH_4. This launcher should be airdropped from an A400M. Equipped with a more powerful first stage and with few more changes, this launcher should be able to be launched from the ground. The s/c weight should be up to 200 Kg for a SSO of 800 Km in the demonstrator version and up to 300 Kg for the same orbit in the operational version. The arrangement of the launcher inside A400M is shown in Figure 5.

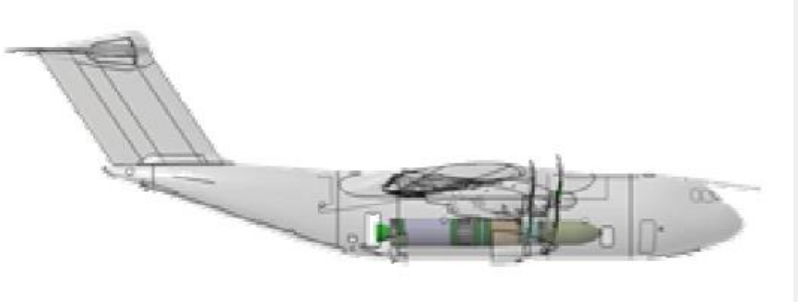

Figure 5: Lateral view of an A400M with a launcher in the payload bay.

- **The Dedalus concept air launched from a UAV**: This concept has two variants. The first variant consists in a new UAV with two booms and two tails. The UAV has two engines in nacelles on the top surface of the wing. The launcher has three solid stages. It is connected to the UAV with a Pendulum support under the UAV. The separation should be done at 0º inclination angle. This concept should place a satellite of 150 Kg in a LEO orbit. This variant is shown in Figure 6. The second variant consists in a commercial UAV (GH block 20) and launcher similar to the first variant launcher. It should be able to place a satellite of 60 Kg in a LEO orbit.

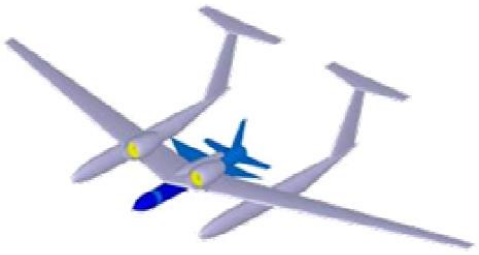

Figure 6: Isometric view of a possible final configuration of the Dedalus concept air launched from a UAV.

- **A Reusable First Stage (RFS) + Kick stage:** This concept consists in a reusable first stage capable of braking in the air and landing without propellant. This means that the first stage should be able of gliding and landing. Nowadays the first stage uses some propellant for the fly-back and for the descent. With this method all the propellant could be used for the acceleration of the kick stage.
- **Infinity concept:** This concept consists in a three-stages launcher. The first stage uses methane and liquid oxygen propellants. The first stage has multiple ceramic chambers in order to ensure capability, controllability and high flight rate. The multiple nozzles corresponding to the multiple ceramic chambers can be seen in Figure 7. The take-off is in vertical position. The descent and landing are also done in vertical position.

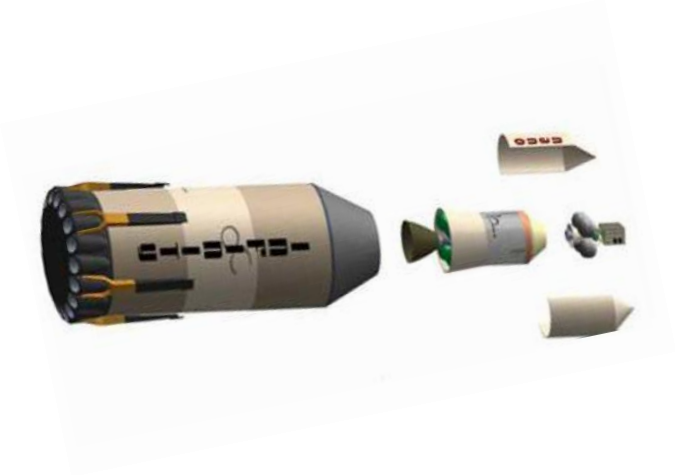

Figure 7: Isometric exploded view of the Infinity concept launcher.

- **The Cheap Access To Space (CATS) concept:** The concept consists in a two-stage-to-orbit vehicle with liquid oxygen and methane for both stages. The first stage is reusable. The first and the second stage should have many similarities in order to reduce production costs. The ground equipment should be as reduced as possible for the launch campaign in order to allow mobile ground facilities.
- **The Flexito concept:** The concept consists in three linear stages. The first stage uses two engines, as can be seen in Figure 8, and should be as reusable as possible. The second and third stages are solid propellant engines.

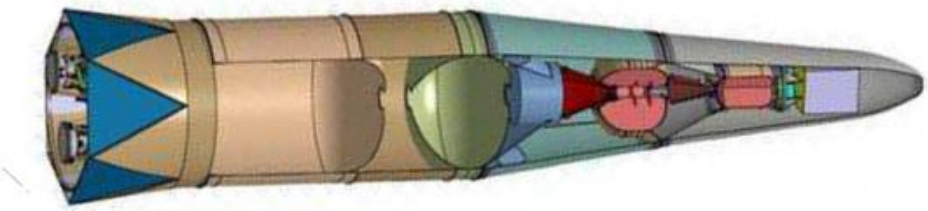

Figure 8: Isometric view of the Flexito concept launcher.

Finally, the different concepts were evaluated with the weighted criteria shown in Figure 9.

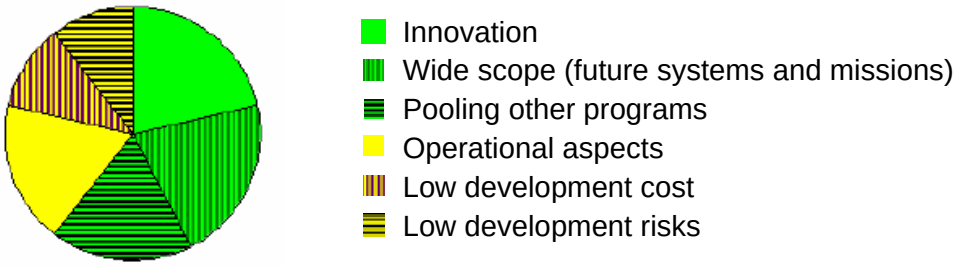

Figure 9: Aldebaran selection criteria and their weight.

With the results of the analysis done to the concepts previously mentioned, a study was made in order to determine the initial launcher mass for different launch options. The result of that study was an estimated initial launcher mass for each launcher as a function of the release angle, as can be seen in Figure 10. The final target orbit was in all cases a LEO. The payload was a 300 kg satellite in all cases[1].

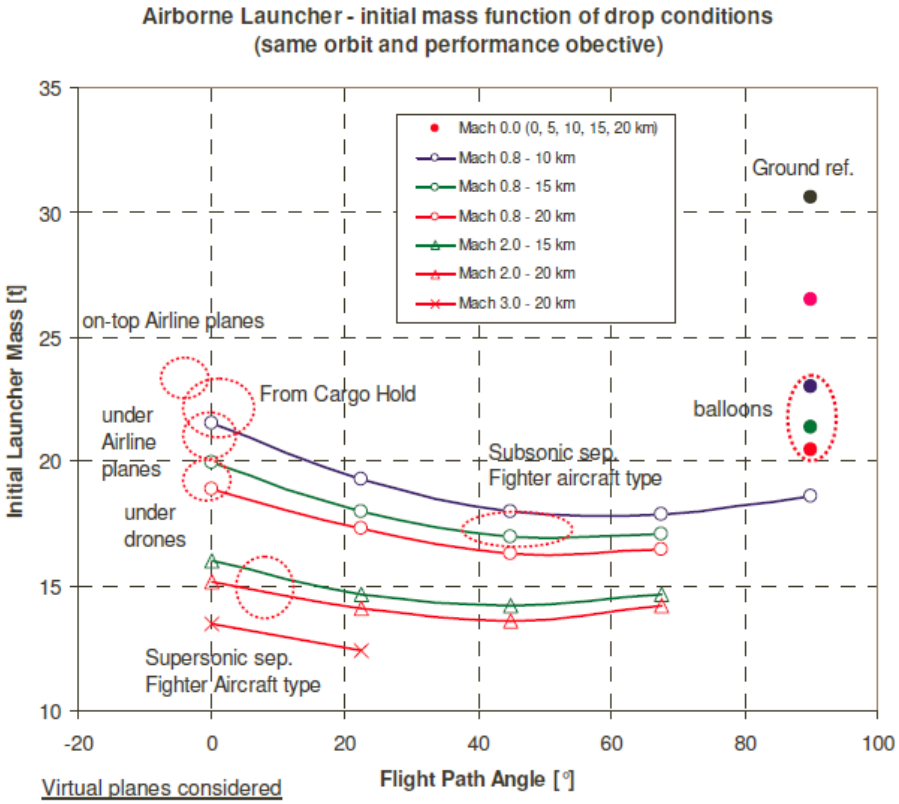

Figure 10: Initial launcher mass as a function of the launch method and the release angle.

It must be added that the lower three curves from Figure 10 are made with some information of the Ishim project [3]. This Russian-Kazakh project intended to place the launcher under a modified MiG-31. This project intended to give service to the same satellite market niche as the Aldebaran project. This project and a similar

one (Dianna-Burlak or HAAL-High Altitude Aerial Launch) were discarded because it was considered that it would be more profitable to develop launchers for heavier satellites. In the Aldebaran project the supersonic release options were not studied because they didn't fit the development target cost.

1.3 Conclusions of Phase 0

The final conclusions of phase 0 were the following [1]:

- The airborne and airdropped concepts are well adapted to the Aldebaran requirements. The main advantage of these options is the important reduction of the expandable launcher mass, up to 50% (Figure 10). Furthermore, they allow the possibility of a European launch site due to the elimination of the launch pad. The mission flexibility and the previous advantages could imply a reduction of the fixed and variable costs. The Dedalus concept air launched from an UAV was discarded due to the lack of the needed UAV in short and medium terms.
- The ground launched concepts with reusable parts were discarded due to the low technical and financial viability of fitting such concepts with the Aldebaran requirements. But the CATS concept was found interesting without the reusability capability. So, the concept was renamed Vertical Ground Lift-off Expendable concept.

Figure 11 shows the main steps to be executed in phase A. Although in the figure the different tasks are in parallel, it can be seen that the depth of the studies are quite different [1].

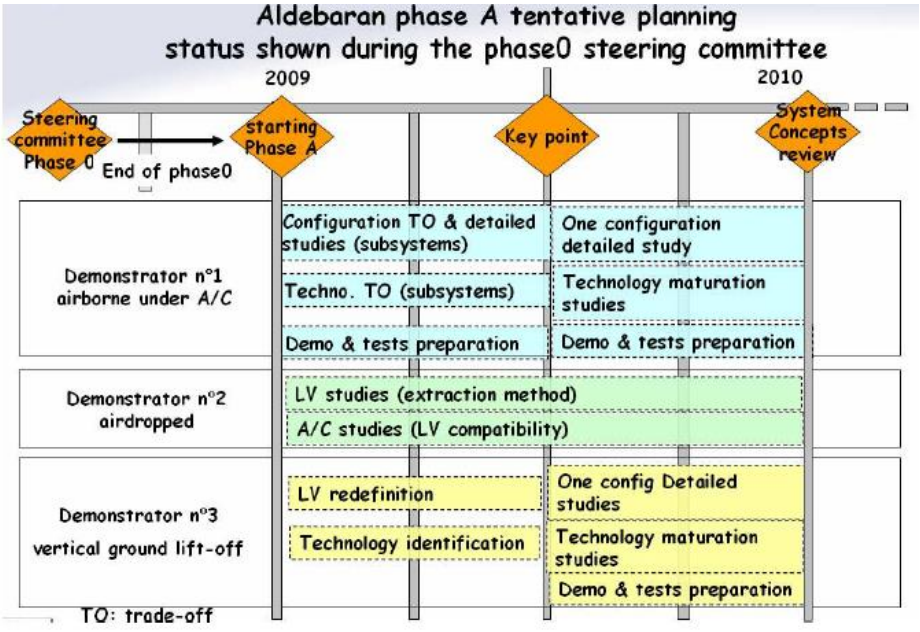

Figure 11: Tasks to be done in phase A.

The main efforts are going to be done in the concept of an airborne launcher launched from a military aircraft. The first stage will use new propellants (still to be developed) and the upper stage will use methane. This concept cannot go to the next project step if the critical subsystems have not been developed in detail [1]. One of these critical subsystems is the INS-GNSS.

The INS system modelling is one step needed in this context in order to finally reach a whole navigation system model. This is the reason why this project has been done. The model developed in this project uses GNSS data in the INS loop. However, this GNSS data are obtained using an inaccurate GNSS model. Another project has to be done in that way in order to complete the INS-GNSS hybrid model.

As a second option, the safety and operational aspects in the extraction phase in the airdropped concept launched from a cargo aircraft context are going to be analysed. The flight between the drop and the main engine ignition has to be studied in order to determine some safety aspects as the ignition delay time (drop time-ignition time). Furthermore, the detailed study of the same critical subsystems than in the previous concepts must be done [1].

As a last option, the conventional vertical ground lift-of expendable solution has to be considered. It is going to be studied just as a last option because the costs are high and the number of innovating systems is smaller than in previous concepts.

In this project an INS is going to be modelled and validated as needed for the development of the Aldebaran project.

2 State of the art

2.1 Reasons to do an aerial launch

Launching space vehicles from air has always been considered an interesting alternative to ground launches. This is why tens of projects have been started in order to perform an aerial launch. The reasons of this kind of launch can be deduced from the equation that defines the ΔV budget:

$$\Delta V_{need} = V_{end} - V_0 + \int_0^t g \sin(\gamma)\, dt + \int_0^t \frac{D}{M} dt - \omega_E R_E \cos(\varphi) \cos\left(a - \frac{\pi}{2}\right). \quad \text{Eq. 1}$$

Where:

- V_{end} is the final launcher velocity in inertial reference frame
- V_0 is the initial launcher velocity in inertial reference frame
- g is the gravitational acceleration
- γ is the flight path angle
- D is the magnitude of the drag
- M is the launcher mass
- ω_E is the angular rotation speed of the Earth
- R_E is the Earth's radius at the launch site
- φ is the latitude of the launch site
- a is the launch azimuth

As it can be seen in Eq. 1, the two factors that penalize in a launch are gravity and drag. The factor that penalizes more is gravity. If one focuses in the corresponding term, it can be seen that γ and time determine the drawback. Therefore, one can think that turning the launcher into a horizontal position just after the launch would be a good idea. But then, the drag losses would increase a lot. As a result, the launcher trajectory has a γ that depends on height. The losses due to gravity for most launchers are between 1 and 1.5 Km/s. The losses due to drag are approximately 150 m/s. Another penalization related with drag that does not appear in Eq. 1 is the maximum dynamic pressure. The launcher structure has to be sized in order to resist the maximum dynamic pressure. The maximum dynamic pressure in a ground launch occurs at the very beginning (it takes 50 seconds to reach the maximum dynamic pressure in a typical launch from ground) [9].

The air density decreases with height. As a consequence, drag decreases and so does the dynamic pressure. Therefore, the time that the launcher is

approximately in vertical position is reduced. Consequently, if the launch is done from the upper atmospheric layers ΔV_{need} decreases.

$$m_0 = m_{end}\, e^{\frac{\Delta V}{I_{sp} g}} \qquad \text{Eq. 2}$$

As can be seen in Eq. 2, the initial launcher mass increases linearly with the final mass, it increases exponentially with ΔV_{need} and it decreases exponentially with I_{SP}. It must be said that Eq. 2 cannot be applied to the multistage case, but must be applied to each stage.

Launching a space vehicle from the air reduces the initial launcher mass by reducing its structure weight and reducing the needed ΔV. However, it has also some drawbacks: the operations are quite complex and the project developments cost increases a lot if the transportation vehicle has to be designed. This is why most projects with the aim of performing an air launch took a given aircraft or designed a small modification of an existing aircraft to transport the launcher.

The project Diana-Burlak (also known as High Altitude Aerial Launch) tried to use a Tupolev Tu-160 to transport the launcher to 14000m and M 1.7. The aim of the project Ishim was also to perform a launch at high altitudes and at supersonic speeds. Both projects were mainly Russian projects and were developed in the nineties. Due to the difficulties of doing such complex launches, the projects were discarded.

Another concept was then proposed. The height and velocities required for the launch were reduced and it was thought to release the launcher from the cargo bay of a military aircraft. The first idea of that kind was to release the launcher from an Antonov An-124 Ruslan.

Most projects that intended to do an aerial launch did not reach advanced development stages. However, one project reached the commercial use stage and some may become reality in medium terms.

2.2 PEGASUS

Pegasus was the first air-launched rocket to place satellites into orbit. It was also the first winged vehicle to accelerate until Mach 8. Pegasus was developed and built by Orbital, a North American company. The first version was improved in order to fulfil the NASA and the USAF performance requirements [11].

Figure 12: Pegasus XL under the "Stargazer" L-1011 Carrier Aircraft in a take-off.

The launcher is placed under an aircraft especially designed with that aim as can be seen in Figure 12. Figure 12 shows this plane with Pegasus placed under the fuselage in the take-off manoeuvre. In order to make the inversion profitable, the plane has been used for testing some other Orbital products. It has also been used for research experiments using the unique external hook system. This system provides power, data link connection, video monitoring and telemetry transmission [11].

However, it has a little handicap when compared to other launchers. For a polar circular orbit of approximately 800 Km height the accuracy values can be seen in Table 1.

Launcher	a [Km]	e [-]	i [º]	Ω [º]
Pegasus XL	± 45	-	0.15	-
Ariane 5	± 2.5	$3.5 \cdot 10^{-4}$	0.04	0.03

Table 1: Typical accuracy values for Ariane 5 and Pegasus for a polar circular final orbit of 800 Km height [11] [9].

Table 1 shows that Pegasus has less accuracy than Ariane 5. However, other launchers that replaced Pegasus do not offer a higher accuracy. As a consequence, the fact that it has not been used since 2008 is probably due to its operation costs, not to a lack of accuracy [12].

The data related to position, velocity and attitude were sent to the airborne launcher just before the release operation. The on-board computers were also initialized from the carrier aircraft [11].

2.3 AIR LAUNCH AEROSPACE CORPORATION (ALAC)

This project was created in 1998 in order to develop and build a faster, better and less expensive satellite insertion option. The ALAC Corporation was created in 2010. The concept is to launch the Russian rocket engines from the Antonov-124-100. Its market niche is between medium and heavy space vehicles in LEO and even small scientific satellites on escape trajectories [14].

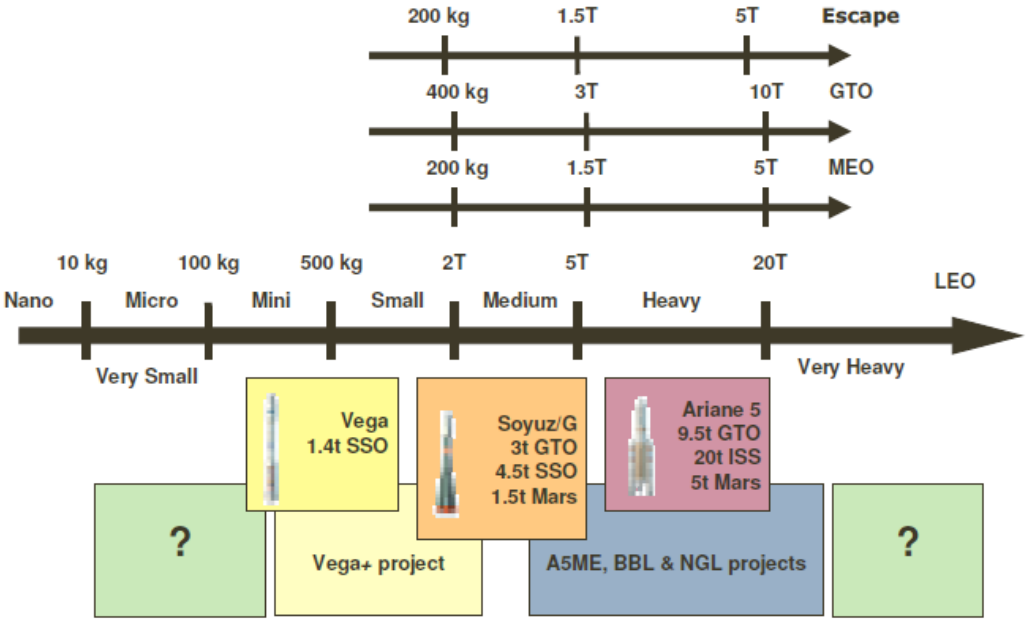

Figure 13: Current and close future domain coverage of European launchers.

As it can be seen in Figure 13, this market niche is covered by other launchers. However, the ALAC launcher has advantages over them. The main advantage of this project compared with other launchers is the target cost. While Ariane 5 costs are approximately 16-17 13M€/tonne per launch, this project costs are 11-12 13M€/tonne per launch (both to GTO) [13].

The launcher deployment is quite unusual. The launcher has the nose pointing to the Antonov tail as can be seen in Figure 14 [14]. Figure 14 is an illustration that shows the launcher inside the Antonov.

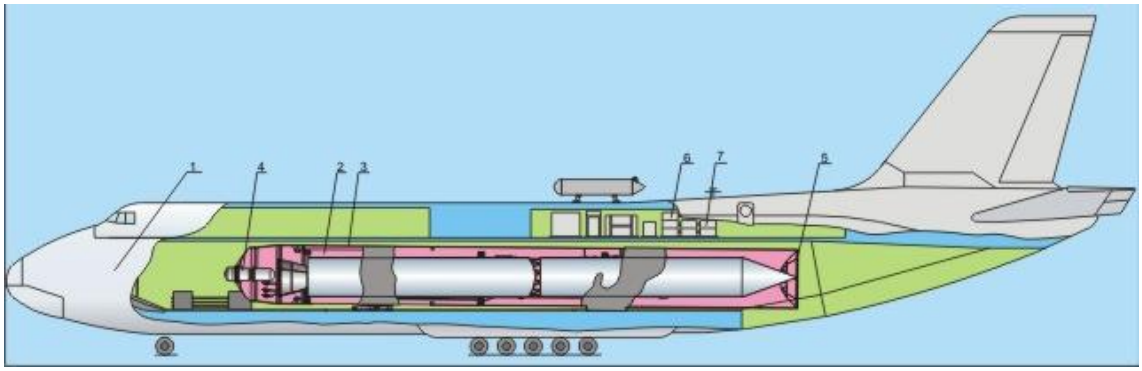

Figure 14: Scheme of the Antonov-124-100 with the launcher inside[14].

The release operation starts with the aircraft in an ascending path. At 11000m, it opens the cargo bay doors and the launcher is shot at 30 m/s relative to the aircraft. Then the launcher turns up while it ignites the first stage [14]. This manoeuvre can be seen in Figure 15.

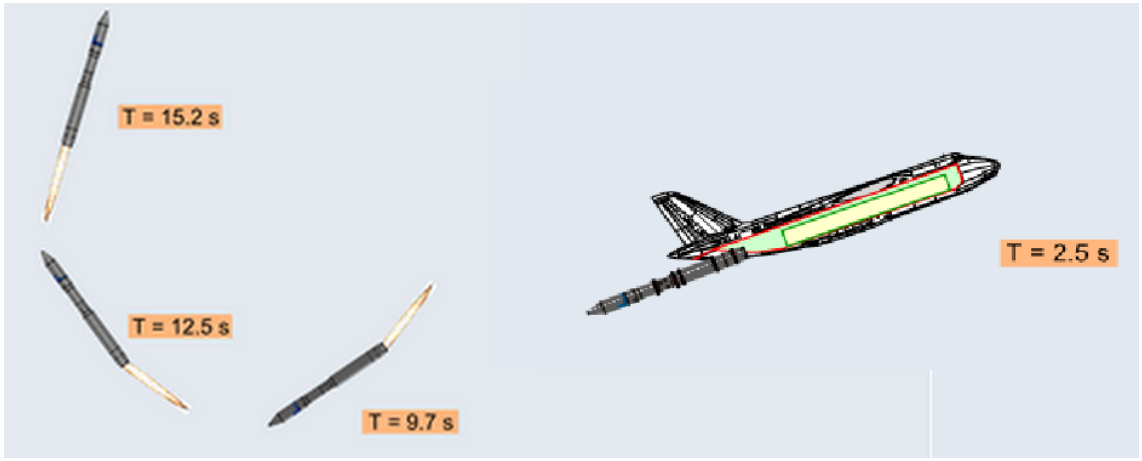

Figure 15: Release operation scheme.

The first flight was scheduled for 2010, but due to technical delays it was postponed until 2013. In 2013 the first test flight could be done in the Biak launch site (Indonesia). However, the release operation did not fulfill the safety requirements. Therefore, the first test flight has been postponed until 2017, when it is expected that the safety issues will be solved [13].

3 Specifications

3.1 Aldebaran mission profile

In this part the Launch Vehicle is going to be briefly described. The objective of the following pages is to enable the understanding of the main navigation requirements and particularly, the INS requirements.

The way the launcher is attached to the combat aircraft is an important issue to consider. It can determine the launcher main concept. For example, in Figure 16 it can be seen that the first stage changes as the attachment points change. Furthermore, the attachment point/points depend on the launcher mass and the fighter aircraft used [1].

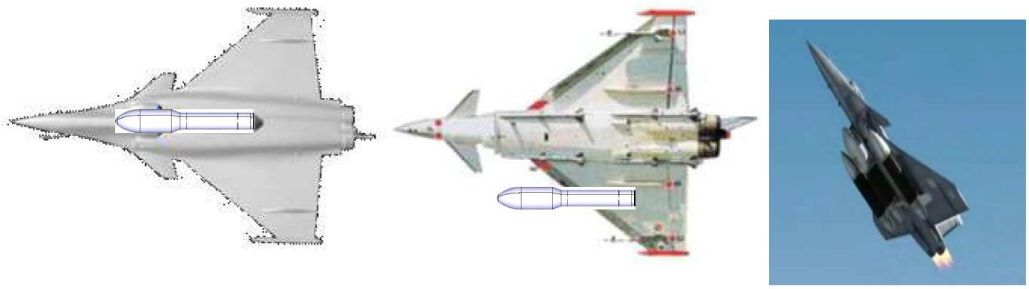

Figure 16: Different possible configurations. In the left and middle configurations the launcher is a three linear stages configuration and in the right configuration the launcher is in its Triman configurations (the first stage are two solid boosters situated in parallel with the second stage) [1] [7].

Some wind tunnel tests have been performed in order to determine the feasibility of some possible Airborne Micro Launcher (MLA) options [1].

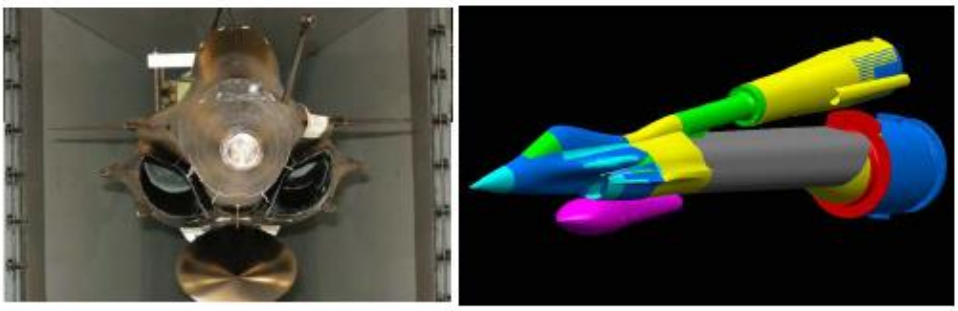

Figure 17: View of the wind tunnel experiments (left image). Isometric view if the wind tunnel experiment configuration (right image). Both images correspond to Rafaele tests[1].

It has been decided that the demonstrator is going to be developed as shown in the left and centre images of Figure 16, but during the detailed design it should

be taken into account that the commercial final launcher may use a Triman configuration [3]. The Triman configuration permits a 9t launcher without inflight refuelling and an 11.5t launcher without refuelling. This Triman configuration uses a parallel first stage and a second and third stage similar to the demonstrator configuration. The demonstrator would weight around 4t (according to CNES) or 6t (according to EADS-CASA/DLR) [4]. The demonstrator main distribution while it is under the fighter is shown in Figure 18.

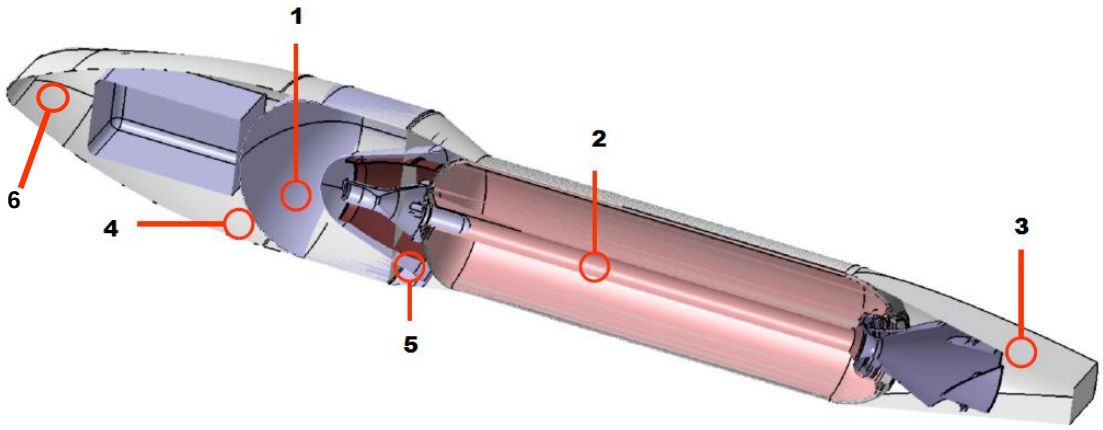

Figure 18: Launcher that is going to be developed. 1- Upper stage 2- First stage 3- Fairing 4- Miniaturised avionics 5- New pyrotechnic systems 6- Payload fairing

The first stage uses a solid propellant booster with a 2 to 3t loading [4]. The upper (second) stage can use a bi-liquid propellant engine of 5 to 10 KN. The propellant weight of the upper stage will be approximately 500 Kg [3]. This stage uses a liquid oxygen/hydrocarbon combination. Hydrazine and other toxic fuels have been discarded in phase 0 and hydrogen did not fit the launcher volume. Regarding the upper stage, there are many disruptive studies, and the targets mass and volume for the avionics and specifically for the INS have not been fixed. Nonetheless, there is the intention of an intensive usage of MEMS [4]. Furthermore, it is expected that the requirements on the sensor technology will rise in next generation launchers. Although the Aldebaran demonstrator would not need those requirements, following the aim of the Aldebaran project, it has been decided that the sensor development will not stop once the Aldebaran requirements are fulfilled. The requirements for the sensor technologies have not been yet decided [5].

The external dimensions are shown in Figure 19, where the launch configuration, with an aerodynamic fairing and a wing is also represented[5].

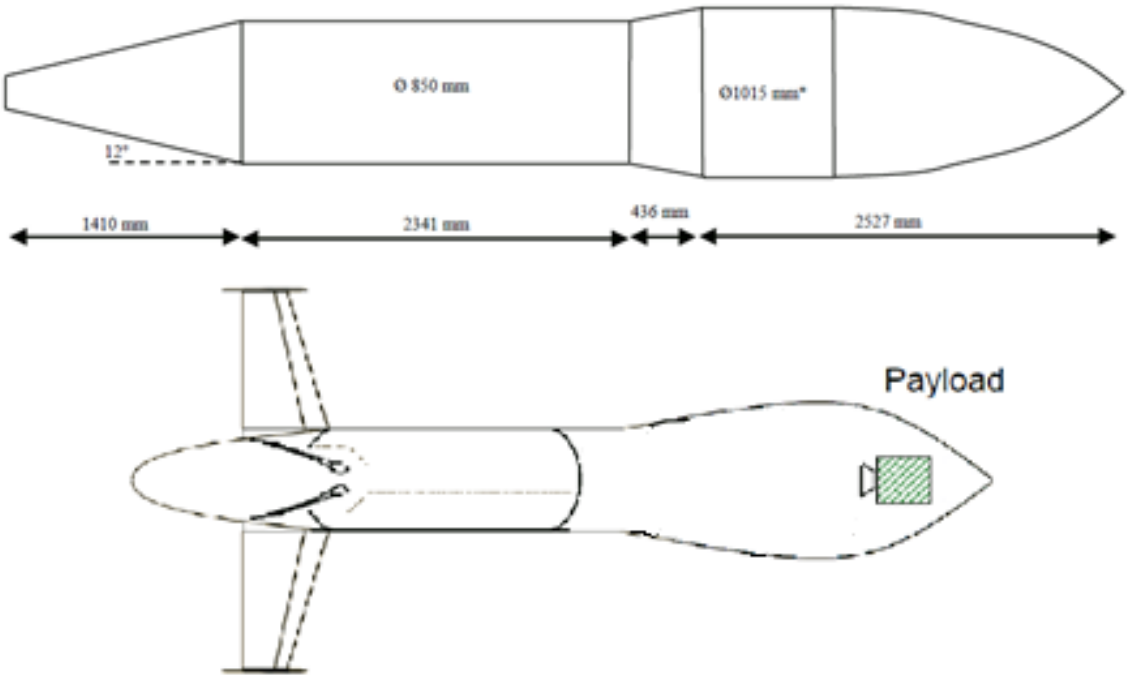

Figure 19: External envelope of the AML and sketch of AML drop configuration.

The mission starts with the fighter take-off from an airfield equipped with a specific ground segment (transportable). The mission profile can be seen in Figure 20 for the Triman configuration. In the demonstrator case, the first stage would replace the first and second stages of the Triman configuration as it can be seen in Figure 20 on the right [4].

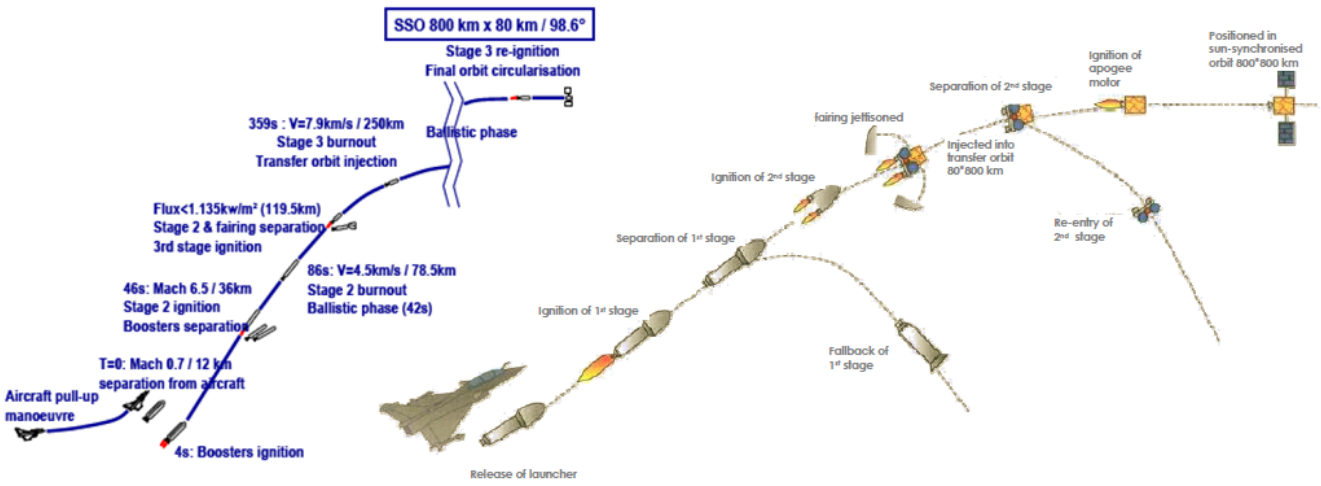

Figure 20: Triman trajectory sequence (left). MLA demonstrator trajectory sequence (right).

In the demonstrator release operation, the fighter aircraft is flying at Mach 0.8, at about 40º fight path angle and above 15 Km altitude. CNES disagrees with the

flight path angle definition, and determines that the optimum release flight path angle is >45º [5].

An altitude profile has been approximated for the Triman configuration as can be seen in Figure 21. Unfortunately, there is no such kind of graphics for the environmental factors. Particularly, the acceleration plot would be a good input for this project. Nonetheless, it has been estimated that the worst accelerations would be in the upper stage with a value smaller than 10 g[7].

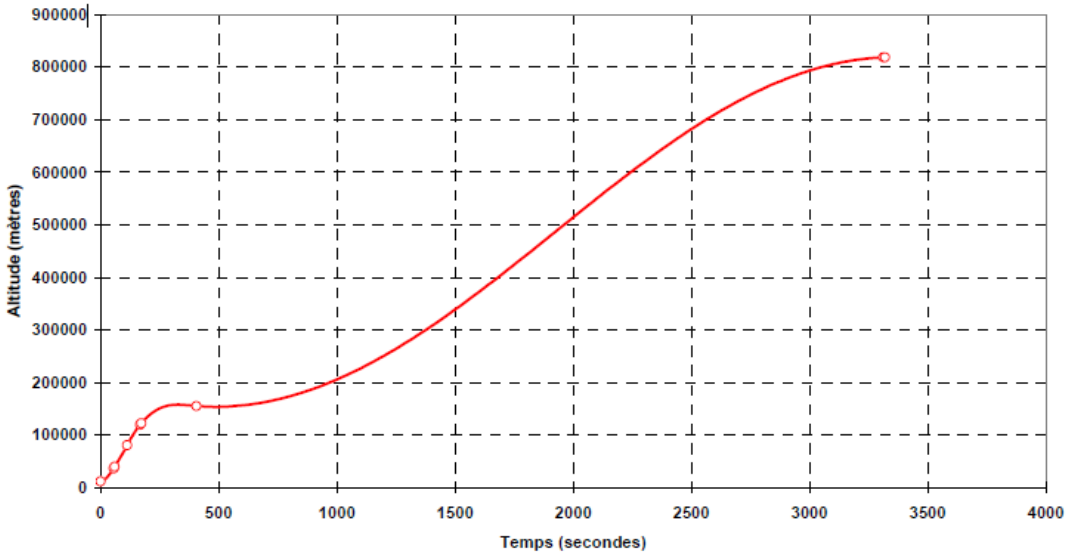

Figure 21: Altitude as a function of time.

It must be added that some acceleration studies have been done, but just for some specific future launcher variations. The engines used in those configurations produce less axial accelerations (6.5 g) than the previous mentioned estimated maximum for the demonstrator (10 g) [6].

In Triman and demonstrator configurations, the loads analyses have been done in order to ensure the viability of the concept. In the worst case (Triman configuration and aborted launch) the analysis showed that the limit loads are not reached by far [4].

Four take-off locations have been found suitable for the MLA concept [5]:

- Mont de Marsan, France for SSO inclinations
- Kourou / French Guyana for every direct inclinations and SSO
- Gran Canaria, Spain for medium inclinations to SSO
- Andoya and Svalbard, Norway for high inclinations to SSO

The mission profile determines the maximum accelerations that the INS should measure. Being air launched is a handicap for a launcher because the initial

conditions are variable and the release manoeuvre has much less accuracy than a typical ground launch.

3.2 System selection

An inertial navigation system (INS) exhibits relatively low noise and robustness from external errors, but tends to drift over time. In contrast, global navigation satellite systems (GNSS) errors are relatively noisy and sensitive to external effects, as multipath and jamming, but exhibit no long term drifting and bounded errors. Although GNSS provides a deterministic solution for position and velocity, it presents some shortcomings, such as low data rate and lack of attitude information. Inertial navigation systems, composed by accelerometers and gyroscopes, provide complementary characteristics to those of the GNSS since they have high data rate, and the availability of attitude and attitude rate.

Inertial navigation systems currently used could be replaced with less accurate inertial navigation systems when a GNSS signal is continuously available in order to bound the inertial system drifted and biased errors. A less accurate inertial system means less costly and lighter avionics systems. The hybrid light-weight navigation system will provide the following benefits:

- The inertial navigation information allows the GNSS tracking loops to work in a narrower bandwidth, so that performance improves in jamming environments. Moreover, outside jamming environments, INS data provides high bandwidth accurate navigation information in situations where the GNSS-only solution would be subjected to signal-loss or lack of availability.
- INS position and velocity information reduce reacquisition time after a GNSS outage. Therefore, the GNSS acquisition frequency can be increased and the requirements regarding the INS can be reduced.
- Low noise inertial systems can have their bias errors calibrated during the mission by means of integrating GNSS measurements. As a consequence, the calibration conditions requirements can also be reduced.
- As the INS is the core of the navigation system, there is not a required minimum number of visible satellites to use GNSS.

The current inertial navigation units present a high performance in terms of bias, scale factor and precision. On the other hand, these high performances have great impact on equipment weight and cost. The Aldebaran avionics technology survey indicates that the architecture that would best match the navigation requirements preserving the specified performances, while respecting and

improving as well the weight constraint, is based on navigation hybrid architectures. The hybridization approach takes advantage of the benefits provided by two different technologies: a GNSS receiver (GPS, Galileo) and a MEMS-based Inertial Measurement Unit.

The most relevant factor to be considered is that the required navigation performance is nowadays still not defined in the Aldebaran project framework. Hypothesis that common navigation performances in the aerospace domain are required is made, but no formal justification for the Aldebaran project has been provided so far. Furthermore, it is expected that the launchers legal environment or European standards will change before 2020[4]. Therefore, the required navigation performance that is going to be used in this project is an approximation provided by GTD.

3.3 System specifications

The following list of requirements has been provided by GTD. With the information presented in sections 3.1 and 3.2 , a comparison has been done with the launcher information database in order to determine the numerical values of the performance requirements. Nonetheless, it has been also taken into account that the regulatory framework will change before the beginning of the test flights.

3.3.1 Functional requirements

The Inertial Measurement Unit (IMU) model shall provide with respect to the inertial reference frame in Cartesian coordinates:

- Position
- Velocity
- Velocity increment
- Acceleration
- Attitude
- Attitude rate

The IMU model shall take into account the sensor measurement model and the IMU intrinsic errors.

The navigation function shall take into account the alignment process, the IMU model and the navigation algorithm (data pre-treatment before the IMU model and post-treatment after the IMU model).

3.3.2 Performance requirements

The navigation function accuracy with respect to an inertial reference frame in Cartesian coordinates shall provide:

- Attitude accuracy of ± 0.75° for roll and of ± 0.5° for yaw and pitch.
- Attitude rate accuracy of ± 0.5°/s for roll and of ± 0.3°/s for yaw and pitch.

The final accuracy in speed increment shall be 0.04572 m/s and in attitude increment shall be $\pi \cdot 2^{-15}$ rad.

The IMU model shall take in account the couple gyroscope and accelerometer.

The IMU gyro model shall take in account the drift, which shall be under 0.5 °/h.

The IMU gyro model shall take in account the scale factor, which shall be under 30 ppm.

The IMU accelerometer model shall take in account the bias, which shall be under 1.61 mg.

The IMU accelerometer model shall take in account the scale factor, which shall be under 300 ppm.

These requirements are not going to be checked in this project because the GNSS model and the INS-GNSS hybridization have not been precisely modelled in this project. These models are the scope of other GTD proposed projects.

3.3.3 Environmental Constraints

The gravity model used shall be a spherical harmonic expansion truncated at the truncated at J_2 term.

The geodetic model used shall be the WGS84 [26].

The navigation model shall be tested in a vibratory and bias environment.

4. INTRODUCTION TO INERTIAL NAVIGATION SYSTEMS

4.1 Inertial navigation systems generalities

The principle of inertial navigation is that the second integral of acceleration is position. This is why the inertial navigation is also called Newtonian navigation.

The accelerometers measure inertial acceleration, also known as specific force. Accelerometers do not measure gravitational acceleration. This means that an accelerometer in a free fall does not have any output value.

Gyroscopes (gyros) measure rotation. Rate gyros measure rotation rate, while displacement gyros measure the accumulated rotation angle. Gyros are very important in inertial navigation because with its output the accelerometer orientation can be known.

An inertial sensor assembly (ISA) is compound by some inertial sensors rigidly mounted to a common base. The sensors always maintain the same relative orientations. Usually the ISA is mounted with three gyroscopes and three accelerometers as shown in Figure 22.

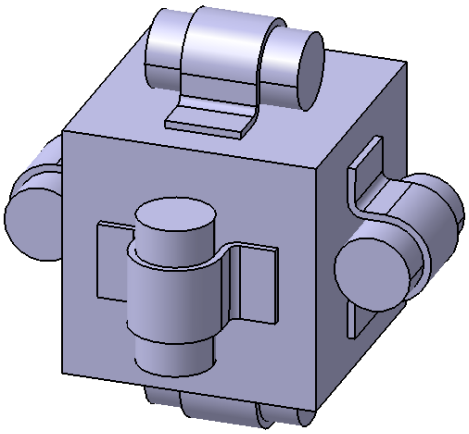

Figure 22: ISA composed by three accelerometers and three gyroscopes.

There is another common configuration; it is the ISA with only gyro sensors. This configuration is named inertial reference unit (IRU).

An inertial measurement unit (IMU) is compound by an ISA with its associated electronics for calibration, measurement, thermal control or thermal

compensation, signal conditioning and output control. Sometimes these functions require an IMU processor or gimbal control electronics for gimballed systems.

An inertial navigation system (INS) includes one or more IMUs, the power supplies, the user interfaces and the navigation computers. The navigation computers calculate the gravitational acceleration and process the accelerometer and gyros outputs in order to estimate the velocity, attitude and attitude rates of the IMU. It is important to remark for the INS-GPS integration that the INS measures the position and attitude of the ISA, while the GPS measures the position of the antenna.

The host vehicle is the platform where the INS is mounted. Even humans are host vehicles. The human body has a double navigation type. In one side, the sense of sight gives information of the position and attitude taking as reference external objects. In the other side, there is the IMU composed of the otolith organs (two dual axis accelerometers) and the semicircular canals (three rotational acceleration sensors).

The error of most INS models ($\boldsymbol{\sigma_{pos}}$) can be approximated with the equation:

$$\boldsymbol{\sigma_{pos}}(t) \approx \boldsymbol{C} \cdot \Delta t \ . \qquad \textbf{Eq. 3}$$

C is a matrix that can be experimentally estimated. Due to the complexity of the terms of this matrix, some other concepts have been used for reflecting the INS accuracy, such as the Circular Error Probable (CEP). The CEP concept consists on using an imaginary circle centred in the calculated host vehicle position. This circle has a radius such that the chance of the host vehicle to be there is 0.5. This circle radius is not constant, but increases with time due to the integration. The degradation of precision with time is quantified by the CEP rate. Before GPS emergence CEP rate was the most important parameter of the INS by difference. The denoted 'high-accuracy systems' have a CEP_{rate}<185 m/h. High-accuracy systems were the ones suitable for missile-carrying submarines and intercontinental missiles. Nowadays, with the possibility of determining the position with GPS on-board, the CEP_{rate} has lost importance.

The INS can be divided in two categories: the gimballed or floated systems, in which the ISA has been isolated from the rotations of the host vehicle, and the strapdown systems, in which the ISA is quasi-rigidly mounted to the host vehicle. In gimballed or floated systems the gimbal/float structure is also quasi-rigidly mounted to the host vehicle. Both categories need the quasi-rigidly assembly in order to isolate the ISA sensors from shocks and high frequency vibrations. This

kind of assembly is usually made with elastomers which also produce some damping.

4.1.1 Gimballed and floated systems

Gimballed systems with feedback control were first developed in the fifties, when computers were too slow for strapdown calculations and too heavy to be brought on board. In its most common configuration, using two gimbal bearings, they pose a problem, the gimbal lock. Gimbal lock occurs when the host vehicle turns around an axis perpendicular to the inner and outer gimbal axes, as can be seen in Figure 23. In this case, the INS turns with the host vehicle and the attitude data obtained is incorrect.

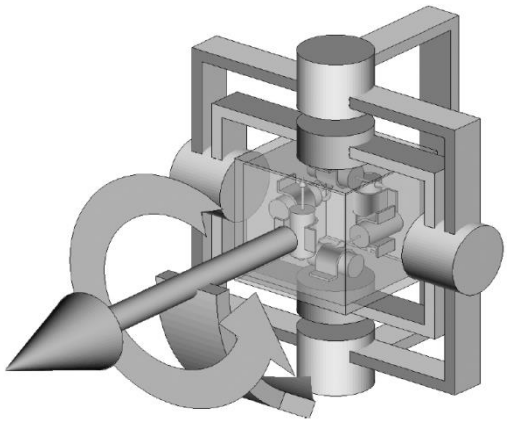

Figure 23: Representation of the gimbal lock [A-3]. When the host vehicle turns about the axis orthogonal to the gimbal axes, the ISA turns with the host vehicle.

Gimbal lock would not be a problem in case of limited attitude mobility, but in flight, this performance is not acceptable and another set of gimbal bearing must be added. This configuration, shown in Figure 24, makes the IMU much heavier (more than a 50% mass increase), more complex and less reliable.

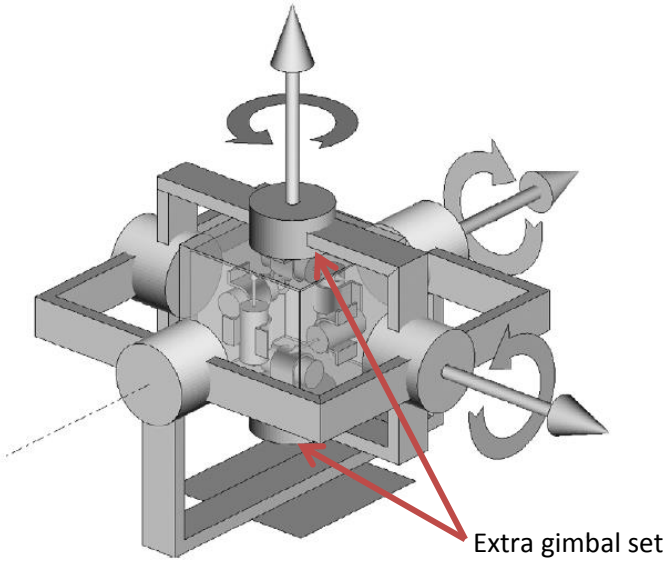

Figure 24: Gimballed system with an extra gimbal set in order to avoid gimbal lock [A-3].

Some INS use mechanical stops in order to prevent gimbal lock. But these systems present a drawback; the mechanical stops make the outer gimbal turn around its axis by 180º. With this turn, known as tumbling, the gimbal position in which the gimbal lock occurs is avoided, but the reference is lost. Then, the ISA attitude should be corrected in the INS algorithm. In precision INS the precision degradation that implies the tumbling is not acceptable.

The gimballed configuration has the advantage that it minimizes the errors coming from the sensitivity scale factor because the accelerations measured are smaller and the scale factor error depends on it. But they are expensive, heavy, big, and at high g environments the gimbal structure flexure increases the error. Furthermore, it is difficult to maintain a uniform sensor temperature. The way the power and signal transmission is done can also increase noise and error.

The floated systems are an evolution of the gimballed systems. The ISA is mounted in a bubble that is in the middle of the flotation cavity. Thanks to this, no gimbal structures are needed. Liquid thrusters are equipped in order to maintain the ISA equally oriented. These thrusters allow the system auto-calibration with gravity.

Floated systems are generally more accurate than gimballed systems. But the access is quite difficult complicating maintenance and repair. The way the power and data is transmitted through the fluid can also lead to some noise and error.

The carouseling is the implementation, for gimballed or floated systems, of a constant turning rate about one specific axis. This spin is slow (about one rpm). For gimballed systems the axis chosen is the one corresponding to the inner

gimbal axis. By doing this, long term navigation errors are reduced. The way these errors are reduced is detailed in section 4.3 . Another technique that pursues the same objective is the indexing. In this technique the rotation is made by discrete rotations, usually a multiple of 90º.

4.1.2 Strapdown systems

Strapdown systems are not isolated from the host vehicle rotation. In this case, the gimbal or floated system is replaced by a computer, which using the gyros and accelerometer data, calculates attitude and position (and their derivatives). This system is much cheaper than the previous ones. It eliminates the deflection of the gimbal structure errors, but this effect is almost cancelled by the increase in the error proportional to the sensor input, as rotation rates are higher. Compared to other systems, calibration and testing becomes more complicated and requires a larger data acquisition rate.

Carouseling is also possible in this system. For vehicles with restricted motion in the x-y plane, the ISA is rotating around the yaw axis in the vehicle reference frame (see Figure 25). In this case the error induced by the uncompensated biases of the accelerometers and gyros is reduced. Usually, the rotation is oscillatory in order to simplify the mechanism. However, Aldebaran motion is not restricted in the x-y plane. Therefore, uncompensated biases cannot be reduced by carouseling.

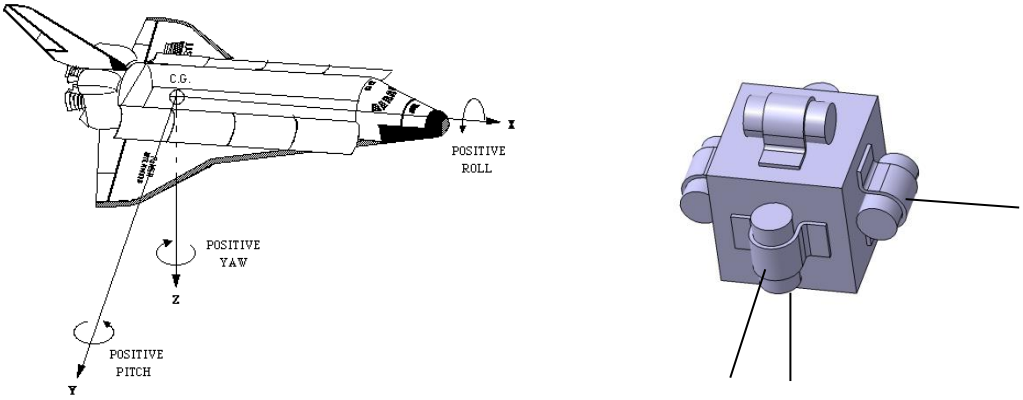

Figure 25: Representation of the axis associated to the host vehicle reference frame and the ISA motion in a strapdown system with carouseling.

Furthermore, carouseling implies the addition of a rotation bearing, a motor and the associated electronics. This drawback makes the carouseling unattractive.

4.2 Sensor signal processing

In this section, the gimballed and strapdown systems signal processing is going to be briefly detailed.

4.2.1 Gimballed or floated systems

The signal processing for a gimballed or floated INS is detailed in Figure 26.

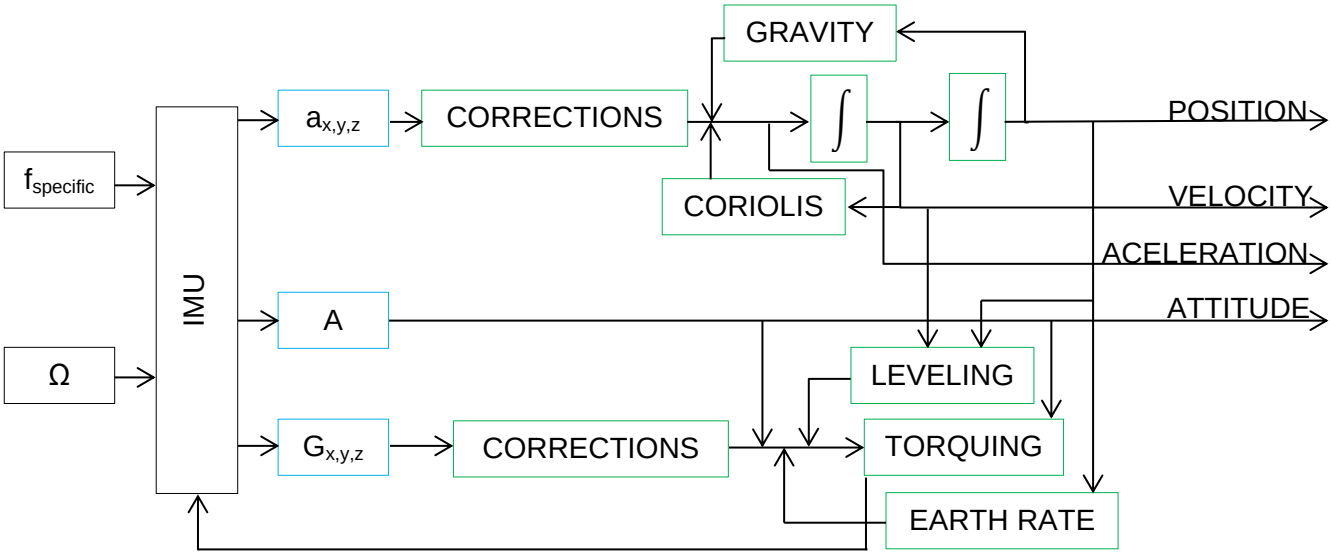

Figure 26: Basic signal processing for a gimballed system.

The INS inputs are the specific force ($f_{specific}$) and the rotation of the host vehicle (Ω). In Figure 26, the ISA outputs ($a_{x,y,z}$, accelerometer outputs, and $G_{x,y,z}$, gyroscope outputs) and the gimbal position (A) are show in blue and the processing steps are shown in green. One output of the ISA is the gimbals position, which indicates the attitude of the host vehicle.

Accelerometers and gyros outputs have a first correction corresponding to the calibration corrections. The accelerometers output is then corrected for gravity and Coriolis effect. Gravity is computed using position and a gravity model. The Coriolis effect is computed using velocity and position. The signal resulting after this corrections is the ISA acceleration. If this signal is integrated, velocity can be found and by integrating another time, position can be found. For both integrations the boundary values, the values at t=0, are necessary.

The gyros signal should be ideally zero. However, the gimbals are not ideal and the ISA attitude does not remain constant. Then, gyros signal is used for maintaining the ISA constantly oriented. Nonetheless, when non inertial reference frame is used, the motor torques are also used in order to maintain the ISA

attitude oriented according to the reference frame used. In the case of using the local horizontal reference frame, the correction due to the Earth rotation (Earth rate) and due to leveling have to be done. Both effects can be seen in Figure 27.

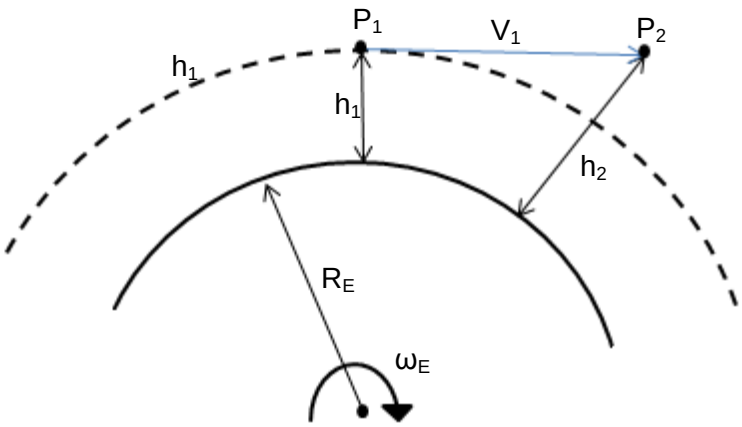

Figure 27: Representation of the Earth rotation and leveling effects.

Once the corrections have been done, the torques that should be applied to the gimbal structures are computed. In Figure 26, this computation process is called "torquing".

The initial position and velocity can be obtained by external inputs. These inputs can be user introduced data, GPS data or the output of an initialization process. Initialization processes use Earth motion to obtain the initial latitude, altitude and attitude. Latitude and altitude can be obtained using velocity and Earth rotation vector and the required initial attitude can be obtained by Earth rotation. It is advisable to use this information as a checker.

4.2.2 Strapdown systems

The signal processing for strapdown INS is detailed in Figure 28.

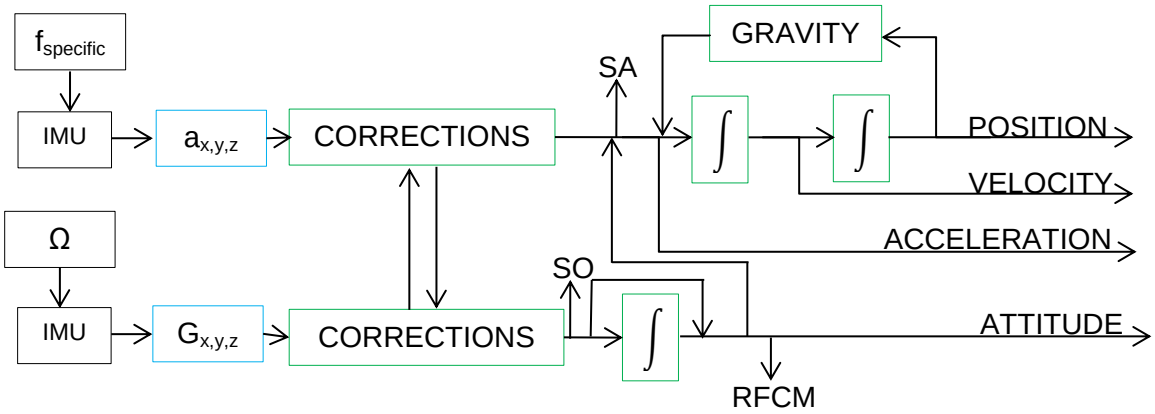

Figure 28: Basic signal processing for a strapdown system.

In Figure 28, SA stand for sensor acceleration, SO, sensor estimated angular velocity of the host vehicle in sensor angles and RFCM is the reference frame change matrix. SA and AO are used for the stabilization and control loops.

In this system the initial position, the velocity and the acceleration at t=0 are also needed. Inintial attitude is also needed, but it can be estimated from trajectory matching or by gyrocompassing. Gyrocompassing is the procedure by which the INS determines the orientation of the ISA. It must be done in stationary conditions. The accelerometers determine the local vertical vector and the gyros determine the Earth rotation vector. East is computed by the cross-product of them. At high latitudes both vectors are almost parallel and this procedure cannot be applied due to the error increase.

4.2.2.1 Reference frame change

The signal processing shown in Figure 28 can slightly change depending on the type of reference frame used to estimate the navigation data. Some examples are:

- An Earth-centred inertial reference frame can be used centred in Earth with the x axis pointing γ, the y axis perpendicular to x and contained in the equator and z positive to geographical north direction. Eq. 4 can be used to determine navigation data.

$$\left.\frac{d^2\boldsymbol{p}}{dt^2}\right|_i = \mathbf{f} + \mathbf{g}\,. \qquad \text{Eq. 4}$$

Where p stands for the estimated position, f for the accelerometers output and g for gravity.

However, if the output is to be expressed in terms of ground speed in the inertial axes, the expression slightly changes.

$$\left.\frac{d\boldsymbol{p}}{dt}\right|_i = \left.\frac{d\boldsymbol{p}}{dt}\right|_{rotating} + \boldsymbol{\omega}_{\mathrm{ie}} \times \mathbf{r}\ . \qquad \text{Eq. 5}$$

Taking into account that the movement can be separated into rotation and translation, Eq. 5 must be used for finding velocity and acceleration.
If the result is combined with Eq. 4 one can find:

$$\left.\frac{d\mathbf{v}_e}{dt}\right|_i = \mathbf{f} - \boldsymbol{\omega}_{\mathrm{ie}} \times \mathbf{v_e} - \boldsymbol{\omega}_{\mathrm{ie}} \times [\boldsymbol{\omega}_{\mathbf{ie}} \times \mathbf{p}] + \mathbf{g}\,, \qquad \text{Eq. 6}$$

where ω_e sands for the rotation rate around Earth rotation axis and v_e is the velocity respect to the Earth surface. The $\omega_e \times [\omega_e \times p] + g$ term is the

local gravity vector and is denoted by g_1. The term $\omega_e \times v_e$ is the Coriolis acceleration term. The Figure 28 signal processing with this reference frame would be modified by adding another process equal to the one corresponding to gravity in order to apply Coriolis corrections. Gravity process would also be modified by correcting not by g but by g_1. f is expressed in inertial coordinates. Therefore, the sensor output must be converted to inertial coordinates with the matrix C_b^i.

- If the same reference frame has x pointing not at γ, but at the null longitude and null latitude point, the reference frame would rotate with Earth. This reference frame is interesting for applications where the host vehicle moves near earth surface because the surface has constant position in this reference frame. By a procedure similar to the previously explained, $\dot{v_e^e}$ can be found:

$$\dot{\mathbf{v}}_{\mathrm{e}}^{\mathrm{e}} = \mathbf{C}_{\mathrm{b}}^{\mathrm{e}} \cdot \mathbf{f}^{\mathrm{b}} - 2\boldsymbol{\omega}_{\mathrm{ie}}^{\mathrm{e}} \times \mathbf{v}_{\mathrm{e}}^{\mathrm{e}} + \mathbf{g}_1^{\mathrm{e}}. \qquad \text{Eq. 7}$$

$\mathbf{C}_{\mathrm{b}}^{\mathrm{e}}$ transforms measured specific force into Earth rotating axes and is calculated by integration:

$$\dot{C}_{\mathrm{b}}^{\mathrm{e}} = \mathbf{C}_{\mathrm{b}}^{\mathrm{e}} \cdot \boldsymbol{\Omega}_{eb}^{b} \ . \qquad \text{Eq. 8}$$

Where $\Omega_{\mathrm{eb}}^{\mathrm{b}}$ is the body rate with respect to the Earth-fixed frame.

- Others systems which origin point is placed on Earth surface are used for Earth surface navigation. As this case is not studied in this project, these systems are not going to be explained. The signal processing is quite similar to the previously explained.

As signal processing will depend on the reference frame, coordinate changes will be required. There are basically three mathematical approaches to describe the attitude of a vehicle in the space:

- Direct cosine matrix is the matrix [3x3] which transforms elements from one reference system to another.

$$\mathbf{p}^{\mathrm{n}} = \mathbf{C}_{\mathrm{b}}^{\mathrm{n}} \cdot \mathbf{p}^{\mathrm{b}}. \qquad \text{Eq. 9}$$

In Eq. 9, it can be seen how direct cosine matrix transforms one vector from one reference frame to another. This matrix changes with time $\mathbf{C}_{\mathrm{b}}^{\mathrm{n}}$ (t). This change can be expressed as a matrix multiplication:

$$\mathbf{C}_{\mathrm{b}}^{\mathrm{n}}(t + \delta t) = \mathbf{C}_{\mathrm{b}}^{\mathrm{n}}(t) \cdot \mathbf{A}(t) \ . \qquad \text{Eq. 10}$$

For small rotations **A**(t) can be written as follows [A-1]:

$$\mathbf{A}(t) = \begin{bmatrix} 1 & -\delta\psi & \delta\theta \\ \delta\psi & 1 & -\delta\Phi \\ -\delta\theta & \delta\Phi & 1 \end{bmatrix}. \qquad \text{Eq. 11}$$

If this matrix is differentiated, the turn rate of the ISA frame with respect to the n frame is obtained.

$$\mathrm{d}\mathbf{A}(t) = \begin{bmatrix} 0 & -\omega_z & \omega_y \\ \omega_z & 0 & -\omega_x \\ -\omega_y & \omega_x & 0 \end{bmatrix} = \boldsymbol{\Omega}_{nb}^{b}\ . \qquad \text{Eq. 12}$$

Then, $\dot{\mathrm{C}}_{\mathrm{b}}^{\mathrm{n}}$ can be also calculated:

$$\dot{\mathbf{C}}_{\mathrm{b}}^{\mathrm{n}} = \mathbf{C}_{\mathrm{b}}^{\mathrm{n}} \cdot \boldsymbol{\Omega}_{nb}^{b}\ . \qquad \text{Eq. 13}$$

- Another way to express attitude and attitude changes is by Euler angles. Any rotation can be expressed as a combination of three turns. They are not going to be explained because the resultant equation system is indeterminate for concrete angles. It is indeterminate because Euler angles are not unique, i.e., when θ is equal to ±90º.
- The basic idea of quaternions is that any reference system change can be expressed as a rotation around one vector (**μ**). The quaternion vector, denoted by **q**, has 4 components and is defined as:

$$\mathbf{q} = \begin{bmatrix} a \\ b \\ c \\ d \end{bmatrix} = \begin{bmatrix} \cos(\mu/2) \\ (\mu_x/\mu)\cdot\sin(\mu/2) \\ (\mu_y/\mu)\cdot\sin(\mu/2) \\ (\mu_z/\mu)\cdot\sin(\mu/2) \end{bmatrix}. \qquad \text{Eq. 14}$$

In quaternion forms, a system reference change is expressed:

$$\mathbf{r}'_{\mathrm{n}} = \mathbf{q}\cdot\ \boldsymbol{r}^{\mathrm{b}'}\cdot\mathbf{q}^{*}. \qquad \text{Eq. 15}$$

Where $\mathbf{q}^*$ is [a –b –c -d]$^{\mathrm{T}}$ and the superscript $\mathbf{r}'$ stands for the vector in quaternion form: [0 [r]]. Multiplication between quaternions must be done considering b, c and d as imaginary numbers. Then:

$$\mathbf{q} = \begin{bmatrix} a \\ b \\ c \\ d \end{bmatrix};\ \mathbf{q}' = \begin{bmatrix} a' \\ b' \\ c' \\ d' \end{bmatrix};\boldsymbol{q}\cdot\boldsymbol{q}' = \begin{bmatrix} a & -b & -c & -d \\ b & a & -d & c \\ c & d & a & -b \\ d & -c & b & a \end{bmatrix}\begin{bmatrix} a' \\ b' \\ c' \\ d' \end{bmatrix}. \qquad \text{Eq. 16}$$

Operating with Eq. 15 and Eq. 16, Eq. 17 can be obtained:

$$\mathbf{r}^{\mathrm{n}} = \mathbf{C}\mathrm{p}^{\mathrm{b}};\ \ \boldsymbol{C} = \begin{bmatrix} a^2+b^2-c^2-d^2 & 2(bc-ad) & 2(bd+ac) \\ 2(bc+ad) & a^2-b^2+c^2-d^2 & 2(cd-ab) \\ 2(bd-ac) & 2(cd-ab) & a^2-b^2-c^2+d^2 \end{bmatrix}. \quad \text{Eq. 17}$$

Quaternions evolve with time with the following equation:

$$\dot{\mathbf{q}} = \begin{bmatrix} \dot{a} \\ \dot{b} \\ \dot{c} \\ \dot{d} \end{bmatrix} = 0.5\mathbf{q} \cdot \begin{bmatrix} 0 \\ \omega_x \\ \omega_y \\ \omega_z \end{bmatrix} \quad \text{Eq. 18}$$

Observing the three mathematical approaches, it can be seen how the most practical to be implemented in an INS processing is the quaternions approach. But the quaternions do not express by itself attitude. The best way to express the attitude is Euler Angles but, as it has been said before, they are not useful for signal processing. The direct cosine matrix method has some disadvantages in signal processing that are going to be explained in section 4.6 . Therefore, navigation algorithms use quaternions.

As a result, conversion of quaternions to Euler angles and vice versa should be added at the end of processing. In some cases this conversion is needed because other subsystems use Euler angles. However, navigation algorithm does not use Euler angles even when the required output is Euler angles.

$$\mathrm{a} = \cos\left(\frac{\Phi}{2}\right)\cos\left(\frac{\theta}{2}\right)\cos\left(\frac{\psi}{2}\right) + \sin\left(\frac{\Phi}{2}\right)\sin\left(\frac{\theta}{2}\right)\sin\left(\frac{\psi}{2}\right), \quad \text{Eq. 19}$$

$$\mathrm{b} = \sin\left(\frac{\Phi}{2}\right)\cos\left(\frac{\theta}{2}\right)\cos\left(\frac{\psi}{2}\right) - \cos\left(\frac{\Phi}{2}\right)\sin\left(\frac{\theta}{2}\right)\sin\left(\frac{\psi}{2}\right), \quad \text{Eq. 20}$$

$$\mathrm{c} = \cos\left(\frac{\Phi}{2}\right)\sin\left(\frac{\theta}{2}\right)\cos\left(\frac{\psi}{2}\right) + \sin\left(\frac{\Phi}{2}\right)\cos\left(\frac{\theta}{2}\right)\sin\left(\frac{\psi}{2}\right), \quad \text{Eq. 21}$$

$$\mathrm{d} = \cos\left(\frac{\Phi}{2}\right)\cos\left(\frac{\theta}{2}\right)\sin\left(\frac{\psi}{2}\right) + \sin\left(\frac{\Phi}{2}\right)\sin\left(\frac{\theta}{2}\right)\cos\left(\frac{\psi}{2}\right), \quad \text{Eq. 22}$$

$$\Phi = \arctan\left[\frac{2(cd-ab)}{a^2-b^2-c^2+d^2}\right], \quad \text{Eq. 23}$$

$$\theta = \arctan[2(bd-ac)] \text{ and} \quad \text{Eq. 24}$$

$$\psi = \arctan\left[\frac{2(bc+ad)}{a^2+b^2-c^2-d^2}\right]. \quad \text{Eq. 25}$$

When θ approaches to π/2, the other two angles have indeterminate solutions. This is why near that angle the equations of Φ and ψ are approximated to:

$$\psi - \Phi = \arctan\left[\frac{2(cd-ab)-2(bc-ad)}{2(bd+ac)+a^2-b^2+c^2-d^2}\right] \text{ and} \quad \text{Eq. 26}$$

$$\psi + \Phi = \arctan\left[\frac{2(cd-ab)+2(bc-ad)}{2(bd+ac)+a^2-b^2+c^2-d^2}\right]. \quad \text{Eq. 27}$$

These equations are used when θ approaches π/2 and when θ=π/2 the values of ψ and Φ are fixed alternatively. First ψ is fixed and Φ is calculated and in next iteration ψ is calculated and Φ is fixed. This process is done while θ=π/2. The indeterminacy has been solved thanks to the use of quaternions in the navigation algorithm.

4.2.2.2 Other strapdown considerations

The calibration of strapdown systems is more difficult than in gimballed or floated systems. If the INS is very stable, it would be possible to calibrate it only once, but for most INS such option means an error increase which is not acceptable. Therefore, it will be necessary to calibrate them over time, by other techniques (GNSS). Aldebaran launcher's INS is used only one time (it burns in the re-entry). Therefore it is only calibrated one time during the five days pre-launch period.

Depending on the output signal reference frame, some computations, which are not shown in Figure 28, should be done before integration. For example, in case of Earth-fixed reference frame, the rotation of the Earth has to be taken into account before integrating. Another example is the local level reference frame. In this case, the axis rotation due to horizontal velocity has to be also computed.

Another computation complexity has to be added: rotation operations are not commutative. This means that the integration process has to be more complex than in gimballed case.

As it can be seen in Figure 28 and Figure 26, signal processing for strapdown and gimballed systems is quite different. The main difference is the gyroscope outputs. While in strapdown systems the gyroscope output is the turn rate, which must be integrated to obtain attitude, in gimballed systems the gyroscope output is the attitude. In addition, in strpdown systems the measurement axis changes in the inertial reference frame.

In this project, the model is needed to be as general as possible. But an important simplification can be done observing the mission profile shown in section 5.1 and the top level requirements shown in section 3. Gimballed systems penalise more than strapdown systems in weight, power consumption and volume, as it can be seen in Annex A. Therefore, the model is going to be focused in strapdown systems.

4.3 ERROR

Error can come from different sources. The configuration of the INS, the number of sensors and the sensor type can cancel or reduce some errors. The main error types are described in this section.

The vertical direction calculations are unstable due to the fact that gravity decreases with increasing altitude. This error source is going to be analysed in section 6.3 because it is not caused by the sensor itself.

4.3.1 Effect of system heading error

The INS is based on integrating the sensor outputs in order to determine the velocity, the position and the attitude. In order to do that, it is necessary to know in which direction the sensors are measuring. In a simplified 2D analysis, such as the one shown in Figure 29, it can be seen how important it is to know the measurement axis:

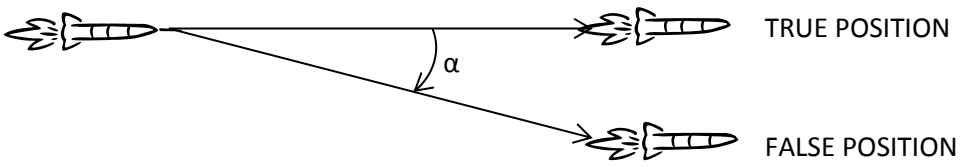

Figure 29: Effect on system heading error.

The cross-track distance error e_c depends on the initial attitude error (α), initial velocity (v) and acceleration (a), which is considered constant.

$$e_c = \sin(\alpha) \cdot \left(v \cdot t + \frac{1}{2} a \cdot t^2\right) \approx \alpha \cdot (v \cdot t + \frac{1}{2} a \cdot t^2) \,. \qquad \text{Eq. 28}$$

As it can be seen in Eq. 28, error increases lineally with the velocity and acceleration initials values, but increases quadratically with time.

4.3.2 Scale factor

As the output signal needs after-treatment by a digital computer, it will be necessary to digitalize the signal if it is analogic. To convert the output into an acceleration value it is necessary to know the conversion factor. The scale factor is the ratio between a change in the output signal and a change of the input.

The scale factor, K, can be found with:

$$K = \frac{\text{Output signal}}{\text{True input}} \,. \qquad \text{Eq. 29}$$

Most sensors have only one scale factor, but some sensors have a positive scale factor and a negative one. This fact is known as factor asymmetry. In this case the signal correction algorithm must detect which scale factor is needed.

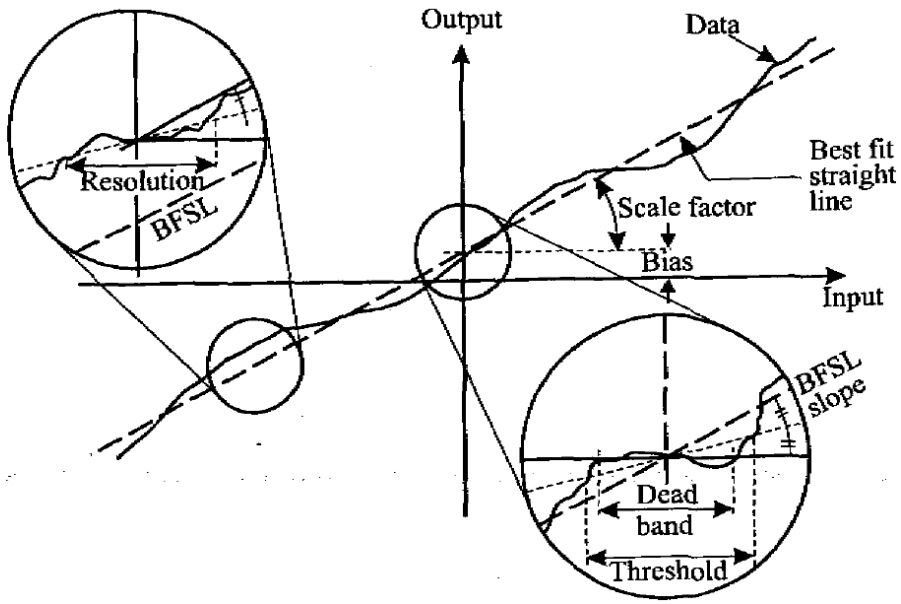

Figure 30: Sensor output errors [A-2].

Figure 30 shows the main error sources. There, can be also seen how the scale factor does not perfectly reproduce the sensor performance. In order to reduce the error associated to that fact, the output can be modelled as a second or third order function of the input. This error can be reduced but not eliminated because there are some parameters that affect the scale factor, for example, temperature, vibration, chock and input axis direction changes. Therefore, huge number of tests should be done to perfectly determine the scale factor in all cases.

4.3.3 Nonlinearity and composite error

Sometimes, the scale factor is not constant. In these cases, the error should be plotted. If the error is randomly distributed there is no possible improvement but the standard error can be calculated. On the other hand, when it is not random, the approximation curve order can be increased.

The composite error, ratio between the largest error and the full-scale range, can also be calculated. It includes many error types, such as hysteresis and resolution.

In the case of gyros, the scale factor is very important because as it has been seen in 8.3.2, heading error can evolve into huge position errors.

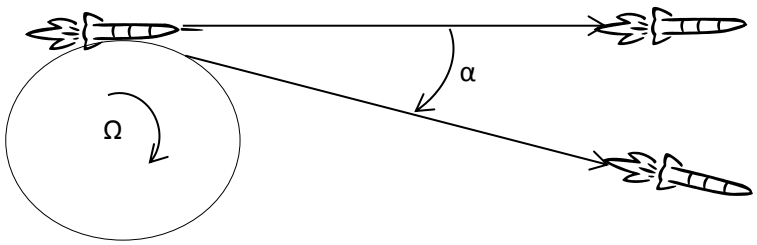

Figure 31: Effect of gyro scale factor error in position.

In Figure 31, the position error that produces the gyro scale factor error is represented. Using Eq. 28 and assuming constant angular and linear velocities, Eq. 30 can be found:

$$e_c \approx \Omega \cdot t_1 \cdot \frac{\Delta K}{K} \cdot v \cdot t_2 \,, \qquad \text{Eq. 30}$$

where t_1 and t_2 are the time spent in circular and linear trajectories respectively.

Asymmetry scale factor is not a problem for most INS because a two scale factor system can be implemented. But the systems that compensate the bias have two scale factors relatively different and usually oscillate around null conditions. Sometimes this asymmetry can mistakenly be interpreted as a bias.

4.3.4 Bias

Generally, even when there is no input, the output is not null. This effect is caused by the bias error. The bias can be easily compensated by subtracting the calibrated value to the measured output. But the problem can be the non-repeatability of the bias from turn-on to turn-on. Moreover, the bias might increase with time.

If the estimated sensor attitude is different from the real attitude, the difference in the gravity component can be mistakenly interpreted as a bias error during calibration. If a gyroscope has a slightly bias uncompensated error, the misalignment of the accelerator axis would increase over time. This has catastrophic consequences, as the position error increases with t^3.

4.3.5 Random Drift

Previously, in section 4.3.3 , randomly distributed error has been described. This error is called random drift and can be characterized by standard deviation. This noise sometimes can be associated to some mechanical sensor designs. In these cases, the noise has peaks at some frequencies. For example, in mechanical gyros with ball bearings it can be observed how these peaks change

in function of the ball size, the number of balls or the operating speed. In mechanical gyros with ball bearings there are always low frequency noises produced for the very small differences between the bearings of both ends.

This drift is also called in-run drift in order to differentiate it from turn-on uncertainties.

4.3.6 Dead Band, threshold and resolution

The dead band is the near zero input range where no output is detected. This fact is caused because some mechanical sensors need a minimum critical load to start functioning. Furthermore, sometimes an output is generated but it is smaller than the noise and consequently, cannot be distinguished.

The threshold is the minimum input that produces an output of at least half the expected value.

The minimum measurable input is the resolution. In analogic output sensors the resolution of the Analogical to Digital (A-D) converter should be taken into account. This resolution can be quite different from the sensor resolution.

4.3.7 Hysteresis

Hysteresis is the maximum difference, for a specific input, between the sensor output being reached by the input value increasing and by it decreasing. It is difficult to cancel this effect because high frequency phenomena can occur between input acquisitions and the effect of trying to cancel hysteresis could be an error increase.

4.3.8 Day-to-Day uncertainty

The aging of internal elements, produced by many external sources (environmental storage conditions, vibrations or shocks, magnetic fields, etc.) can modify the scale factor and bias. The bias change can be 10 times bigger than in-run random drifts.

4.3.9 Gyros acceleration sensitivities

The error source, in this case, is the gyro output that is not consequence of turn rate but is consequence of acceleration. This fact is produced by mass unbalance. The origins of mass unbalance are materials imperfections, fabrication tolerances, assembly tolerances and mechanical component tolerances. Mass unbalance is not the single cause of gyros acceleration sensitivities, anisoelasticity also produces this phenomena. In case of a mass supported by two brackets with different rigidities in the x and y directions, if acceleration at 45º is produced, the mass would rotate along the z axis. Other

phenomena produce gyro acceleration sensitivities. But all these effects can be calibrated and compensated. Consequently with any calibration, the compensation procedure adds more uncertainties to the final value.

4.3.10 Anisoinertia errors

Anisoinertia is the difference between moments of inertia that should be equal. The causes of this type of error are the inequalities between gyroscopes moments of inertia produced by mass unbalance. The effect is an output signal coupled between axes. In consequence, the output signal in one axe will depend on the input signal of the two perpendicular axes.

4.3.11 Rotation-Induced Errors

Accelerometer rotation sensitivities depend on the sensor type. As an example, force feedback accelerometers have sensitivity to rotation rate changes. The only way to reduce it is placing the sensor nearer to the hinge. But then the accelerometer sensitivity is reduced. As in the case of gyro acceleration sensitivities, this effect can be calibrated and compensated, but the associated uncertainties would also be added.

4.3.12 Cross-coupling errors

Cross-coupling errors are the errors produced by the momentum wheel deviation from the orthogonal configuration. As there are some difficulties in this error modelling, the error is given as a percentage of the measure, being this percentage the maximum percentage obtained in all the measurement range for the sensor manufacturer.

4.3.13 Statistics of Instrument Performance

As it has been said in previous sections, sensors present performance differences from turn-on to turn-on and during operation. Most important differences are from turn-on to turn-on.

The ideal day-to-day repeatability parameter should be estimated taking a big sample quantity and calculating the mean value and the standard deviation during many days. The data is usually assumed normally distributed. Therefore, the chances of being within a specified range at any day turn-on can be calculated.

In real sensor operation, these tests are not done due to the high need of samples. Instead, a small number of test are done and, if they fulfil a list of statistic requirements, it is considered that the sensor is within the specifications. These tests are also done to predict the mean time between failures (MTBF).

4.4 Sensor models

In this section some models used in accelerometers and gyroscopes are presented. These models cannot be applied without consulting the sensor specifications. The models shown in this section present the usual behaviour of the sensor. Nonetheless, sensor designers can compensate some sensor dependences shown in this section.

4.4.1 Gyroscope models

Gyroscopes with rotating parts and sinusoidal spinning can be modelled using Eq. 31:

$$\mathrm{I_o}\left(\frac{d^2\theta}{dt^2}\right) + c\left(\frac{d\theta}{dt}\right) + K\cdot\theta = H\cdot\Omega\ , \qquad \text{Eq. 31}$$

where:

- $\mathrm{I_0}$ is the gimbal moment of inertia about the output axis.
- c is the damping constant around the output axis
- K is the spring elastic constant
- θ is the gimbal angle
- H is the momentum wheel angular momentum
- Ω is the input rate

Then, the damping ratio and the natural frequency can be found.

$$\xi = \frac{c}{2(I_o K)^{1/2}} \text{ and} \qquad \text{Eq. 32}$$

$$\omega_\mathrm{n} = \left(\frac{K}{I_o}\right)^{1/2}. \qquad \text{Eq. 33}$$

Therefore, the transfer function has to be taken into account in the post-treatment of the output data or in the sensor selection.

If the spinning is not sinusoidal, K is null and then the output/input relation is:

$$\frac{\theta_0}{\theta_i} = \frac{H}{c}\left(1 - e^{-\frac{c}{I_o}t}\right) \qquad \text{Eq. 34}$$

In the stationary case, this equation can be expressed as follows:

$$\theta_0 = \frac{H}{c}\theta_i \qquad \text{Eq. 35}$$

According to gimbal performance, the friction should be introduced in the equation. However, these effects can usually be neglected by a proper gimbal

selection and an optimized momentum wheel. In some cases there is inertial compensation. This means that the friction is estimated in function of the gimbal movement and a motor applies the torque needed to counteract it. The static friction cannot be counteracted. Therefore, in these sensors the dead band is defined by the static friction.

Momentum wheels working with hysteresis motors have a mounting that can be modelled as an elastic coupling. The natural frequency of this elastic coupling (4-40 Hz) is usually similar to the spinning frequency. Therefore, the anisoinertia torques, which have the spinning frequency, are maximized. The anisoinertia torques are defined in Eq. 36.

$$\mathrm{T_{ani}} = \frac{1}{2}\Big(\big(I_{gs} + C\big) - \big(I_{gi} + A\big)\Big)\,\Omega^2 \sin 2\alpha, \qquad \text{Eq. 36}$$

where:

- I_{gs} is the gimbal inertia about the spinning axis (sensor axis)
- I_{gi} is the gimbal inertia about the input axis
- C is the rotor polar inertia
- A is the rotor transverse inertia
- Ω is the spinning rate about an axis contained in the input-sensor axes plane
- A is the angle between the spinning axis and the sensor axis

The effect of the frequency similarity can be modelled as a torque increase.

$$\Delta\mathrm{T_{max}} = \frac{1}{2}\mathrm{C}\,\Omega^2\ . \qquad \text{Eq. 37}$$

The torque increase depends on the elastic coupling and the frequency difference. Nonetheless, the maximum torque increase can be computed with Eq. 37 [A-2].

Errors due to anisoinertia can be sharply reduced by adjusting the wheel rotor. The adjusting can be done by displacing the mass centre or by making the electrostatic field nonuniform.

Previous models have to be taken into account in order to refine the output signal model. The IEEE proposed model for single axis gyros output signal is sown in Eq. 38 [A-2]:

$$\frac{\mathrm{S}}{\mathrm{K}} = \Omega_{\mathrm{i}} + B + (D_i a_i + D_0 a_0 + D_s a_s) + \big(D_{ii} a_i^2 + D_{ss} a_s^2 + D_{is} a_i a_s + D_{io} a_i a_0 + D_{os} a_0 a_s\big)\ , \qquad \text{Eq. 38}$$

where the subscript ‘i' stands for relative to the input axis, the subscript ‘s’ for relative to the rotating axis and the subscript ‘o’ for relative to the output axis. In

Eq. 38, Ω stands for spinning rate, B for bias, S for the signal output and K for the scale factor. In the first parenthesis, the input and sensor axes mass unbalance and the output axis g-sensitivity are included. In the second parenthesis, the acceleration sensitivity second order values are included. It must be remarked that in Eq. 38 the acceleration values are the sum of the acceleration sensed by the accelerometers and the gravity acceleration.

However, the motion-added error rate also needs to be considered, and should be corrected in the data post-treatment or should be assumed as a signal error. The motion-added error rate can be computed with Eq. 39:

$$\frac{\mathrm{dS}}{\mathrm{K}} = (\mathrm{I_s} - \mathrm{I_i})\frac{\Omega_i \Omega_s}{\mathrm{H}} + \theta_o \Omega_s + D_o \Omega_0 + \frac{I_o \alpha_0}{H} \ . \qquad \text{Eq. 39}$$

The notation used in Eq. 39 is the same used in previous equations in this section. Anisoinertia error and cross coupling error are the origin of the first and second equation terms. Rate error from angular rate about the output axis and angular acceleration about output axis are the origin of the two other equation terms.

For a dynamically tuned gyroscope, Anthony Lawrence in reference A-2 proposed the model sown in Eq. 40. As this type of gyroscope measures in two axis, in Eq. 40 the measuring axis are x and y and the spinning axis is z.

$$\begin{aligned}\frac{\mathrm{S_x}}{\mathrm{K_x}} = \Omega_\mathrm{x} + B_x + D_{xx}a_x + D_{xy}a_y + D_{xz}a_z + D_{x0x}\emptyset_x + D_{x0y}\emptyset_y + \\ D_{xy1}a_{1Nz} + D_{xy2}a_{2Nxy} + D_{xy3}\left(\frac{d\emptyset}{dt}\right)_{2Nxy} + D_{xxz}a_z a_x + \\ D_{xi}\left(\frac{d\emptyset}{dt}\right)_x \left(\frac{d\emptyset}{dt}\right)_z (w)\ ,\end{aligned} \qquad \text{Eq. 40}$$

where:

- The D terms are the calibration constants.
- ∅ is the angle turned in the axis x or y by the momentum wheel
- a_{1Nz} is the vibration at momentum wheel spinning frequency acceleration amplitude due to imperfections in the momentum wheel
- a_{2Nz} is the vibration acceleration amplitude in the input axis due to misalignments between the rotor and stator in the motor.
- $\left(\frac{d\emptyset}{dt}\right)_{2Nxy}$ comes from the gimbal axis misalignment
- The last equation term is frequency sensitive. It also depends on the turning rate around x and z axis.

4.4.2 Accelerometer models

The Institute of Electrical and Electronics Engineers (IEEE) has proposed some standards in order to make the sensor selection easier for the INS designer.

IEEE has proposed for all pendulous accelerometers the following standard model [A-2]:

$$a = \frac{E}{K_1} \approx B_o + a_i + K_2 a_i^2 + K_3 a_i^3 + d_o a_p + K_{ip} a_i a_p - d_p a_0 + K_{io} a_i a_0 \ , \qquad \text{Eq. 41}$$

where:

- E is the instrument output, in V or in Hz.
- K_1 is the scale factor, in output units/g. Sensors with scale factor asymmetry have K_1 defined as $K_1^+\xi^+ + K_1^-\xi^-$, where $\xi^{+/-}$ is a binary variable that is one or zero in function of the input value (positive or negative). Gyroscope models shown in Eq. 38 and Eq. 40 are lineal. The model shown in Eq. 41 is not lineal.
- B_0 is the bias value in g or m/s^2.
- a_i is the acceleration in the axis that is measured. All the parameters which have the subscript 'i' are relative to the input axis.
- K_2 and K_3 are the nonlinearities parameters. Their units are g/g^2 and g/g^3 respectively. Taking into account the available sensor data, IEEE has considered that higher order terms do not reduce sensor error.
- d_0 is the misalignment factor around the hinge axis. Therefore, it is multiplied by the acceleration in the axis perpendicular to the hinge and input axes. The factors relative to this axis have the subscript 'p'. The subscript '0' means relative to the hinge axis. d_p is the misalignment factor around the 'p' axis. Therefore, in Eq. 41 this factor is multiplied by the acceleration in the hinge axis.
- K_{ip} and K_{i0} are the crossing factors. Ideally they should be zero. However, most sensors need some corrections due to manufacturing tolerances and material imperfections.

A pendulous accelerometer also measures the turning rate change around the hinge axis and the turning rate around the other two axes.

$$\frac{\text{Acceleration}'}{\text{constant}} = I_0\alpha_0 + (I_p - I_i)\Omega_i\Omega_p \ . \qquad \text{Eq. 42}$$

α and Ω are the turning rate change and the turning rate respectively. The 'I' factors are the moments of inertia, which are determined by the gyroscope. It must be taken into account that they are not constant, but depend on the hinge deflection. The acceleration measured due to α and Ω is proportional to the moment of inertia. That acceleration is named Acceleration' in Eq. 42[A-2].

Vibratory accelerometers are modelled by Kearfott with Eq. 43, Eq. 44 and Eq. 45 [A-2].

$$f_1 = K_{01} + K_{11}a + K_{21}a^2 + K_{31}a^3 \ , \qquad \text{Eq. 43}$$

$$f_2 = K_{02} - K_{12}a + K_{22}a^2 - K_{32}a^3 \ \text{ and} \qquad \text{Eq. 44}$$

$$f_1 - f_2 = (K_{01} - K_{02}) + (K_{11} - K_{12})a + (K_{21} - K_{22})a^2 + (K_{31} - K_{32})a^3 \ . \qquad \text{Eq. 45}$$

Eq. 45 is the combination of the previous two equations. Ideally the first and third parentheses are null. However, in real sensors these factors are usually not negligible [A-2].

In vibrating accelerometers, constants are usually computed with a third order approximation on temperature:

$$K_i = K_{i_0} + K_{i_1}T + K_{i_2}T^2 + K_{i_3}T^3 \qquad \text{Eq. 46}$$

4.5 Calibration and error compensation

Testing and calibration are important to determine sensor specs. It is important to perform testing and calibration in the same environment than in operation. If a generic testing and calibration is done, the measured errors are greater than in the specific testing and calibration.

Each specification has some error margin. The error margin can be reduced by improving the sensor calibration. In the sensor selection phase it is important to determine the testing and calibration methods to be used because testing and calibration costs can be a significant INS costs percentage.

If an external factor is not calibrated, the maximum output change due to that factor must be computed as error in all conditions. But, the calibration and correction also add some errors to be computed in the sensor. For example, if the temperature is not calibrated, the maximum output change within the operation range must be added in the output error. However, if temperature correction is done, the calibration errors (calibration temperature errors, input errors and output measurement errors) must be added to the sensor output error. This is the reason why many ISA are temperature controlled, they are always working within a very short temperature range, reducing by this way the output temperature associated error.

The first tests batch consists on one test for each input considered in the sensor model. Some examples of sensor models are described in Annex A. The tests input must cover the expected operational range and they must be done at constant temperature. It must be reminded that each model constant value has an associated error value.

Then, the signal temperature dependence is determined. Each sensor model constant must be modelled in function of temperature. Obviously, this calibration also adds some uncertainties to the sensor model. Temperature change rate also affects the sensor output signal [A-1]. However, the temperature rate change does not worth compensation [15]. Therefore, the best way to take this effect into account in the ISA model is to consider it a sensor intrinsic error, taking the worst case value.

Electromagnetic tests are also performed. The ISA is subjected to the worst electromagnetic environment the ISA will undergo in its operational environment. Correcting the sensor output from electromagnetic environment is not feasible in a launcher context, as more sensors should be equipped. Instead of equipping more sensors, ISA electromagnetic isolation is preferred for reasons of weight, simplicity and reliability. Then, the maximum signal deviation produced by the electromagnetic field should be included in the intrinsic signal error.

Most sensors have vibratory dependant model constants. Therefore, the constant modelling described previously must be done in the vibratory environment that the sensor will undergo in its operational life. Vibratory corrections are not suitable in a launcher context because that would imply adding extra sensors. These sensors would be accelerometers. Consequently, each ISA should have another ISA with accelerometers suitable for measuring the vibratory environment. The vibratory compensation does not produce a significant signal error reduction to compensate all the drawbacks that produces.

Therefore, the sensor output signal changes due to changes in vibratory environment should be included in the intrinsic signal error. This modelling should take into account the vibratory environment during the whole mission. However, the ISA is isolated from high frequency vibrations with an elastic assembly. Thus, the ISA's vibratory environment is less detrimental than the host vehicle vibratory environment.

Shocks must also be taken into account during calibration. Shocks produce a sensor output reaction similar to the signal output shown in Figure 32.

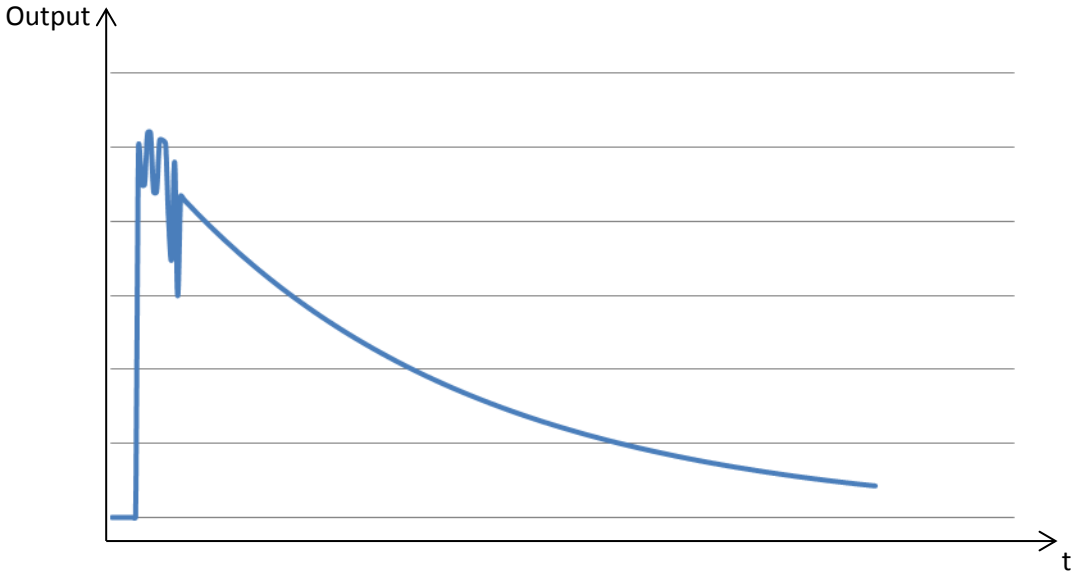

Figure 32: Sensor output reaction to a shock. The shock is applied in the first output increase.

Applying the same reasoning than in the vibratory environment case, the shock effects should be included in the signal intrinsic error. Ageing and storage tests are also done. However, in Aldebaran context the INS is used just once. Then, ageing and storage are not relevant variables because the tests are done at maximum five days before the launch. As most sensors are recommended to be revised at intervals of one or two years [A-1], in this project ageing and storage factors are not going to be taken into account.

Taking into account the corrections and calibrations presented in this section, the gyros output is modelled as shown in Eq. 47 :

$$\frac{\mathrm{Output_x}}{K_1} = (1+S_x)\omega_x + (M_y+\Delta M_y)\omega_y + (M_z+\Delta M_z)\omega_z + (B_{fx}+\Delta B_{fx}) + (B_x+\Delta B_x)a_x + (B_y+\Delta B_y)a_y + (B_z+\Delta B_z)a_z + (B_{xx} + \Delta B_{xx})a_x^2 + (B_{zz}+\Delta B_{zz})a_z^2 + (B_{yy}+\Delta B_{yy})a_y^2 + (B_{xz}+\Delta B_{xz})a_x a_z + (B_{xy}+\Delta B_{xy})a_x a_y + (B_{yz}+\Delta B_{yz})a_y a_z + n_x \,. \quad \text{Eq. 47}$$

The origin and definition of each term can be found in Annex A and section 4.4 . In mechanical gyros, the z axis is the spin axis, but in other sensor types the axis should be defined by the supplier. In Eq. 47 the term that depends on $a_x \cdot a_y$ has been added in order to take into account misalignments between the theoretical and actual orientation about the measurement axis. As it has been said previously in this section, n_x includes sensor random response, electromagnetic interferences, vibratory and shock environment response and not modelled temperature effects. This calibration model is not suitable for dual axis sensors. The model has not been adapted to them because dual axis sensors are not

suitable in the Aldebaran context. They are not suitable because the ISA should measure the turn rate about three orthogonal axes due to the type of redundancy used. In this report, redundancy is going to be evaluated in section 6.2 .

Eq. 47 can be particularized for each gyroscope type. For example, all the acceleration terms are null in optical gyroscopes. Gyroscopes based on the difference between two signals that are affected in opposite ways have the B_{fx} term null.

B_{fx} term does not depend of any input. However, it can depend on time. Each sensor model has its own model. The simplest model is the constant model. Some models use linear time dependence and some others use an asymptotical dependence [A-1].

Accelerometers use the model shown in Eq. 48 to calibrate the sensor:

$$a_x = (1 + S_x)a_x + M_y a_y + M_z a_z + B_f + B_{xy} a_x a_y + B_{xz} a_x a_z + n_x \ , \qquad \text{Eq. 48}$$

where S_x is a polynomial value that depends on a_x. Some accelerometers need better calibrations and need up to a third order calibration in a_x. Furthermore, the corrections detailed in Eq. 42 can be added. In this project, they are going to be added because the model is needed to be as general as possible. However, adding this term to the calibration is a trade-off between a better instrument modelling and its associated costs. The model is better expressed in Eq. 49, where Eq. 42 terms have been included:

$$\begin{aligned} Output_x = {} & (K_1 + S_1)a_x + (K_2 + S_2)a_x^2 + (K_3 + S_3)a_x^3 + (M_y + \Delta M_y)a_y + \\ & (M_z + \Delta M_z)a_z + (B_f + \Delta B_f) + (B_{xy} + \Delta B_{xy})a_x a_y + (B_{xz} + \Delta B_{xz})a_x a_z + \\ & (PI_y + \Delta_1)\alpha_y + (P(I_z - I_x) + \Delta_2)\omega_x \omega_z + (P(I_y - I_x) + \Delta_3)\omega_x \omega_y + \\ & (B_x + \Delta B_x)\omega_x + (B_y + \Delta B_y)\omega_y + (B_z + \Delta B_z)\omega_z + n_x \ , \end{aligned} \qquad \text{Eq. 49}$$

where P is the constant value in Eq. 42 and y is the hinge axis. The error values of the polynomial adjust should be very small compared to the adjust values. However, they have been included in the model because calibration is an expensive process and sometimes it is preferred to leave some error in these terms and reduce the calibration costs. All the terms related to axis misalignments have been also included.

Furthermore, accelerometer and gyroscope output models should be frequency response analysed. Some accelerometers increase the response at some input

frequencies. Some examples are the gyroscopes and accelerometers described in Annex A that have natural oscillation frequency.

4.6 Attitude and acceleration computation

As it can be seen in Eq. 47 and in Eq. 49, the computation of the acceleration and attitude vectors in body frame cannot be done independently. The equation system to solve is a non-lineal six variable system. When studying a specific sensor combination, this problem can be avoided by simplifying the sensor model. However, no simplifications will be applied in this project, as it is intended to develop an INS model that could be used in any sensor combination. Analysis of computational costs is not included in this project because the analysis should be done of the whole Navigation system and not only of the INS part.

If optical gyroscopes are used, the equation system can be divided into two systems and the gyroscope part can be solved independently. The gyroscope equations can be solved iteratively. Although they are not sensitive to acceleration they are coupled.

In this project the equation system is going to be solved iteratively starting with the last solution vector as a guess values set. The first step will be to solve the accelerometer equations with the Newton-Raphson method. Newton-Raphson method is used because in the sensor range the function will always be increasing. Therefore, the convergence with Newton-Raphson will be fast. After the acceleration calculation, the gyroscope equations are going to be solved with the updated acceleration values. The solving process can be divided in the following points:

1. Sensor outputs acquisition
2. Solve acceleration and gyroscope equations with previous values
3. Evaluate attitude equations with updated acceleration values.
4. Evaluate acceleration equations with updated attitude values.
5. If the difference between updated and previous values is greater than the maximum iterative process error value in any variable, return to step 2 with updated values. Otherwise, the updated values are the sensor corrected values.

In this project, the iterative process error value (the precision used for solving iterative equations in the navigation and sensor corrections algorithms) is not going to be considered as a model variable. The main reason is that in this project computational time is not going to be evaluated. The other reason is that with most sensors, the iterative process can be sharply reduced, thanks to the fact that, some gyros are independent from acceleration and most

accelerometers are independent from rotation movement. Consequently, the iterative process error is set at a value that can be neglected.

Reached this point, it must be considered that the measurement axis of the gyroscopes changes with the host vehicle attitude. If the data processing is done with the direct cosine matrix, the algorithm order should be higher when it is done with quaternions. This fact can be seen in Table 2, where the attitude drift error is smaller in quaternion algorithms for all algorithm orders.

Algorithm order	Attitude drift error (º/h)	
	Direct cosine matrix	Quaternions
1	6870	1720
2	3430	860
3	7	0.4
4	1.7	0.2

Table 2: Attitude drift error due to algorithm order for a single axis rotation. In both cases the maximum input error is set to 0.1 rad [A-2].

Quaternion approach has the drawback that the direct cosine matrix should be found in order to transform the acceleration vector to inertial frame reference. However, the quaternion approach has been found more suitable for this modelling. The following points define some variables that are relevant during computation:

- $\vec{\theta}$ is the angle vector with direction and magnitude such that the rotation of the body frame between two samples can be expressed as a rotation of the vector magnitude around the vector direction.
- ω is the vector which components are the corrected gyroscope outputs.
- r_k is the quaternion representing form of a rotation of magnitude θ about the axis $\vec{\theta}$

If the rotation of the measurement axis is not taken into account, the equation that defines $\vec{\theta}$ would be:

$$\vec{\theta} = \int_t^{t+\Delta t} \omega \, dt \quad . \qquad \text{Eq. 50}$$

However, the axis rotation should be considered. Bortz, J.E. proposed in reference 16 an equation which includes this fact:

$$\vec{\theta} = \int_t^{t+\Delta t} \left(\omega + \frac{1}{2}\vec{\theta}\,\mathrm{x}\,\omega + \frac{1}{\theta^2}\left[1 - \frac{\theta sin\theta}{2(1-cos\theta)}\right]\vec{\theta}\mathrm{x}\,\vec{\theta}\,\mathrm{x}\,\omega\right) dt\ . \qquad \text{Eq. 51}$$

This equation is not suitable for computation. Eq. 51 needs to be iterated. Furthermore, the cosine and sine terms should be developed in series expansions. Due to the computing complexity, Savage, P proposed in reference 17 to simplify considerably the equation but to integrate with more frequency the attitude than the acceleration. In this model case, increasing the attitude frequency would be useless because the error correction is high coupled. Moreover, Aldebaran trajectory has large acceleration changes in short time intervals that do not allow reducing acceleration integration frequency. Therefore, is not going to be implemented in the model. The equations that Savage proposed were:

$$\vec{\boldsymbol{\theta}} = \boldsymbol{\beta} + \delta\boldsymbol{\beta}\ , \qquad \text{Eq. 52}$$

$$\boldsymbol{\beta} = \int_{\mathrm{t}}^{\mathrm{t}+\Delta\mathrm{t}} \boldsymbol{\omega}\,\mathrm{dt} \quad \text{and} \qquad \text{Eq. 53}$$

$$\delta\boldsymbol{\beta} = \frac{1}{2}\int_t^{t+\Delta t} \boldsymbol{\beta}\,\mathrm{x}\,\boldsymbol{\omega}\,\mathrm{d}t\ . \qquad \text{Eq. 54}$$

Then, r_k can be computed:

$$\mathbf{r}_{\mathrm{k}} = \begin{bmatrix} a_c \\ a_s\theta_x \\ a_s\theta_y \\ a_s\theta_z \end{bmatrix}\ , \qquad \text{Eq. 55}$$

$$\mathrm{a_c} = \cos\left(\frac{\theta}{2}\right) \approx 1 - \frac{(0.5\theta)^2}{2!} + \frac{(0.5\theta)^4}{4!} - \frac{(0.5\theta)^6}{6!} + \cdots \quad \text{and} \qquad \text{Eq. 56}$$

$$\mathrm{a_s} = \frac{\sin\left(\frac{\theta}{2}\right)}{\theta} \approx 0.5\left(1 - \frac{(0.5\theta)^2}{3!} + \frac{(0.5\theta)^4}{5!} - \frac{(0.5\theta)^6}{7!} + \cdots\right)\ . \qquad \text{Eq. 57}$$

Finally, the attitude quaternion can be updated:

$$\mathbf{q}_{\mathrm{k+1}} = \mathbf{q}_{\mathrm{k}} \cdot \boldsymbol{r}_k = \begin{bmatrix} q_{k_1} & -q_{k_2} & -q_{k_3} & -q_{k_4} \\ q_{k_2} & q_{k_1} & -q_{k_4} & q_{k_3} \\ q_{k_3} & q_{k_4} & q_{k_1} & -q_{k_2} \\ q_{k_4} & -q_{k_3} & q_{k_2} & q_{k_1} \end{bmatrix} \begin{bmatrix} a_c \\ a_s\theta_x \\ a_s\theta_y \\ a_s\theta_z \end{bmatrix} = \begin{bmatrix} q_{k+1_1} \\ q_{k+1_2} \\ q_{k+1_3} \\ q_{k+1_4} \end{bmatrix}. \qquad \text{Eq. 58}$$

The errors related to this procedure can be computed. However, in this report, they are going to be analysed in the sensitivity part of the model. By doing this, the overall affectation is going to be reflected and not only a part of it.

Acceleration also needs to be computed taking into account that the sensor axis change. In this case, no approximations should be done apart from considering constant the acceleration during the integration interval. It must be taken into account that the gravity must be added to the acceleration vector. The 'false velocity vector' (v) can be found by integrating acceleration over time in body axis without taking into account the attitude change during the integration interval.

$$\mathbf{v} = \int_{t}^{t+\Delta t} \boldsymbol{f}^{b}\ dt\ . \qquad \text{Eq. 59}$$

Then, it can be found that:

$$\mathbf{u}_{\mathrm{n}} = \mathbf{q} \cdot \left(\mathbf{v}_{\mathrm{mean}} + \frac{1}{2}\boldsymbol{\beta}_{\mathrm{mean}} \mathrm{x}\, \mathbf{v}_{\mathrm{mean}} + \frac{1}{2}\int_{\mathrm{t}}^{\mathrm{t}+\Delta\mathrm{t}} \left(\boldsymbol{\beta}\ \mathrm{x}\ \mathbf{f}^{\mathrm{b}} - \boldsymbol{\omega}^{\mathrm{b}}\ \mathrm{x}\ \mathbf{v}\right)\mathrm{dt} \right) \cdot \mathbf{q}^{*}\ . \qquad \text{Eq. 60}$$

The subscript 'mean' stands for average properties during the integration interval.

4.7 Error modelling

The error is introduced in the model in different ways. The first part is the signal disturbance due to the ISA-host vehicle connections. In Figure 33, it can be seen how these disturbances are added to the model.

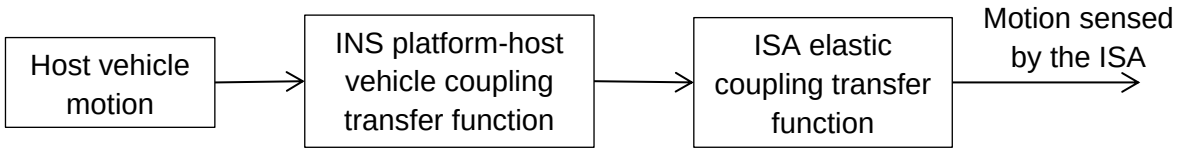

Figure 33: Scheme of the pre-ISA signal changes model.

Then, the ISA is modelled, as shown in Figure 34. The first step is the transfer function that represents the ISA input amplification or reduction in function of the frequency due to the functioning of the sensor. Afterwards, the sensor is modelled with Eq. 47 and Eq. 49. At this point, the random behaviour of the sensor contributes to the final error. In the post processing of the sensor, those equations are used but using the calibration constants, which have an uncertainty associated. Furthermore, some error is also included by sensor constants temperature corrections due to temperature measurements and temperature gradients. Thereafter, the navigation algorithm is implemented with its precisions in the iterative processes and the sub-algorithms orders.

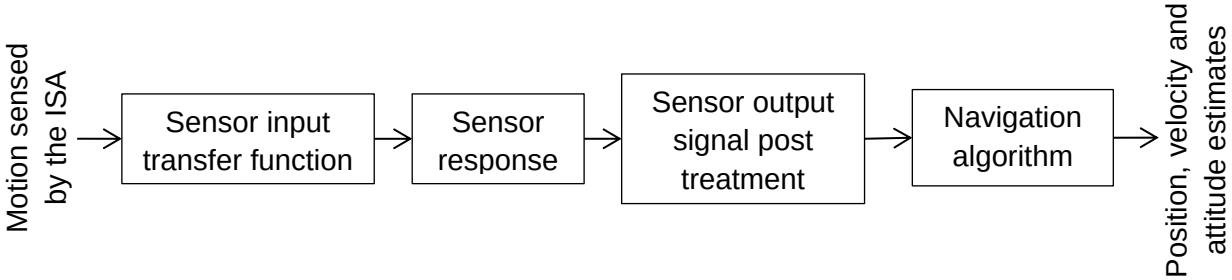

Figure 34: Scheme of the sensor and signal post treatment model.

The 'sensor signal post treatment' block also introduces some error due to the precision of the Earth gravity model used. The gravity term also includes the position estimated error. Attitude error is also reintroduced in the algorithm because it causes error in the gravity vector breakdown.

In the navigation algorithm, the initialization values error, discussed in section 6.4 , are also included. Furthermore, the position is updated with the GNSS estimated position.

The error in this project is going to be evaluated by considering the worst case in every error source. There are some methods used for associating precision to each estimated value. But these methods only consider the sensor output signal post treatment and the sensor response [A-1]. Therefore, the other error sources should be included. By including these terms the advantage of knowing the probability of having a certain precision is lost. Consequently, not using specific error models has been considered better for this INS model due to the associated complexity increase, not justified by the advantages.

4.8 Inertial navigation systems-global navigation satellite system integration

INS-GNSS integration is very interesting due to drawbacks of both systems. While GNSS errors are bounded, the INS errors increase with time. However, GNSS systems have low data rate whereas INS have high data rate of. GNSS have also the drawback of integrity and depend on an external system. Therefore, the chance of losing the signal of one satellite and not having the sufficient number of satellite signals to compute position with GNSS should be taken into account.

System integration is an expensive process. Therefore, different levels of integration exist depending on the requirements needed.

- Uncoupled systems integration is the cheapest way to integrate both systems. The GNSS estimated position is used to reset the INS position.
- Loosely coupled systems use the INS and GPS estimated positions differences as inputs in a Kalman filter. The Kalman filter is an algorithm that combines different redundant inputs in order to obtain a combined non redundant output with better accuracy than the inputs.
  The main data transfer scheme can be seen in Figure 35.

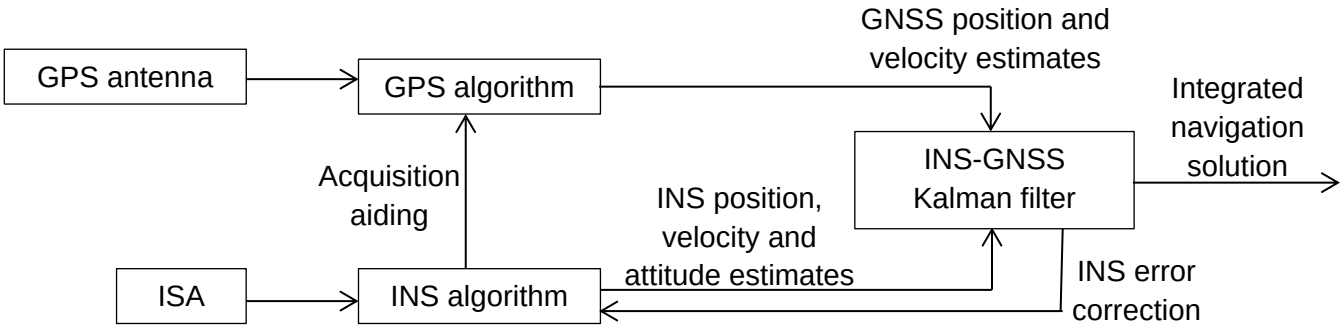

Figure 35: Scheme of the INS-GNSS coupling in a loosely coupled system.

- Tightly coupled systems reduce the GPS algorithm as it can be seen in Figure 36.

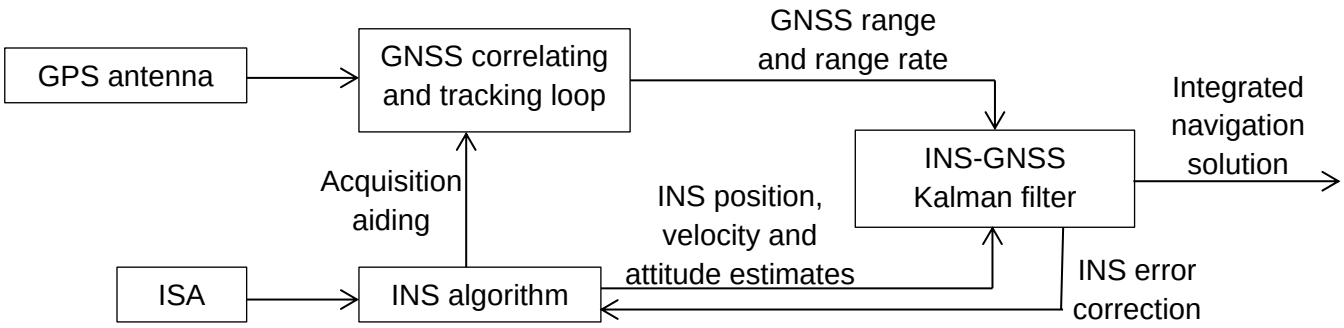

Figure 36: Scheme of the INS-GNSS coupling in a tightly coupled system.

The main advantage of this type of systems is the versatility. They can operate independently of the GNSS satellite availability. Loosely coupled systems need a minimum number of usable satellite data to use GNSS data. Furthermore, in loosely coupled systems GNSS algorithm ends with the GNSS Kalman filter. Therefore, the input of the INS-GNSS Kalman filter comes from another Kalman filter, as can be seen in Figure 36. This fact gives some complications in the INS-GNSS Kalman filter [A-2].

- Deep or ultra-tightly coupled systems are the junction of GNSS and INS algorithms in one single navigation algorithm. These Systems are able to work with the data provided by one satellite. The specifications are difficult to determine because depend on the number of satellites used, their relative position and altitude. This type of coupling offers the best performance, but is the most expensive one. The navigation algorithm is completely new and more complicated than in the other cases. Furthermore, this coupling implies higher computational requirements.

The scope of this project is not to model the INS-GNSS coupling, but to model the INS in the Aldebaran context. In the Aldebaran demonstrator, it has been found interesting to use a hybrid system. As a consequence, uncoupled system

integration is going to be implemented in the model. The reason why this integration type has been chosen is that it reflects the benefits and consequences of INS-GNSS integration but it is simple to model. As it has been said in the project scope, to model the INS-GNSS integration in order to evaluate which integration type suits better to Aldebaran mission is the scope of another GTD proposed project.

5 Model selection

The aim of this section is to justify the main decisions taken in the model design phase. The first decision concerns the simulation of the trajectory. The way the random error is simulated is also explained in this section. Furthermore, the requirement that imposes a gravity model truncated at the second zonal harmonic (J_2) is analysed.

5.1 The flight profile of Aldebaran

The trajectory that Aldebaran will follow has not yet been defined. However, some data have been published by CNES and are summarized in Table 3. They are likely to be approximations and, for this reason, they should be taken as an indication.

t [s]	Initial altitude [m]	Initial velocity [m/s]	Remarks
0	12000	208	Release manoeuvre. Flight path angle of 45º.
0-5			Free fall.
5-55	26000	1200	First stage engine operation. Constant flight path angle.
55-135	100000	4300	Second stage engine operation. Constant flight path angle.
135-145	123358		Free fall.
145-345	250000	7907,5	First ignition of the third stage.
345-3330	800000	7451,85	Elliptical orbit.
3330-3345			Spin up operation.
3345-3355			Orbit circularization.
3355-3365			Payload release.
3365-3380			Beginning of the 180º turn.
3380-3390			End of the 180º turn

Table 3: Available trajectory information. The engine cut offs are not mentioned because CNES has not published such information

At t=3390s the third stage is reignited in order to place the launcher (without the payload at this point) into an elliptical orbit with perigee into the atmosphere. This is the reason why the last manoeuvre changes the launcher's attitude, to orient the nozzle opposite to the velocity. The trajectory has been approximated until t=3380 because there is no available data about the launcher descent trajectory. Furthermore, the precision with which the position and attitude are known past t=3390s does not affect the main mission of the launcher. Consequently, the INS

model does not evaluate the navigation performance past the end of the 180º turn.

In order to approximate the trajectory some hypotheses have been made:

- The trajectory starts at y=0 (inertial reference frame) and is contained in the xy-plane. The aim of this assumption is to simplify the computation. Note that the project results are not affected by the choice of initial position or by the inclination of the trajectory.
- During the free fall phases aerodynamic drag is not relevant. This assumption is justified by the high degree of approximation of the data which allows neglecting this effect. Furthermore, the drag coefficient value (C_D) is not given and should be estimated.
- The launcher longitudinal axis is oriented like the direction of the velocity in Inertial Reference Frame. The reason for this assumption is that no information is available about the angle of attack and hence this quantity has been set to zero. The attitude of the launcher is probably not conveniently approximated, but it has been considered that turn rate values obtained with these approximations are representative enough for this project. Therefore, the turn rate can be estimated by means of the flight path angle (γ).

In order to simplify the trajectory approximation, the equations of motion are expressed in polar coordinates. The first step is to define the type of equations that are needed in each segment of the trajectory. Considering the number of boundary parameters that can be imposed in each trajectory, it can be seen that each equation should have two variables. The segment computed in Table 4 is not such case because the trajectory is completely defined by the initial conditions and the gravity. The computed values of radial velocity $\dot{r}$, and the radius r, and γ at the end of the segment are shown in Table 4.

From t=0s to t=5s		r_0 [m]	$\dot{r}_0$ [m/s]	Δt [s]
$\dot{r}$=	$\dot{r}_0 - g \cdot t$	6390140	147,078	5
$\dot{\theta}$=	$\frac{\dot{r}_0}{r}$	$\dot{r}_f$ [m/s]=	98,028	
Engines off		γ [rad]=	0,58789	
		r_f [m] =	6390752,766	

Table 4: Known and computed parameter values that define the Aldebaran trajectory from release to t=5 s.

When the fighter aircraft is sufficiently far from Aldebaran, the ignition of the first stage takes place. This trajectory equation depends on a, b, x and y (see Table 5 for parameter definition). a and b are computed with the boundary conditions, while x and y are adjusted manually. The first attempts were made with exponential equations such as

$$r = r_0 + \dot{r_0} \cdot t + a \cdot e^{b \cdot t}. \qquad \text{Eq. 61}$$

This form should be appropriate for the phases when the combustion is taking place because the launcher mass is decreasing. However, when Eq. 61 is used in combination with the boundary conditions shown in Table 5, the solutions are very unstable. These trajectories were quite constant at the beginning of the trajectory segment and had huge velocity increases with short time intervals at the end of the segment. This is the reason for adjusting x and y manually. They are set at values that provide acceleration functions similar to Ariane V and Pegasus (considering one function for each stage). Such similarity holds qualitatively but not quantitatively.

From t=5s to t=55s	**Δt [s]** = 50	**r_0 [m]**	6390752,77
First stage		**$\dot{r}_0$ [m/s]**	98,028
$\dot{r}$=	$\dot{r_0} + a \cdot t^x + b \cdot t^y$	**r_f [m]**	6404140
r=	$r_0 + \dot{r_0} \cdot t + \frac{a}{(x+1)} \cdot t^{x+1} + \frac{b}{(y+1)} \cdot t^{y+1}$	**$\dot{r}_f$ [m/s]**	665,5277
Δ$\dot{r}$ [m]	567,5	**Δr [m]**	13387,234
a=	21,2509	**x =**	0,5
b=	1,335E-06	**y =**	5

Table 5: Known and computed parameters that define the Aldebaran trajectory during the operation of the first stage.

The trajectory segment of the second stage has been computed with the same method as in previous segment. The results of the trajectory computation trajectory computation are illustrated in Table 6.

From t=55s to t=135s	**Δt [s]** = 80	r_0 [m]	6404140
First stage		$\dot{r}_0$ [m/s]	665,5278
$\dot{r}$=	$\dot{r}_0 + a \cdot t^x + b \cdot t^y$	r_f [m]	6478140
r=	$r_0 + \dot{r}_0 \cdot t + \frac{a}{(x+1)} \cdot t^{x+1} + \frac{b}{(y+1)} \cdot t^{y+1}$	$\dot{r}_f$ [m/s]	2384,808
Δ$\dot{r}$ [m]	1719,280	**Δr [m]**	74000
a=	8,3178E-05	**x =**	4
b=	-3,2962E-03	**y =**	3

Table 6: Known and computed parameters that define the Aldebaran trajectory during the operation of the second stage.

At the second stage cut off a 10-seconds free fall trajectory takes place. In this phase, the structure of the second stage is jettisoned.

From t=135s to t=145s	r_0 [m]	$\dot{r}_0$ [m/s]	**Δt [s]**
$\dot{r}$= $\dot{r}_0 - g \cdot t$	6478140	2384,808	10
$\dot{\theta}$= $\frac{\dot{r}_0}{r}$	$\dot{r}_f$ [m/s]=	2286,7077950673600	
Engines off	**γ [rad]=**	0,568665266779134	
	r_f [m] =	6501497,57795067	

Table 7: Known and computed parameters that define the Aldebaran trajectory from the burn out of the second stage to the ignition of the third stage.

After the free fall segment, the third stage ignites. At the end of this trajectory segment, the launcher is at the perigee of an elliptical orbit which apogee at 800 km altitude. The trajectory has been approximated with the same method as for the first and second stages. In this case, x and y must be adjusted by considering that γ and the magnitude of the velocity are monotonously increasing. See Table 8.

From t=145s to t=345s	**Δt [s]** = 200	r_0 **[m]**	6501497,578
Third stage		$\dot{r}_0$ **[m/s]**	2286,708
$\dot{r}$=	$\dot{r_0} + a \cdot t^x + b \cdot t^y$	r_f **[m]**	6628140
r=	$r_0 + \dot{r_0} \cdot t + \frac{a}{(x+1)} \cdot t^{x+1} + \frac{b}{(y+1)} \cdot t^{y+1}$	$\dot{r}_f$ **[m/s]**	0
Δ$\dot{r}$ [m]	-2286,708	**Δr [m]**	126642,422
a=	8,54934E+01	**x =**	1
b=	-1,64644E+02	**y =**	0.9

Table 8: Known and computed parameter values that define the Aldebaran trajectory during the first operation of the third stage.

At t=345s, the launcher has reached an altitude of 250 km and a velocity of 7.9 m/s. By taking into account that at this point $\dot{r}$=0, it has been possible to compute the values shown in Table 9. These parameters characterize the orbital arc between the end of the first operation of the third and the second ignition of the third stage.

$\mathbf{v_\pi}$=	7907,8 [m/s]
$\mathbf{r_\pi}$=	6628140 [m]
h= $r_\pi \cdot v_\pi$=	$52414 \cdot 10^6$ [m^2/s]
p=h^2/μ_E=	6892191 [m]
e=p/ r_π-1=	$3{,}98 \cdot 10^{-2}$ [-]
$\mathbf{r_\alpha}$=p/(1-e)=	7178155 [m]
$\mathbf{h_\alpha}$= r_α-R_E=	800 [km]
a=(r_π+ r_α)/2=	6903147 [m/s]
n=($\mu_E/a^3)^{0.5}$=	$1{,}1 \cdot 10^{-3}$ [rad/s]

Table 9: Intermediate orbit parameters.

The third stage reignites a few seconds after apogee passage. The purpose of this second ignition is to circularize the orbit. Since this manoeuvre is much shorter than the orbit period, we have assumed that it occurs at constant radius.

The complete trajectory has been computed in polar coordinates. Figure 37 shows the radius as a function of time. The radius only decreases few seconds after the apogee passage. Figure 38 illustrates the angle turned about the polar coordinate centre as a function of time. After 500s into the flight, its behaviour seems linear because the orbital eccentricity is very small.

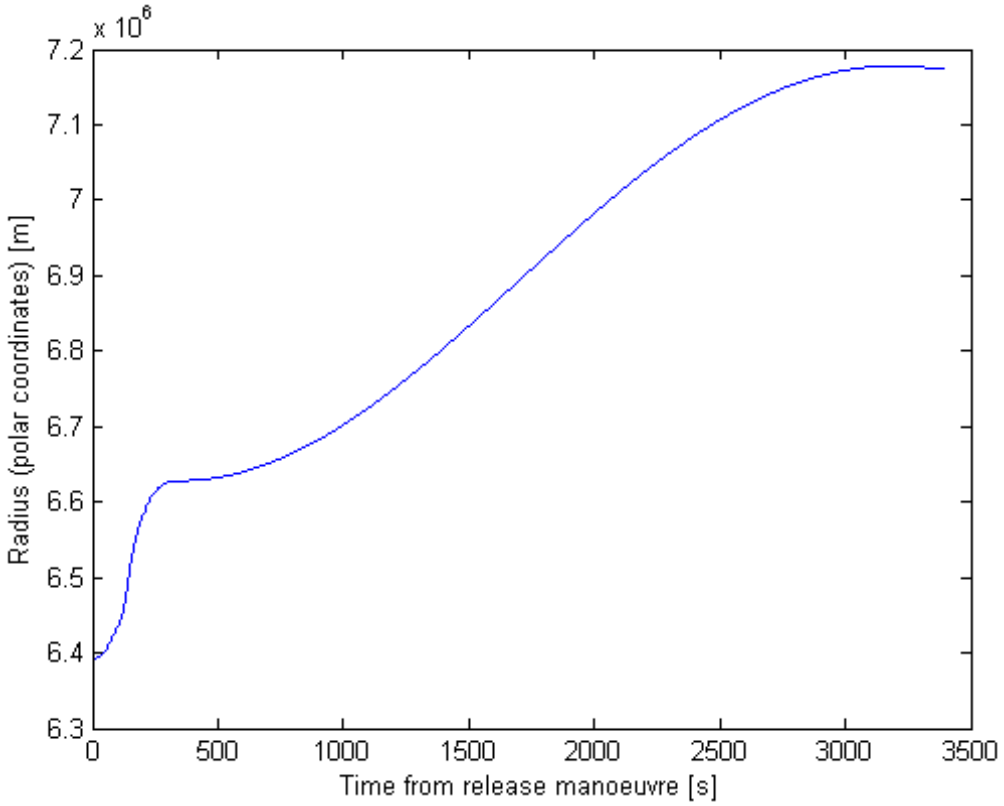

Figure 37: Radius as a function of time.

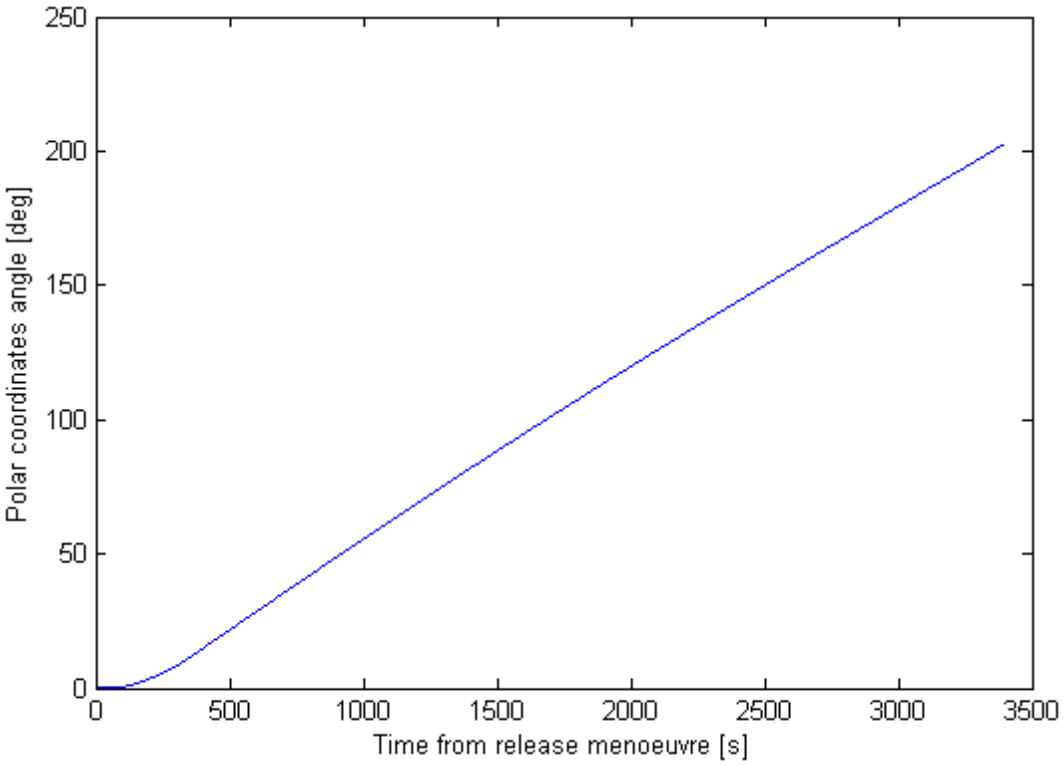

Figure 38: θ as a function of time.

Once the trajectory is defined in polar coordinates it is transformed into the Inertial Reference Frame. Figure 39 shows the trajectory of the launcher (blue) and the earth surface (red).

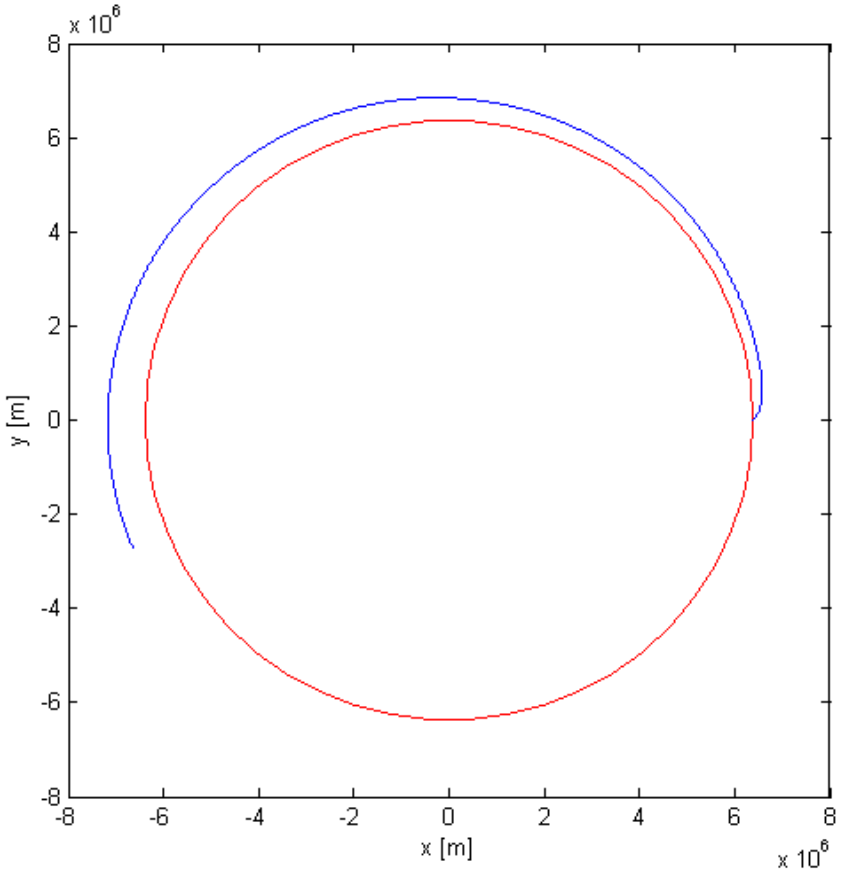

Figure 39: Representation in the xy-plane of the Aldebaran trajectory (blue) and the Earth (red)

The velocity is obtained by differentiation from the trajectory in the Cartesian Inertial Reference Frame. Figure 40 provides the magnitude of the velocity as a function of time. The velocity decreases in the free fall phases and during the intermediate elliptical orbit.

As a final remark, the velocity is continuous but not differentiable. In order to make the trajectory representative, some acceleration discontinuities have been defined. By this way, the effects of the activation of pyrotechnic devices (separations) and fast acceleration changes have been included in the model.

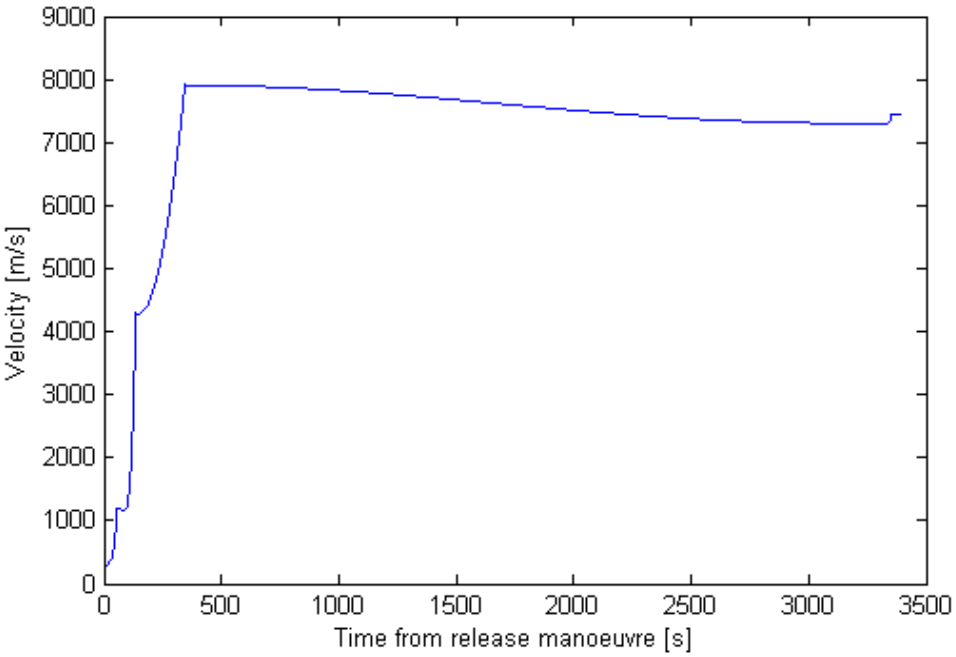

Figure 40: Magnitude of the velocity as a function of time.

Once the trajectory has been approximated, the attitude is also approximated. As previously mentioned, the turn rate values are representative of the real turn rates; however, they do not accurately represent the launcher attitude. As the aim of the project is to model the INS performance, the representative turn rate values have been adopted as inputs to the model.

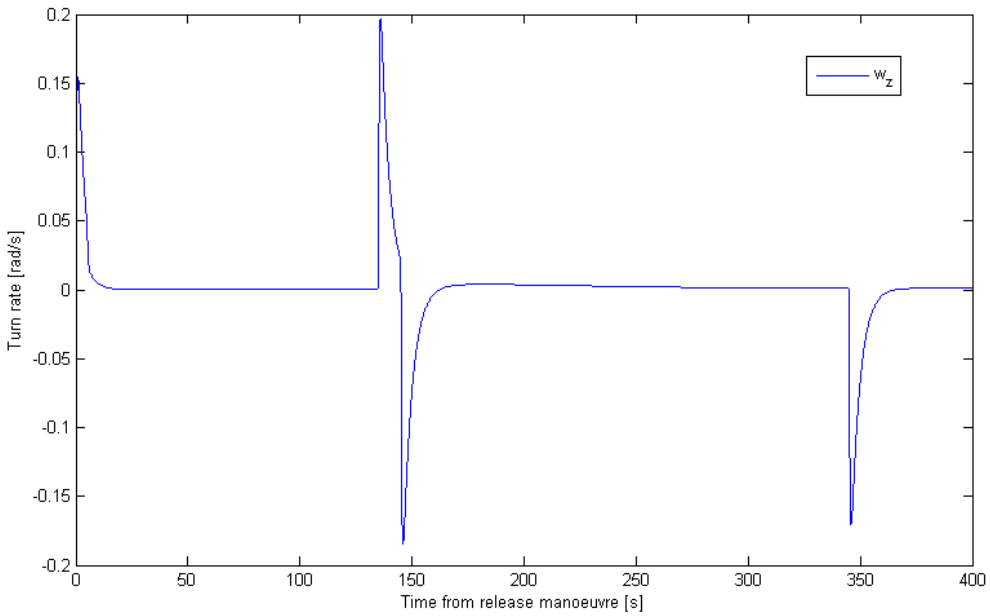

Figure 41: Turn rate about the z-axis in body frame as a function of time.

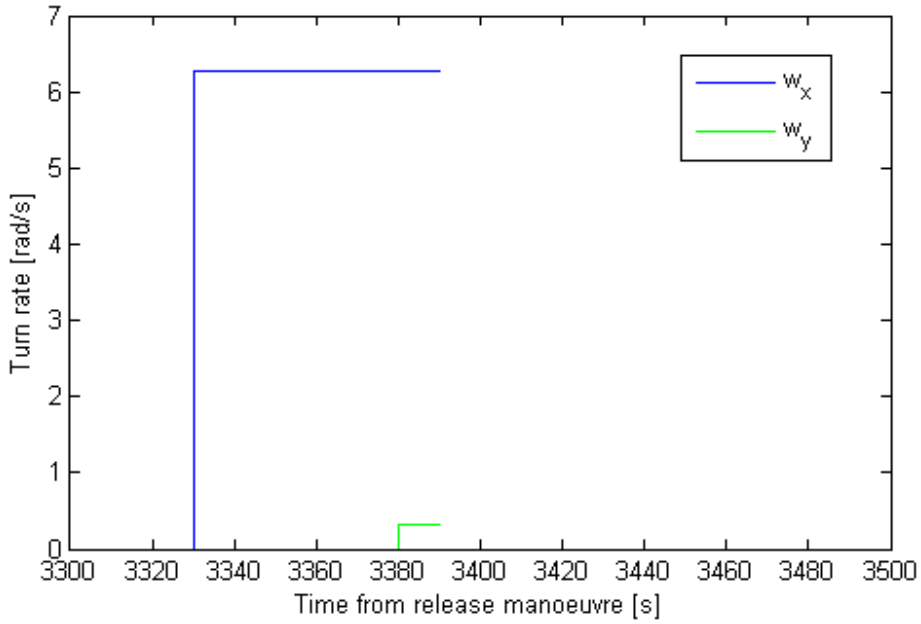

Figure 42: Turn rates about the x- and y-axes in body frame as a function of time.

Figure 41 and Figure 42 show the turn rate values about x, y and z (in body frame) in the most relevant time intervals: Figure 41 provide w_z at the beginning of the trajectory, while Figure 42 illustrates w_x and w_y at the end of the trajectory. w_x and w_y are nominally zero out of the represented part. w_x and w_y are not continuous functions. The reason why this decision has been made is that the INS should detect launcher attitude changes due to shocks or pyrotechnic separation of stages. w_z presents fast turn rate changes. As a consequence, the model inputs represent not only the nominal launcher operation, but also the launcher failure cases.

5.2 Random error modelling

There are two ways of modelling the random error, which are by means of either the dynamic or the group methods. Both techniques model the sensor random walk in a given vibration environment [21][19].

- Dynamic random walk modelling method consists in associating to each sensor output an error or a variance. Therefore, each sensor output has an associated ±Δg, where Δg is the maximum possible deviation with a given probability. This method is easy to validate and is applicable to all sensor types.
- Group random walk modelling method consists in making sensor output groups. It considers a signal post-treatment that groups sensor samples and associates to each group an output value and an error. In Figure 43 the sensor output reduction is represented. The basis of the method is the

Allan Variance but each sensor supplier uses its own adaptation of the method.

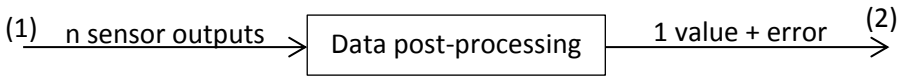

Figure 43: Schematic representation of the data flow in the group random walk

This type of model presents one advantage over the dynamic modelling; the random walk error associated to the sensor output is reduced significantly. However, the random walk error depends on the sample group size. In the case of small sample group sizes this associated error is not properly defined [19]. Furthermore, the sampling rate at 2 (Figure 43) should be three to five times the sensor bandwidth [19]. As a consequence of the huge data rate needed in 1 (Figure 43), the Modified Allan Variance was applied in some sensors. The Modified Allan Variance method does not reduce the data rate from 1 to 2. This method overlaps the groups and corrects the sensor output as a result of the n-previous outputs. The computation time increases and so does the quantization error. However, the random walk error is significantly reduced compared to the original Allan Variance method [18]. Nowadays the use of the Allan Variance and the Modified Allan Variance in MEMS accelerometers and gyros is being studied with the aim of providing more confident error approximations [18].

Since not all the sensor types can be properly modelled with the group random walk modelling it has been decided to use the dynamic random walk model. Another argument that supports this decision is that most sensors use internal signal post-processing that, depending on the required data rate, reduce the random walk dynamic error. IEEE Std. 952-1997 C.1.1 provides the formulas needed to transform between different random error definitions and the dynamic random walk [20].

Another issue to discuss related to the random walk error is the error distribution. Most inertial sensor datasheets use normal distributions in error modelling. However, there is not a standard to determine the standard deviation values. The inertial sensor suppliers should do many tests to correctly determine the standard deviation. These tests imply an increase of the calibration costs. In order to be able to offer a more competitive product, most sensor suppliers execute only about 15 tests. Then, they assume a series of hypotheses to determine the standard deviation. As a consequence of the fact that there is not a standard, each supplier uses the methodology that best suits to its product.

In this project, the type of distribution implemented is the uniform distribution. This implementation ensures that the sensor error is not underestimated.

Consequently, it is overestimated in all cases. Then, the estimated position error obtained with the model is worse than the real one.

5.3 Gravity model analysis

Here we evaluate the requirement listed in Section 3.3.3 concerning the gravity model approximation to be used in the INS algorithm. In other words, we check whether limiting the gravity field expansion to the J_2 zonal harmonic is acceptable. Figure 44 shows the time evolution of the difference in velocity between an INS algorithm limited to the J_2 term and one including terms up to J_4.

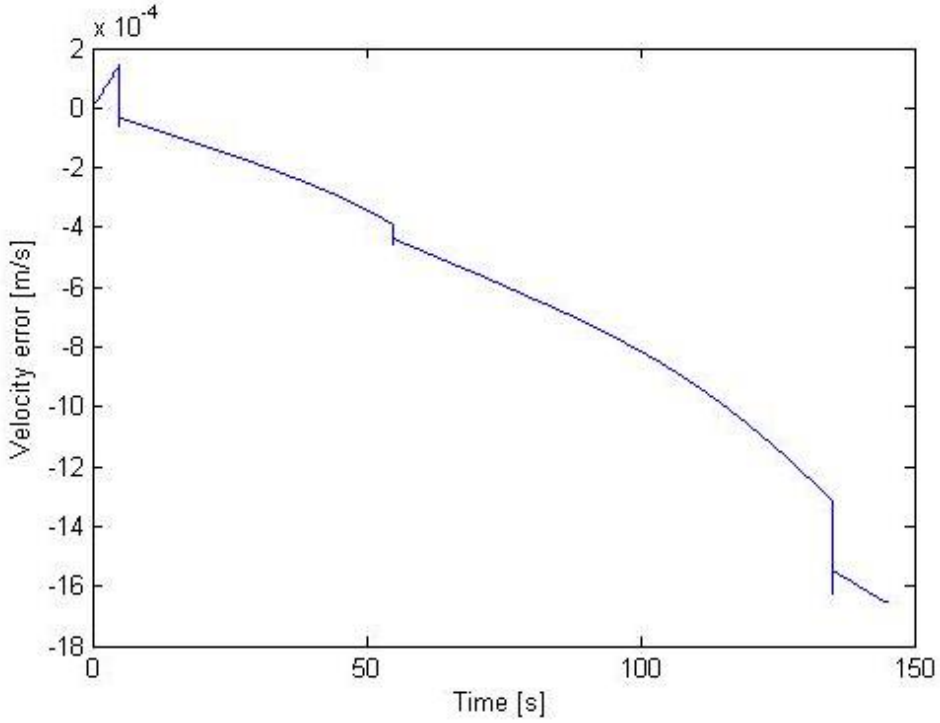

Figure 44: Error in velocity as a function of time.

The simulations made in order to obtain Figure 44 have the following characteristics:

- The model inputs are exactly the same.
- The hybridization with GNSS has not been activated.
- The calibration and random walk errors have been set to zero. The sensors are not affected by temperature changes.
- The junction of the host vehicle and the ISA is considered ideal.
- The errors in the sensor correction and INS algorithm loops have been set to 10^{-15}. Therefore, the error introduced in the computation process can be neglected.

- The error associated to signal digitalization is present in both models. The discontinuities in Figure 44 are due to this. The way the INS reacts to an acceleration discontinuity is slightly random. This random performance can be reduced by increasing the acquisition frequency. For the simulations corresponding to Figure 44 the frequency has been set to 100 Hz.

In Figure 45 the error caused by gravity discontinuities has been removed. As can be seen in this figure, the velocity error caused by the gravity approximation reaches 1.5 mm/s at t=145s.

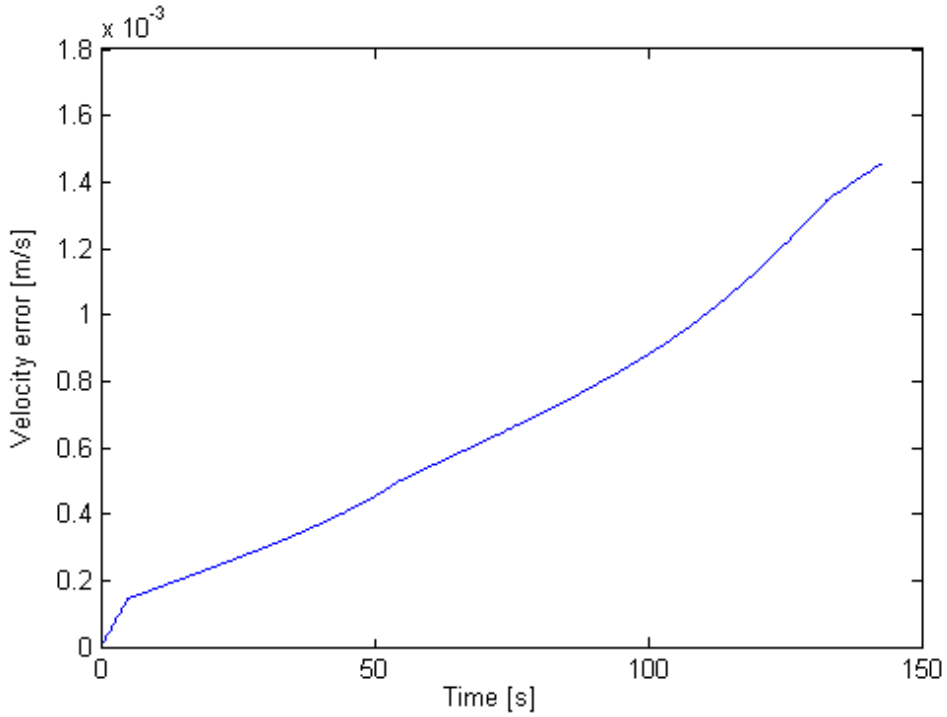

Figure 45: Velocity error due to gravity approximation as a function of time.

Taking into account the velocity error values show in Figure 45 and the fact that the GNSS hybridization can periodically set the velocity error almost to zero, the decision of using a gravity model limited to J_2 has been considered correct.

Another important point to discuss concerning the gravity model is the geocentric gravitational constant (μ). There are three options to evaluate: using the value computed considering the atmosphere, or the value computed without considering the atmosphere or computing the exact value at each position.

The launcher trajectory starts at 12 km altitude. Therefore, the densest atmosphere layers should always be included in the estimation of μ. Furthermore, the altitude of the launcher increases rapidly. Another fact to be taken into account is that neglecting the atmosphere at sea level causes a decrease in μ by

8.8 ppm. As a consequence, it has been decided to use a constant μ value in the model and to include the atmosphere.

5.4 Inertial navigation system assembly model

Section 4.7 introduced the error associated to the ISA assembly in the host vehicle. In the model this error can be introduced. However, this error source has been neglected in the simulations performed.

The Aldebaran launcher has reduced dimensions. The avionics must fit between the third stage and the payload. The diameter of this section of the launcher is 1 meter. The length is still undefined, although we can assume that will be short. Therefore, the hypothesis that the INS platform is fixed directly to the third stage structure can be considered valid. The third stage structure can be considered ideally rigid. Therefore, the assembly between the INS platform and the host vehicle can be neglected.

The other transfer function that can distort the ISA sensed acceleration is that related to the ISA and INS platform assembly. This assembly is done with an elastic coupling in order to isolate the ISA from high acceleration shocks. As stated at the beginning of this section, the distortion in the simulations has not been taken into account. However, the users can introduce the transfer function. The transfer function can be introduced in the model input parameters list. By default, it is a second-order transfer function.

Eq. 62

$$G(s) = \frac{K\omega_n^2}{s^2+2\cdot\varepsilon\cdot\omega_n+\omega_n^2}.$$

Where:

- G(s) is the transfer function
- K is the proportionally factor. In this case it is always set to 1
- ω_n is the natural frequency of the ISA and the INS platform junction
- ε is the damping ratio

Depending on the value of the damping ratio, the systems can be classified according to four response types:

- The undamped systems have null damping ratio. This means that the system oscillates perpetually when it suffers an input change. This type of system is ideal and does not exist.
- The underdamped systems have $\varepsilon < 1$. The output reaction to a step input function is an oscillation with decreasing amplitude.

- The overdamped systems have $\varepsilon > 1$. The output reaction to a step input function does not oscillate. It monotonically tends to the stationary solution. These systems are characterized by the delay that they introduce in the system.
- The critically damped systems have $\varepsilon = 1$. Their output does not oscillate to a step input. These systems are characterized by the fastest response among those for which the output does not overtake the stationary value.

The damping ratio in the transfer function must avoid values close to zero and values that increase a lot the delay. Consequently, if a model user needs to take into account the transfer function of the ISA and INS platform junction, the damping ratio should be around one.

6 Model implementation

6.1 Mission estimated profile

The approximation and the implementation of the trajectory are the subject of Section 5.1 . However, there are other external factors of the INS that also determine the ISA performance. The environmental conditions are some of such external factors.

6.1.1 Vibration and shock environments

The frequency and amplitude of the vibrations determine some characteristics of the inertial sensor. The ISA is isolated from most high frequency vibrations by the quasi-rigid assembly.

The vibration environment has two main sources: the motor operation and the acoustics acting on the launch vehicle. Acoustic driven random vibration is not easily determined before launch. Most launcher manuals provide an acoustic vibration envelope determined in the worst vibration case. Motor burn vibrations can be determined either by doing an engine operation study or experimentally. They have a narrow frequency range (for example, the Minotaur IV range is 10 Hz). Usually, each stage has its own frequency range. Typically, the frequency spectrum of the acoustic driven random vibration starts beyond 250 Hz. Therefore, it is potentially removable thanks to the fact that the ISA with the quasi-rigid assembly can be insensitive to this class of vibration.

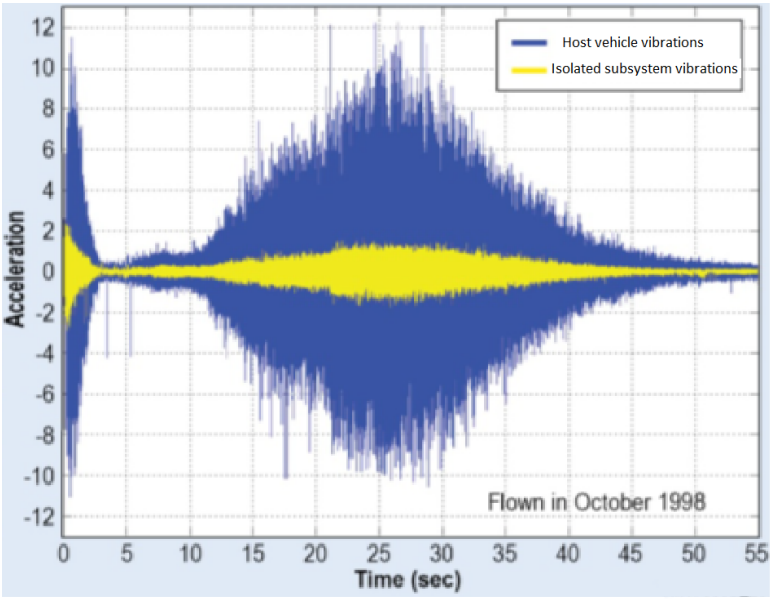

Figure 46: Measured vibrations in a Minotaur IV launcher in an isolated launcher part and in a launcher structure [12]. From other figures from the launcher's manual it can be inferred that the acceleration units are m/s^2.

Figure 46 shows in a time period of 55 seconds, the host vehicle vibrations and the vibrations in a subsystem that has been isolated from host vehicle vibrations with a quasi-rigid subsystem assembly. The data shown apply to the Minotaur IV flight profile.

Since the sensor performance deteriorates when the vibration amplitude increases, such degradation must be specified in the worst predicted vibratory environment. Consequently, the inertial sensor performance is defined with a safety margin. The option of measuring the acceleration with accelerometers specifically designed for this purpose and then correcting the output of the navigation inertial sensors is not feasible. The reasons are that this would imply three additional sensors and that it would be difficult to measure the vibrations and apply the corresponding signal corrections in real time.

The shock environment is modelled with velocity discontiuities. Such discontinuities are placed at the times of stage separation. It has been considered that the other shocks do not affect the ISA thanks to the quasi-rigid assembly.

6.1.2 Temperature environment

In most launchers the temperature of the avionics module is controlled by the launcher thermal control system. Furthermore, launchers use passive thermal control systems in order to reduce the heat flux to the payload and avionics modules.

The heat sources are the engine operation and the aerodynamic interactions. The latter mainly affect the payload fairing, whereas the most relevant contribution of the former type is associated to the operation of the third stage due to its proximity. Aerodynamic interactions depend on the dynamic pressure. The Pegasus launcher experiences the maximum heat flux in the avionics module approximately when the maximum dynamic pressure is reached [11]. Thanks to the similarity between the Aldebaran and the Pegasus launchers, it can be assumed that the corresponding heat fluxes are similar. Consequently, the ISA heat flux depends on time. The temperature is measured with a determined time interval and the refrigeration system is regulated to maintain the avionics module temperature as constant as possible.

The selection of the sensor temperature must be carried out considering precision and time response. Fluid expansion devices are very stable and precise, but the data is difficult to digitize and they have very low response. Thermocouples are inexpensive, rouged and have a wide temperature range, but they are very inaccurate. Integrate-circuit devices are very slow compared to

other sensor types. Infrared devices are very inaccurate. Resistance temperature devices are expensive, they need a constant current source, they are self-heating and their delay is not negligible. However, they are the most stable and accurate. For this reason, we assumed a resistance temperature device for the ISA.

As a consequence of the temperature variation, the sensor delay and the temperature sensor precision, the temperature error must be taken into account in the INS model. One of the inputs of the model determines the temperature acquisition frequency. Another input corresponds to the temperature error. The temperature error value is the sum of sensor error and the error due to the time delay.

6.2 Redundancy

Redundancy in an INS can be achieved in two different ways. Both ways are explained in the case of tolerating one sensor failure.

- The first way to reach some degree of redundancy is to use ISAs in a non-orthogonal configuration. An example is a 4 sensor configuration with 120º separation between measurement axes. This configuration is not commonly used. The sensors signal post-treatment output is the acceleration and turn rate in three axes. The difficulty of the signal post-treatment remains on the fact that the accelerations that affect the sensors must be computed in sensor axes and consequently, each acceleration component depends on the other three sensor measurements. Then, the signal post-treatment becomes more complicated to handle because if good precision values are required, the computation time increases a lot compared to the case of orthogonal ISA.
  The detection of sensor failure is quite complicated due to the high coupling between sensor outputs. When a sensor failure is detected, the sensor output post-treatment changes.
- The other way to reach the required redundancy is to duplicate all the sensors. This means that two equal ISAs should be equipped in the avionics module. This option implies 12 inertial sensors (6 accelerometers and 6 gyroscopes), while the previous redundancy option implies only 8 sensors (4 accelerometers and 4 gyroscopes). However, the use of two ISAs has some benefits. The first one is that there is no need to determine which sensor has failed because when an error in the ISA output is detected, the INS algorithm uses the output of the other ISA. The other benefit is that in case of not having any failure, the ISAs outputs can be

averaged in order to reduce the random error consequences to the estimated position and velocity values. As a result, the INS accuracy improves.

In the INS model the option of an ISA in non-orthogonal configuration is not implemented. The reason to restrict the model to orthogonal sensors is that, in the case of non-orthogonal angles, the sensor that has failed is difficult to determine due to the high correlation between sensor outputs. The failed sensor should be found by a probabilistic analysis.

6.3 Altitude sensor implementation

As explained in section 4.3 , the vertical channel instability is one error source that does not depend on sensor selection. The source is the gravity gradient, which is always decreasing when the altitude increases. The consequence of this gradient is that a small error in altitude increases with time. The reason why this error always increases is that an error in altitude implies an error in the gravity approximation. For example, if the altitude is underestimated, gravity is overestimated because the estimated position is closer to the Earth than the real position. As a result, an extra acceleration is computed in the vertical direction. Consequently, the altitude error increases with time. Figure 47 schematically shows this concept.

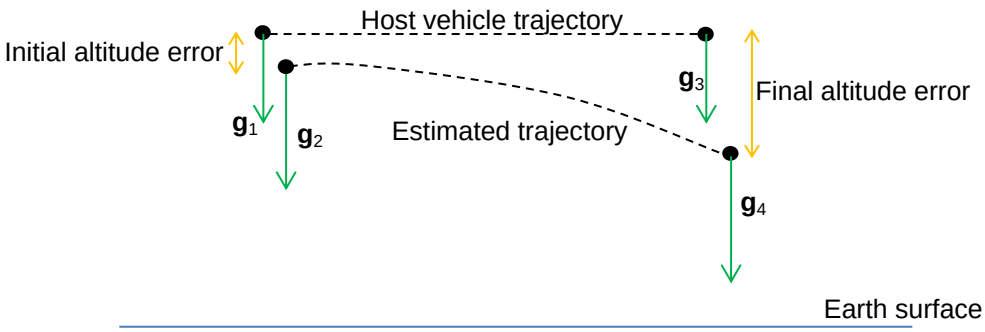

Figure 47: Shematic representation of the vertical channel instability in the case of initial estimated altitude smaller than the host vehicle real altitude. g_1 and g_3 are the gravity vectors in the initial and final host vehicle positions. They are equal. g_2 and g_4 are the estimated gravity vectors in the estimated initial and final positions. $g_1 < g_2$ and $g_2 < g_4$. As a consequence, the altitude error increases with time.

Vertical channel instability is the reason why the “free inertial specifications” are usually only provided by the INS supplier in horizontal position/velocity errors.

The way in which the altitude error increases can be approximated by [A-3]:

$$\Delta h(t) = \Delta h(t_0) \cdot e^{\sqrt{\frac{gravity}{r}} \cdot (t - t_0)} \quad , \qquad \text{Eq. 63}$$

where r is the distance of the host vehicle from the center of the Earth, $\Delta h(t_0)$ is the initial altitude error, gravity is the average gravitational acceleration in the given time interval, t_0 is the initial period time and t is time. Figure 48 shows the altitude error due to the vertical instability as a function of time in the case of average gravity magnitude and radius values for the Aldebaran trajectory and an initial altitude error of 7 meters.

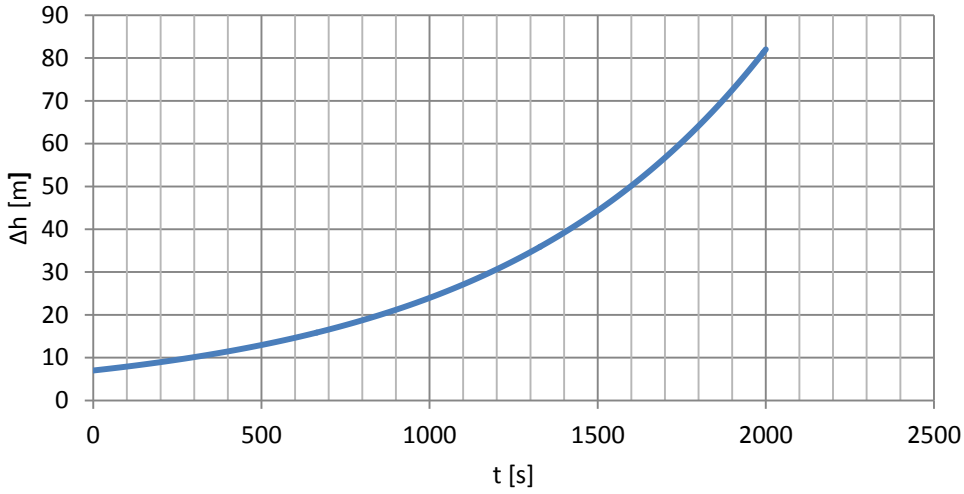

Figure 48: Altitude error due to vertical instability as a function of time.

In the case shown, after 30 minutes the vertical instability error is 64.1 meters. At the same time, the velocity error is 0.08 m/s, which is greater than the maximum permitted velocity error.

The vertical channel instability can be solved by adding an altitude sensor. This solution implies adding at least two sensors in order to have some redundancy. The navigation algorithm should be modified in order to account for this additional input, and a Kalman filter should be added. The Kalman filter is an algorithm that combines different redundant inputs in order to obtain a combined non-redundant output. The Kalman filter is also used for reducing random sensor responses.

The Ariane and Vega launchers do not use altitude sensors. These launchers reduce the vertical channel instability by reducing the initial error. Their INS is sufficiently precise to neglect the vertical channel instability.

The Aldebaran launcher does not need an altitude sensor not because its INS is very precise, but because the GNSS hybridization periodically reduces the error. Therefore, the vertical channel instability does not significantly affect the navigation algorithm estimations.

6.4 Release operation considerations

The release operation is one of the most critical mission phases. The main reason is the operation by itself, because the manoeuvre must be done precisely in order to place the launcher in the correct trajectory. Another reason is that the fighter aircraft has to transmit the position, the velocity and the attitude of the launcher to the launcher. This transmission cannot be done directly with the fighter data. The main reason is that the fighter and the launcher supports become deformed due to the action of aerodynamic forces and torques. This problem can be solved in one of the following three ways:

- By precisely computing the fighter dynamics during the release operation and adding the pre-introduced values to the fighter measurement. This option has the drawback that it is difficult to precisely compute the launcher position and attitude because the fighter operation is unsteady. Furthermore, wind gusts can alter the computed corrections.
- By precisely determining the position and attitude of the launcher's ISA with respect to the fighter's ISA. This can be done by optical comparators or laser trackers. The data recorded by such sensors should correct the fighter data in order to send the position and attitude of the launcher's ISA to the launcher. Nonetheless, this option has the drawback that the fighter has to be modified to equip these sensors and the software for the communications with the payload must also be changed. Fighters are equipped with software to send the position and attitude to missiles before launching them.
- By initializing the launcher INS before the fighter's take off. This option has strong impact on the launcher design because of the power consumption increase. Such increase can be compensated by a higher number or bigger batteries on the launcher or by connecting the launcher EPS with the carrier aircraft during the captive flight. This second option implies modifying the fighter standard interface, which does not allow powering the payload before being armed for launch. Moreover, safety implications of having the launch vehicle armed during captive manned flight should be carefully analysed [27].

  Furthermore, the launcher is placed under the fighter, and then, the launcher cannot receive properly the GNSS data because the fuselage masks the GPS antenna. Therefore, the navigation system should be designed to operate from the take-off to thirty-five seconds after the release manoeuvre only with the INS. This fact implies that the INS performance requirements increase significantly. Furthermore the ISA should withstand different environmental conditions during its operation.

Taking into account these drawbacks, we have decided that this option is not going to be implemented in the model because its implementation is not feasible in the Aldebaran project.

The effect of the first two options on the navigation system is an error in the initial position and velocity. Since the modelling of the Aldebaran launcher release operation is not within the scope of this project, the maximum error values have not been computed. Nonetheless, in section 8.1 the conclusions of the sensitivity analysis on the precision of the initial position are presented.

In description of the third option, we said that the launcher could not use GNSS data until 35 seconds after the release. This data has been obtained with currently hybrid GPS-INS used in guided missiles and bombs [27]. Of these 35 seconds, five correspond to the time interval in which the GPS system is not operating due to the proximity to the fighter. During these proximity instants the risk of GPS multipath interferences is high. The remaining 30 seconds correspond to the GPS initialization.

By taking into account the initialization error and the initial time interval without GNSS data it can be deduced that the worst INS performance occurs at the end of the gap of GNSS data. Figure 49 and Figure 50 should confirm this deduction. In fact they do not: at the end of the trajectory (t = 3345s), position and velocity estimation errors are quite large.

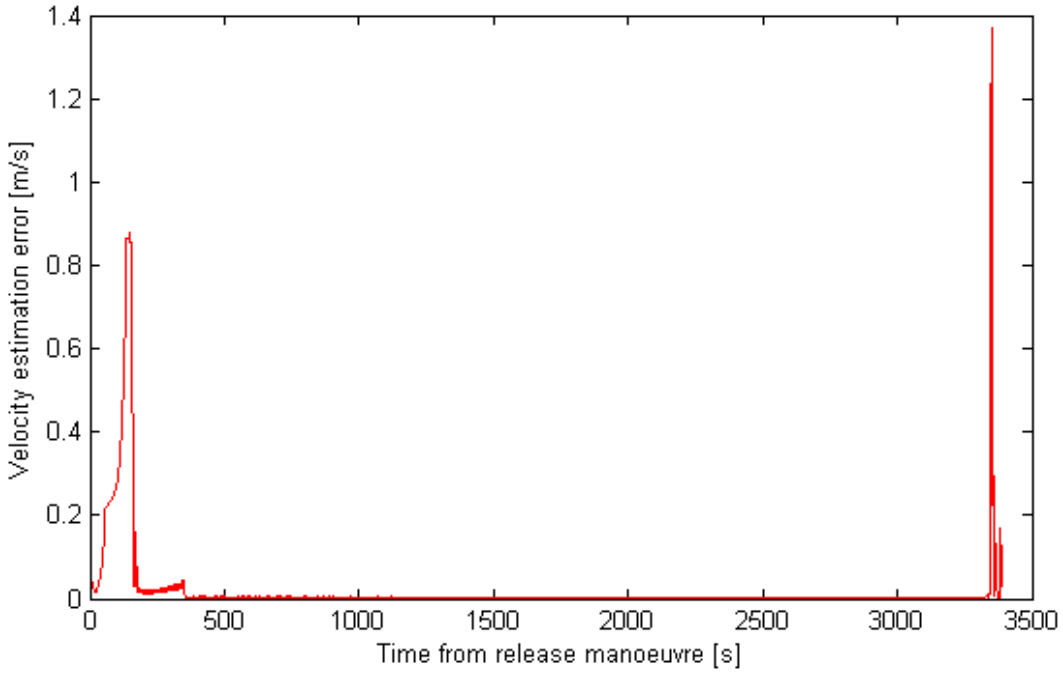

Figure 49: Magnitude of the velocity estimation error as a function of time. In this simulation, the initialization error is set to zero and the sensor performance has not been considered ideal (the reader is referred to Annex B for additional information concerning the simulations).

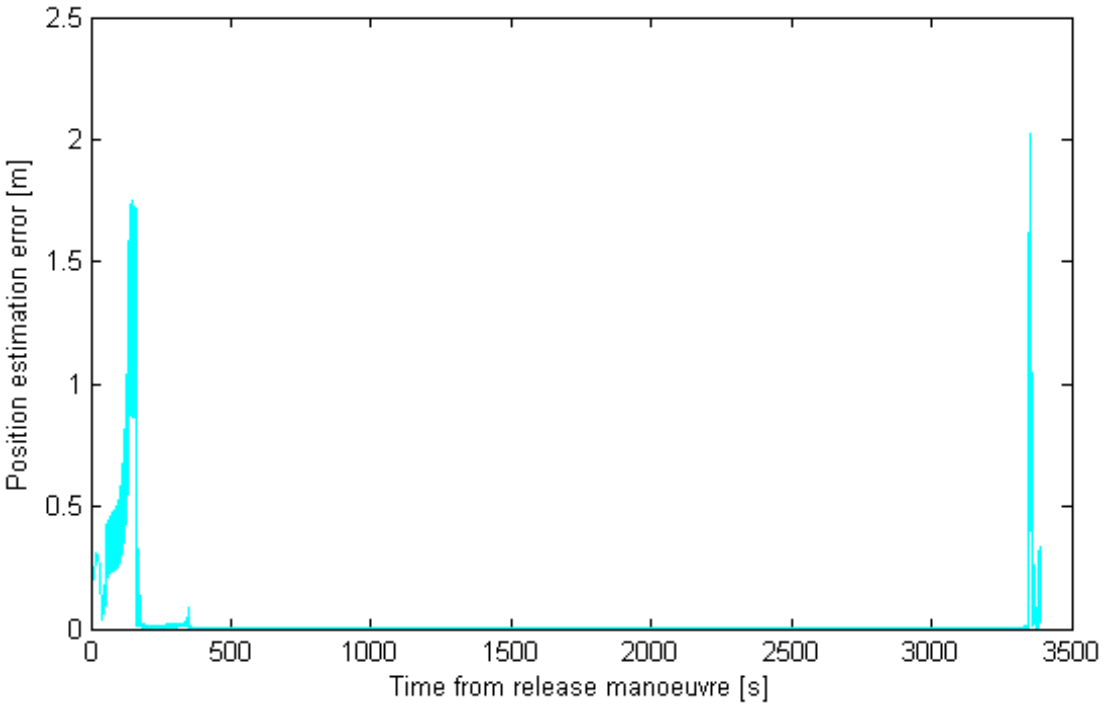

Figure 50: Magnitude of the position estimation error as a function of time. In this simulation, the initialization error is set to zero and the sensor performance has not been considered ideal (the reader is referred to Annex B for additional information concerning the simulations).

The reason for such increase in the error in this phase is related to the turn rate values. In the estimation made in section 5.1 for the turn rate, the spinning frequency imposed about the *x*-axis was found reasonable. Nonetheless, the turn rate value imposed around *x*-axis is 3.6 times larger than the maximum measurable turn rate in the Ariane V ISA[22]. Therefore, the error may be caused by large turning rates which cannot be completely corrected by the attitude and acceleration computation algorithm (section 4.6). If this hypothesis is correct, an increase in the INS frequency would imply an improvement in the INS performance at the end of the trajectory. The results shown in Figure 51 and Figure 52 were obtained from a simulation performed with an INS frequency larger than used in previous simulations.

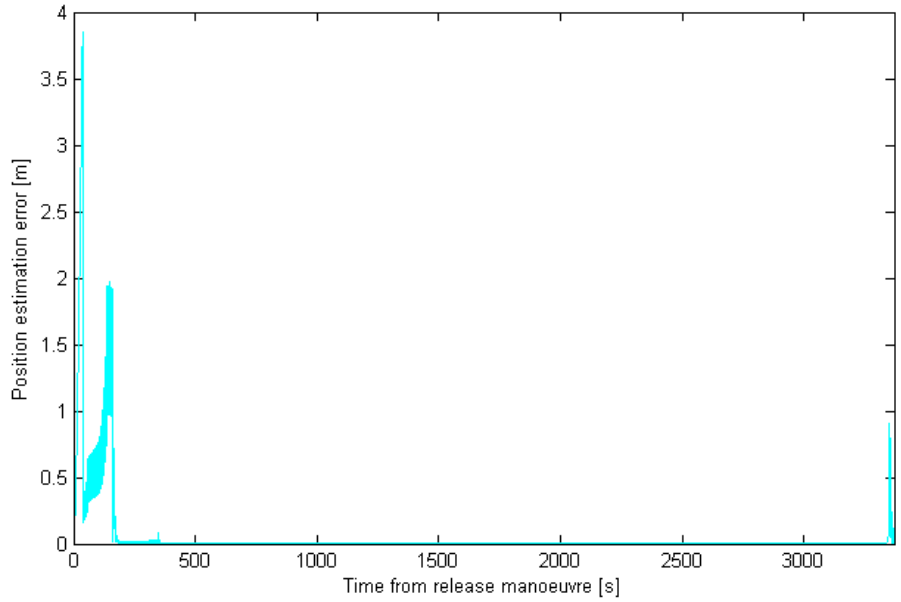

Figure 51: Magnitude of the position estimation error as a function of time. The simulation inputs are the same as in the inputs to the simulations of Figure 49 and Figure 50 except for the INS frequency, which is twice as much (consult Annex B for more information on the simulations).

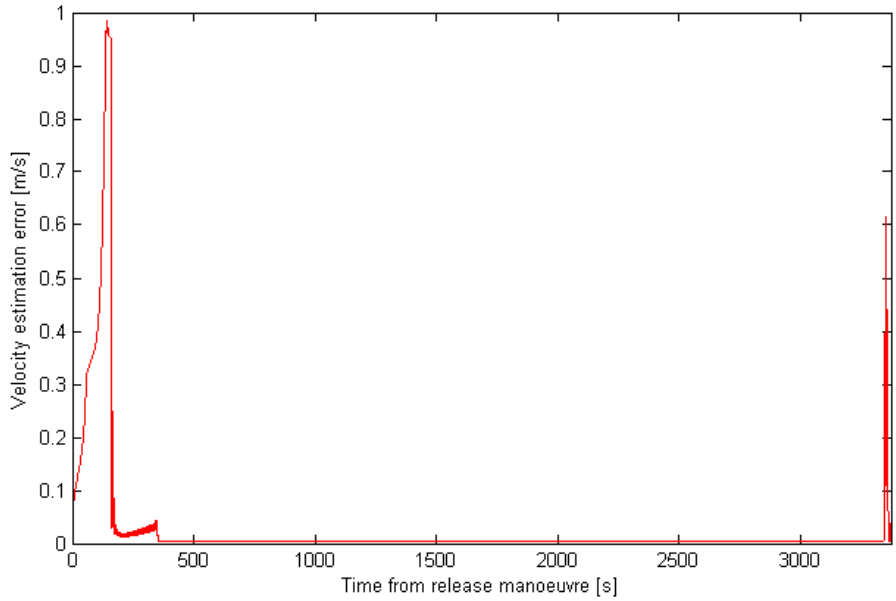

Figure 52: Magnitude of the velocity estimation error as a function of time. The simulation inputs are the same as in the inputs to the simulations of Figure 49 and Figure 50 except for the INS frequency, which is twice as much (consult Annex B for more information on the simulations).

The simulation of Figure 51 and Figure 52 and that of Figure 49 and Figure 50 use the same sensor properties. Nonetheless, the random errors in calibration lead to differences in the INS performance. Although the INS performance changes, one can appreciate that the final trajectory error has been significantly reduced compared to the maximum error in the first seconds of the trajectory.

6.5 Inertial navigation systems-Global navigation satellite system integration

As discussed in section 4.8 , the model uses an uncoupled INS-GNSS integration. In the present section, we describe three design options for the integration algorithm that we have designed and analysed.

6.5.1 Position update

In this design, the position is updated with the GNSS data. It must be taken into account that GNSS and INS data can arrive at different times to the position computing algorithm. Therefore, the position update cannot be done by updating the position at the instant in which the GNSS data is received.

If the GNSS data arrives later than the INS data, the position computed by the INS is saved between GNSS data receiving instants. Then, when the GNSS data arrives, the position at the time the GNSS data was obtained is corrected and, with the INS saved data, the current position is obtained. In turn, if the INS data has a delay, the previous procedure is unnecessary because the GNSS data can be saved until the corresponding INS data arrives.

6.5.2 Modified position update

With the simple position update, the INS error accumulated between the GNSS measurement and the GNSS correction is always included in the applied position correction. Therefore, the position error is never zero. In order to further reduce the position error, we have proposed to estimate the error accumulated between the GNSS measurement and the position update. The estimation is made as a function of the error increase between the two last position updates. It has been considered that, if more data is used in the estimation, the position update between trajectory segments (where acceleration discontinuities have been introduced in order to simulate pyrotechnic devices and shocks) would lead to high position update errors.

6.5.3 Position and velocity update

The position and velocity update algorithm uses the corrections obtained with one of the previous detailed algorithms to detect the velocity error. The velocity correction is determined every four GNSS data updates. The velocity update frequency could be the double of the frequency utilised. However, we have considered that high frequencies of velocity update would lead to velocity instabilities. Up to t = 345s there are large acceleration changes, and correcting velocity at high frequencies would lead to velocity correction overestimations and underestimations.

6.5.4 Algorithm selection

The previous sections describe the three different ways for integrating INS and GNSS. In the present section, we analyse which option should be used.

The first thing that must be analysed is the position update. Figure 53 shows the time evolution of the estimate position error. Both simulations had exactly the same inputs and the only difference was the navigation algorithm position updating. In both cases the maximum error was less than 0.45 m. Such precision has been obtained thanks to the fact that the GNSS error has been set to zero. The sensors have been considered ideal and the temperature is also measured without any error. Therefore, in the simulations corresponding to this section the only error source considered is the navigation algorithm error.

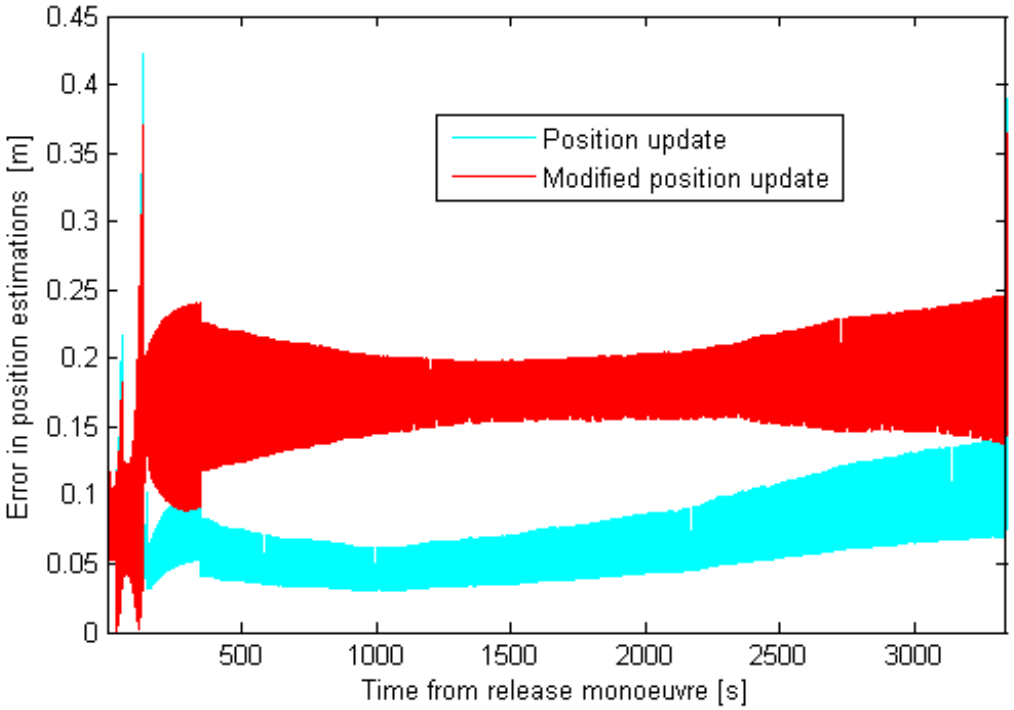

Figure 53: Magnitude of the position estimation error as a function of time (consult Annex B for additional information concerning the simulations).

As shown in Figure 53, the modified position update algorithm overcorrects the position. Therefore, we adopted the position update algorithm for the model.

Then, the velocity update must be analysed on the basis of the selected position update algorithm. Figure 54 shows the time evolution of the estimated velocity error in the case of using the GNSS velocity correction and in the case of using only INS data to update the velocity.

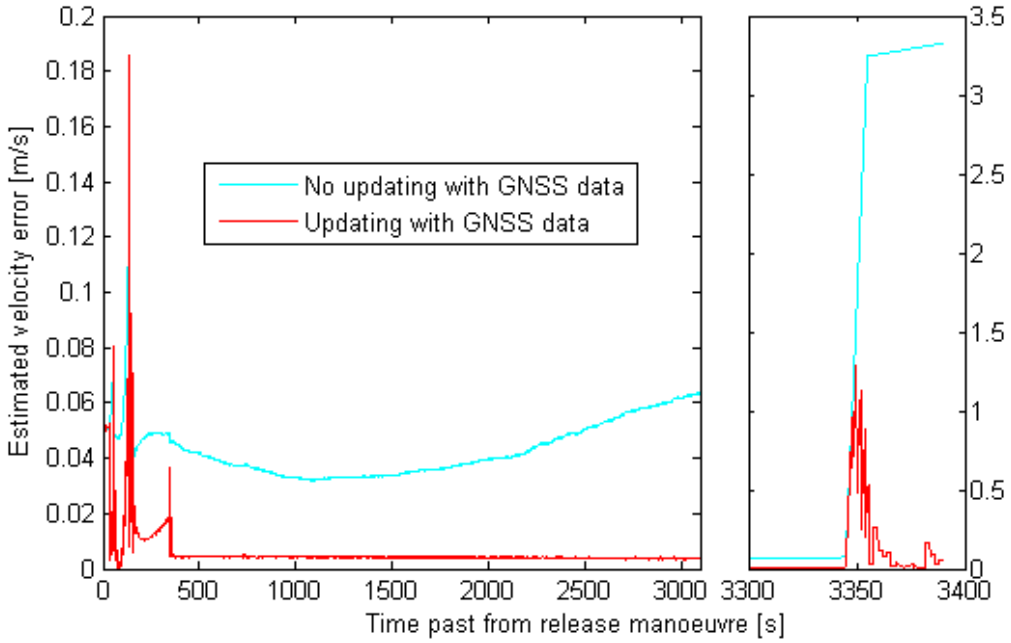

Figure 54: : Magnitude of the velocity estimation error as a function of time (consult Annex B for further information concerning the simulation).

Figure 54 tells that velocity updating with GNSS data significantly improves the INS precision. Nonetheless, this algorithm deteriorates the INS performance at the instants when the trajectory has high acceleration changes. Another advantage of updating the velocity with GNSS data is the improvement of the INS performance at the end of the trajectory, where the host vehicle undergoes large turn rate values, as described in section 6.4 . Such improvement can be seen in the right side of Figure 54.

Despite the INS general performance improvement, the INS performance deterioration has been considered non-acceptable when there are large velocity changes. Taking into account that the large acceleration changes are concentrated in the first 135s and the shocks are also concentrated there, it has been found interesting to test an hybrid algorithm that uses the GNSS data to update the velocity for t>137s. Figure 55 shows the time evolution of the velocity estimation error for the three options (GNSS updating, GNSS updating or hybrid).

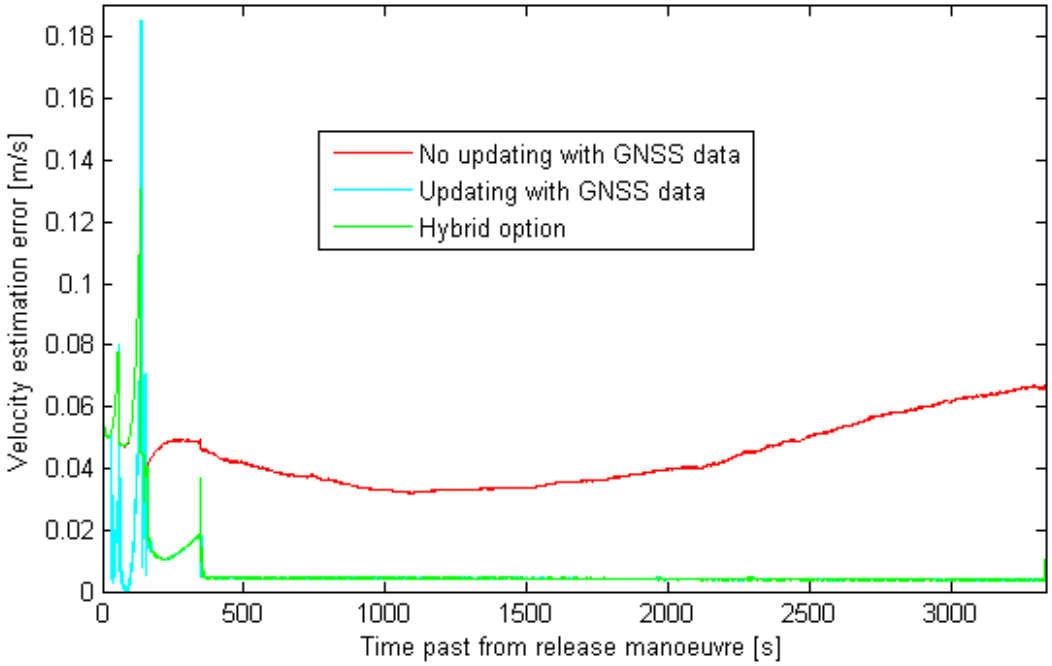

Figure 55: Magnitude of the velocity estimation error as a function of time at the end of the trajectory (consult Annex B for further information concerning the simulation).

Figure 55 shows how the hybrid option improves the INS performance. In the first trajectory phases, when the launch vehicle can undergo large accelerations changes and shocks, the GNSS data is not used in the velocity integration but, past this time, the GNSS data is used the integration. Hybrid option improves INS performance without destabilizing the INS performance in the first trajectory segments.

By default, the implemented options in the model are simple position correction and hybrid velocity correction. Attitude corrections have not been implemented because they need a more detailed analysis. Due to the GNSS errors, the attitude corrections could lead to attitude errors that consequently would deteriorate the INS performance. Therefore, a better INS-GNS hybridization should be made. The INS-GNSS integration is out of the scope of this project. As a consequence, the required development of the INS-GNSS hybridization for attitude corrections is not going to be carried out in this project.

6.6 Model description

The model is divided in seven parts:

- **Model initialization**: In this part, velocity and acceleration are computed in the inertial reference frame. Then, the direct cosine matrix is computed and the acceleration vector is transformed to body reference frame. The model parameters (host vehicle assembly parameters, INS characteristics

and sensor performance) are defined in another file. The reason why the parameter definition is made in another file is that the sensor calibration uncertainties can be maintained between different simulations. If the parameter definition were done in the model, the sensor performance would be different in each simulation.

- **Host vehicle model**: This part models the ISA-host vehicle assembly. All the simulations in this report have been executed by considering a rigid assembly.
- **Gravity subtraction part**: It uses the model initialisation position to compute the gravity acceleration. Then, the computed vector is subtracted from the sensed acceleration vector.
- **Sensor response model**: This part differentiates the turn rate. Up to this operation, the time step used is the model time step, a variable defined by the user. Thereafter, all the signals are combined in order to obtain the sensors output signals. This operation is done at the INS frequency. The sensor specifications used are the 'real' ones. They are different from the calibrated specifications due to calibration uncertainties.
- **Sensor corrections model**: This block uses the outputs of the sensor response subsystem. This block models the signal digitalization, which has been considered ideal, because computational efforts are not analysed in this report. Then, the signal correction algorithm has been implemented. This algorithm computes the sensor inputs with the sensor outputs and the calibrated sensor specifications by an iterative process. This algorithm solves the equation system with a specified precision.
- **GNSS model**: Its input is the position, which comes from the model initialization part. Its output has a different frequency than the INS frequency. The subsystem output has an associated error that has been modelled as a function of time. As declared in the scope of the project, to precisely model the GNSS is the scope of another GTD proposed project.
- **INS algorithm subsystem**: This block uses the GNSS and sensor corrections subsystem outputs and computes position, velocity, acceleration and turn rate in the inertial reference frame, and the attitude quaternion and the direct cosine matrix between body and inertial reference frame. The first step done is the attitude computation, which takes into account that the measurement axis change when the host vehicle rotates, as described in section 4.6 . Then, the velocity increment *dv* measured by the accelerometers is computed. The computation of *dv* takes also into account the fact that measurement axis change. Attitude and *dv* are used in the position-velocity-gravity loop, which is an iterative algorithm that uses the previous position and velocity. Previous position

and velocity are provided by the GNSS hybridization block, which updates periodically position and velocity with GNSS data.

7 Model Validation

The model validation has been divided in three parts: the attitude, the trajectory and the INS-GNSS hybridization. Each part adopts its own tests and simulations.

7.1 Attitude validation

The attitude validation consists of the following list of tests:

- Ideal simulation
- Sensitivity to INS frequency
- Sensitivity to attitude functions
- Sensor calibration errors
- Sensor temperature error
- Sensor random walk error

All the simulations use the same trajectory and attitude functions.

$$\boldsymbol{Position} = [10^{-3} \cdot t^3 \quad 0 \quad 0] \ [m]. \qquad \text{Eq. 64}$$

$$\boldsymbol{Turn\ rate} = [10^{-2} \cdot \cos\left(\frac{t}{10}\right) \quad 0.8 \quad 10^{-3} \cdot t] \ \text{[rad/s]}. \qquad \text{Eq. 65}$$

They are different from the standard simulation functions with the aim of simplifying the analysis of the results. Eq. 1 is expressed in the inertial reference frame and Eq. 65 in the body reference frame. Turn rate functions are changed in the test of sensitivity to attitude functions.

The use in the gravity subtraction block of a gravity model different from the model used in the INS algorithm is a source of error. Moreover, gravity does not influence the attitude. Furthermore, the simulations do not take into account gravity.

The accelerometer performance has been defined ideal in all simulations here presented. The tests on the sensor temperature error and the sensor calibration errors are executed by taking into account only one gyroscope specifications parameter. The parameter used is the scale factor. It has been found representative for all gyroscope specification parameters because in the model they are used as a block; if there was an error in the model, all the specifications would be affected.

7.1.1 Ideal simulation and sensitivity to INS frequency tests

The test called ideal simulation consists in executing a simulation with ideal ISA properties, with a large value for the INS frequency and with negligible values (of

the order of 10-20) for the accuracy of the iterative algorithms. Such test is difficult to execute due to the high processing time. As a consequence, we have decided to perform a set of simulations with different INS frequencies, f. Consequently, the Ideal simulation and the INS frequency sensitivity tests are carried out simultaneously.

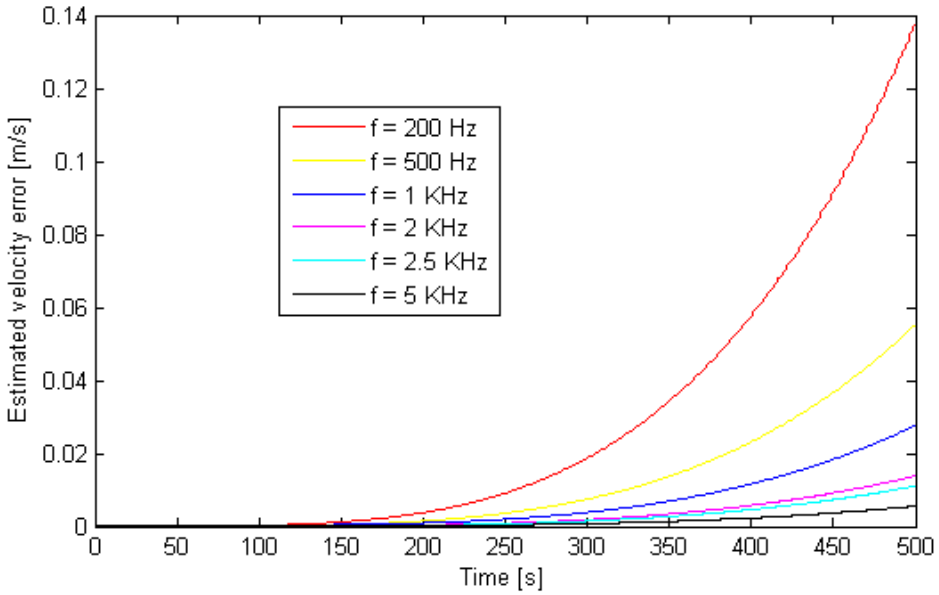

Figure 56: Estimated velocity error as a function of time. Each simulation has a different INS frequency (the reader is referred to Annex B for additional information concerning the simulations).

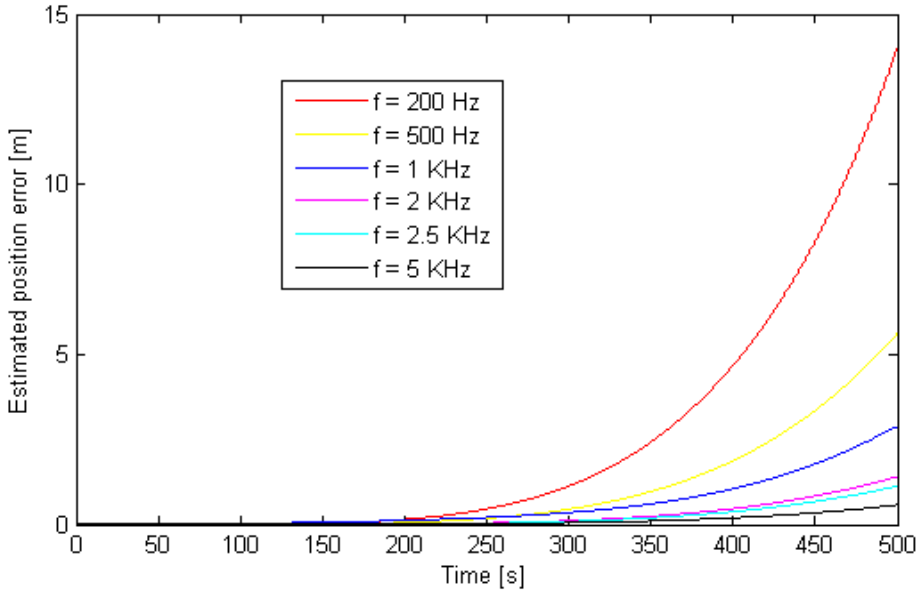

Figure 57: Estimated position error as a function of time. Each simulation has a different INS frequency (the reader is referred to Annex B for additional information concerning the simulations).

As it can be seen in Figure 56 and Figure 57, the INS performance degrades as *f* decreases. This fact correctly reflects the expected performance. Then, the result of the sensitivity to the INS frequency test is positive.

In order to validate the ideal INS performance, the maximum errors have been plotted as a function of INS frequency.

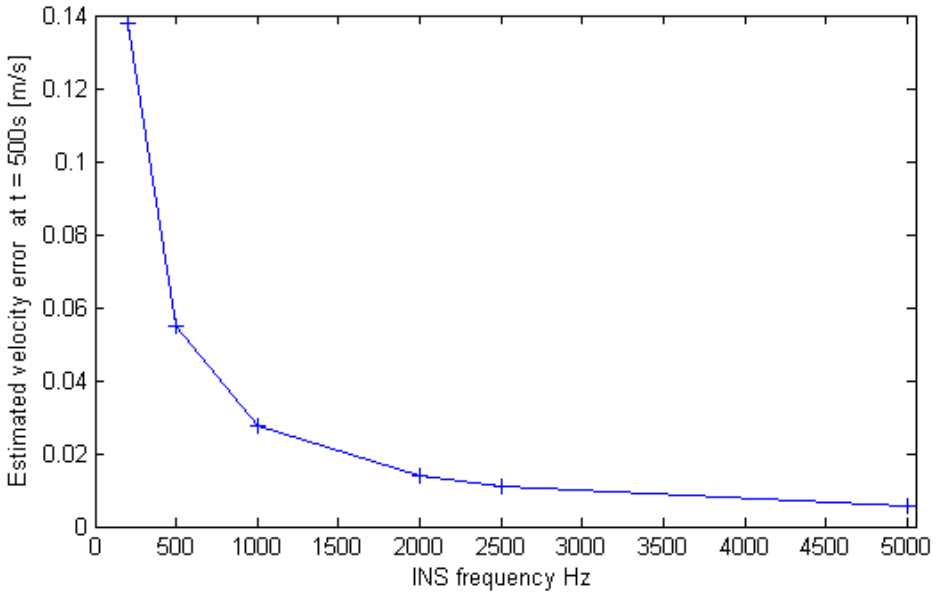

Figure 58: Estimated velocity error at the end of the trajectory as a function of INS frequency.

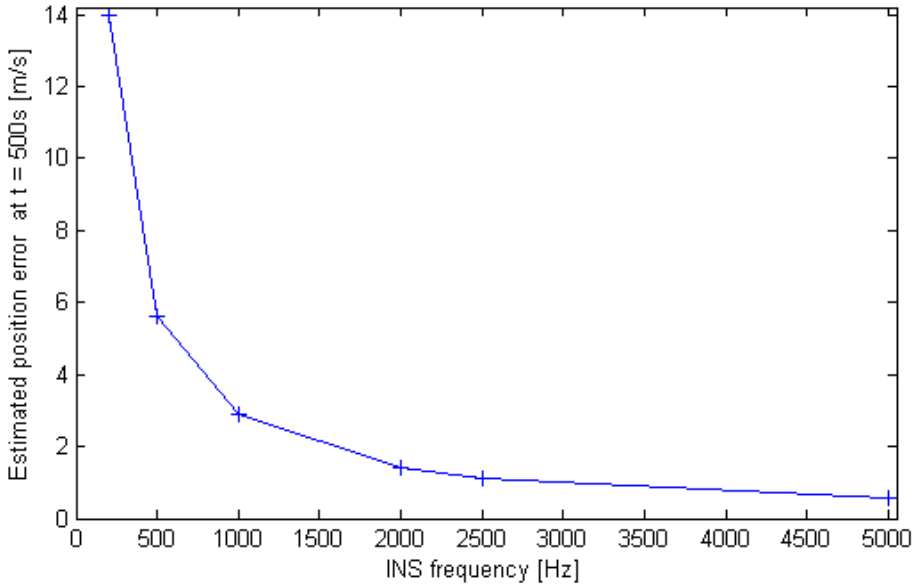

Figure 59: Estimated velocity error at the end of the trajectory as a function of INS frequency.

Figure 58 and Figure 59 show that the INS performance improves as the INS frequency increases. Moreover, the simulation results of both figures have a form that could be expressed by a function of the type:

$$E = a \cdot f^{-b} \quad , \qquad \text{Eq. 66}$$

where *a* and *b* are positive parameters, *E* is the estimated position or velocity error at the end of the trajectory and *f* is the INS frequency. Eq. 66 indicates that in the ideal model (infinite INS frequency), the error would be zero. Therefore, the result of the ideal simulation test is positive.

7.1.2 Sensitivity to attitude functions test

The test on the sensitivity to attitude functions consists in simulations executed with an INS frequency of 200 Hz. The error associated to the INS frequency also depends on the derivative of the defined turn rate function. As a consequence, we have decided to use similar functions. The attitude functions defined in the model are:

$$\boldsymbol{Turn\ rate} = [10^{-2} \cdot \cos\left(\frac{t}{10}\right) \quad 0.8 \quad 10^{-3} \cdot t] \text{ [rad/s].} \qquad \text{Eq. 67}$$

$$\boldsymbol{Turn\ rate} = [0.8 \quad 10^{-2} \cdot \cos\left(\frac{t}{10}\right) \quad 10^{-3} \cdot t] \text{ [rad/s].} \qquad \text{Eq. 68}$$

$$\boldsymbol{Turn\ rate} = [0.8 \quad 10^{-3} \cdot t \quad 10^{-2} \cdot \cos\left(\frac{t}{10}\right)] \text{ [rad/s].} \qquad \text{Eq. 69}$$

$$\boldsymbol{Turn\ rate} = [10^{-2} \cdot \cos\left(\frac{t}{10}\right) \quad 10^{-3} \cdot t \quad 0.8] \text{ [rad/s].} \qquad \text{Eq. 70}$$

$$\boldsymbol{Turn\ rate} = [10^{-3} \cdot t \quad 10^{-2} \cdot \cos\left(\frac{t}{10}\right) \quad 0.8] \text{ [rad/s].} \qquad \text{Eq. 71}$$

$$\boldsymbol{Turn\ rate} = [10^{-3} \cdot t \quad 0.8 \quad 10^{-2} \cdot \cos\left(\frac{t}{10}\right)] \text{ [rad/s].} \qquad \text{Eq. 72}$$

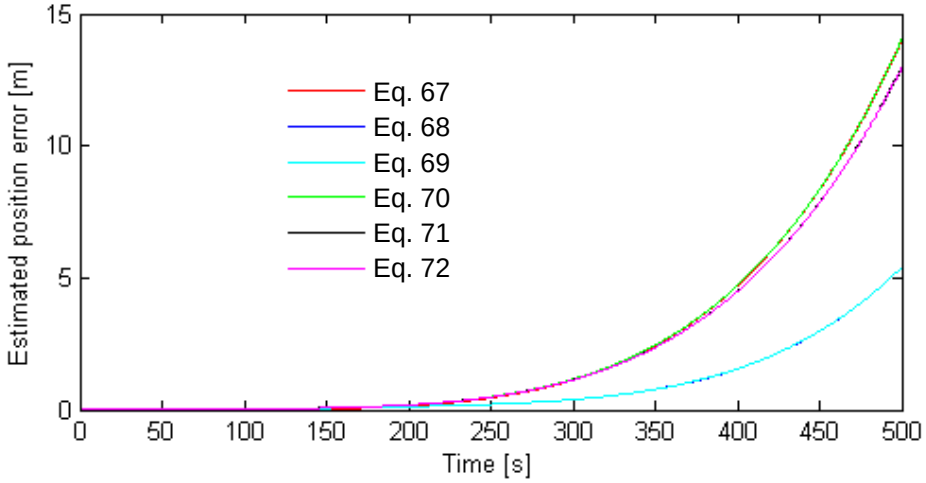

Figure 60: Estimated position error as a function of time. Each simulation uses different turn rate equations (the reader is referred to Annex B for additional information concerning the simulations).

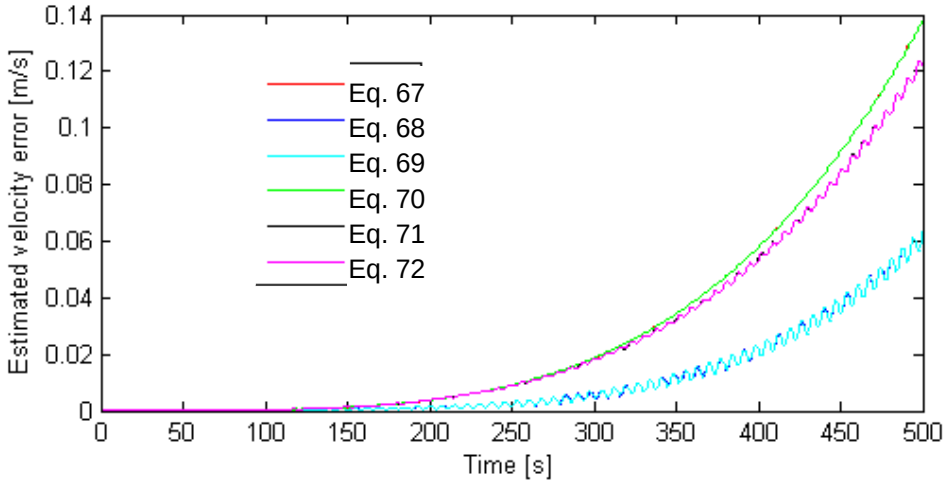

Figure 61: Estimated velocity error as a function of time. Each simulation uses different turn rate equations (the reader is referred to Annex B for additional information concerning the simulations).

Figure 60 and Figure 61 show that the results of the simulations corresponding to Eq. 67 and Eq. 70 are identical. The same fact occurs with the simulation results corresponding to Eq. 68 and Eq. 69 and, Eq. 71 and Eq. 72. The justification is the attitude change at the beginning of the trajectory. As illustratedd in section 4.3.1 , at the beginning of the trajectory the errors increase quadratically with time. As a consequence, the simulations with high turn rates in direction orthogonal to the acceleration vector at the beginning of the trajectory have more error at the end of trajectory. As the results shown in Figure 60 and Figure 61 agree with the previous considerations, the result of the test on sensitivity to attitude functions test is positive.

7.1.3 Sensor calibration errors test

The test on sensor calibration errors is executed by performing two sets of ten simulations with the same sensor. At the beginning of each simulation the random calibration errors have been changed. The maximum calibration scale factor error has been defined as 1% in the first set of simulations and as 10 ppm in the second set. The other properties are considered ideal. The trajectory and the attitude are defined in the simulations with Eq. 64 and Eq. 65.

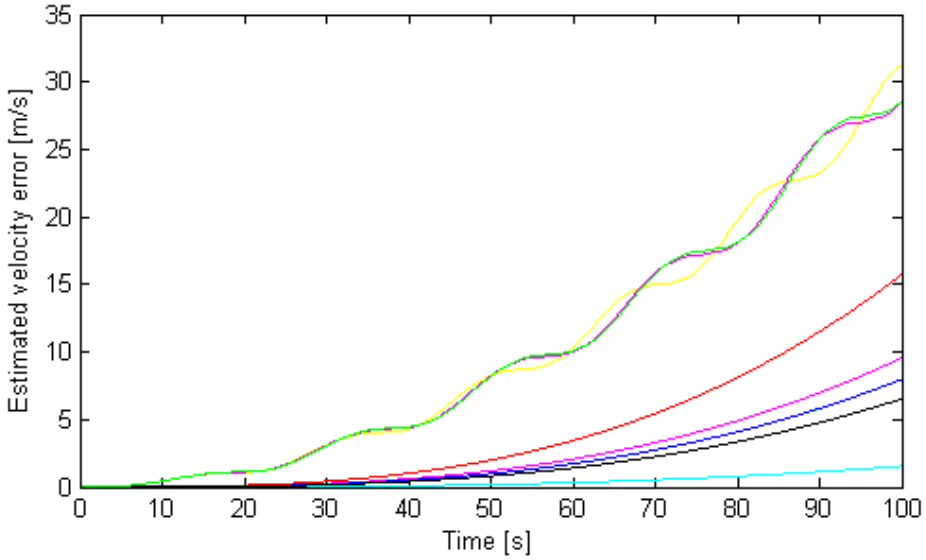

Figure 62: Estimated velocity error as a function of time. The maximum calibration scale factor error has been set to 1% (the reader is referred to Annex B for additional information concerning the simulations).

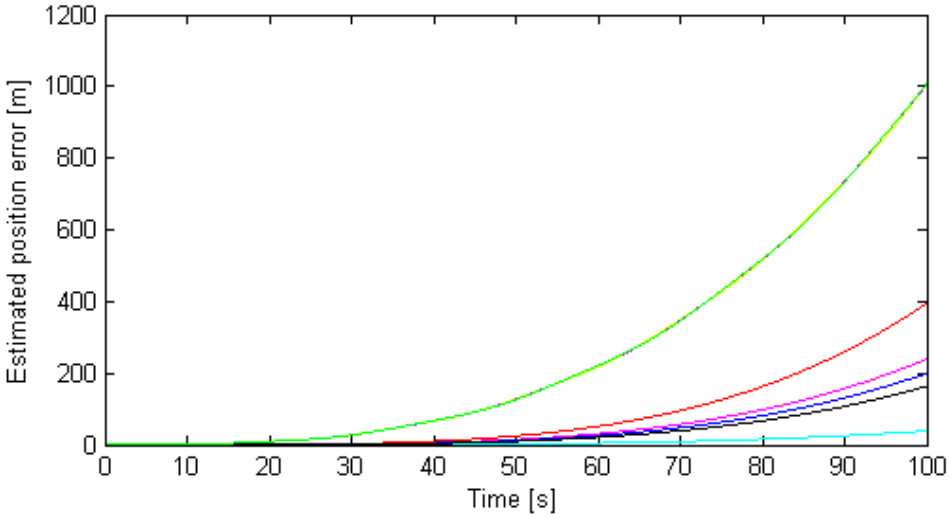

Figure 63: Estimated position error as a function of time. The maximum calibration scale factor error has been set to 1% (the reader is referred to Annex B for additional information concerning the simulations).

The maximum estimated position error (Figure 63) is approximately 1000 m and the maximum estimated velocity error (Figure 62) is approximately 31 m/s.

Figure 64 and Figure 65 show the results of the second simulation set. The maximum scale factor error is smaller in this set than in the previous one. This fact is reflected in the figures: Figure 64 and Figure 65 show an INS performance significantly better than Figure 63 and Figure 62. The largest estimated velocity and position errors are approximately are 0.25 m and 0.01 m/s, respectively.

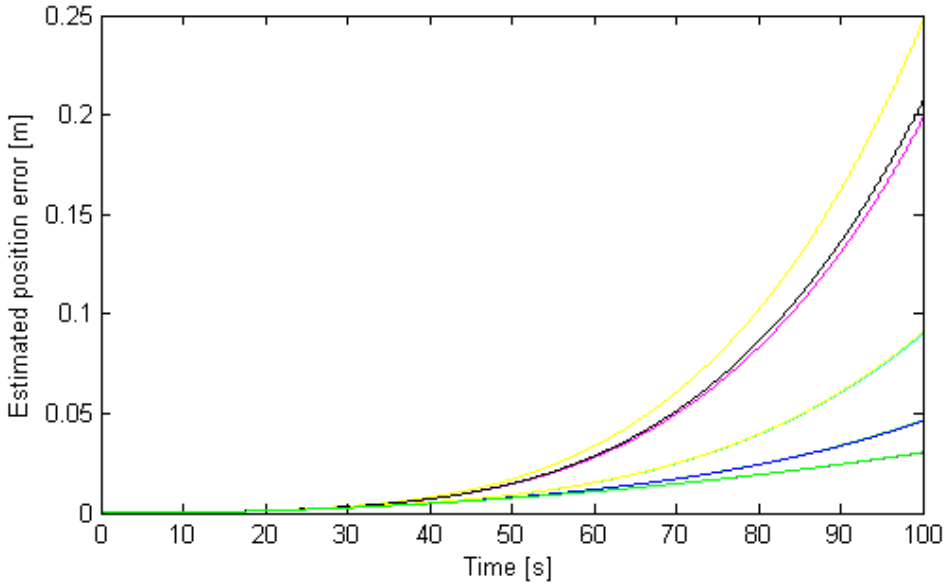

Figure 64: Estimated position error as a function of time. The maximum calibration scale factor error has been set at 10 ppm (the reader is referred to Annex B for additional information concerning the simulations).

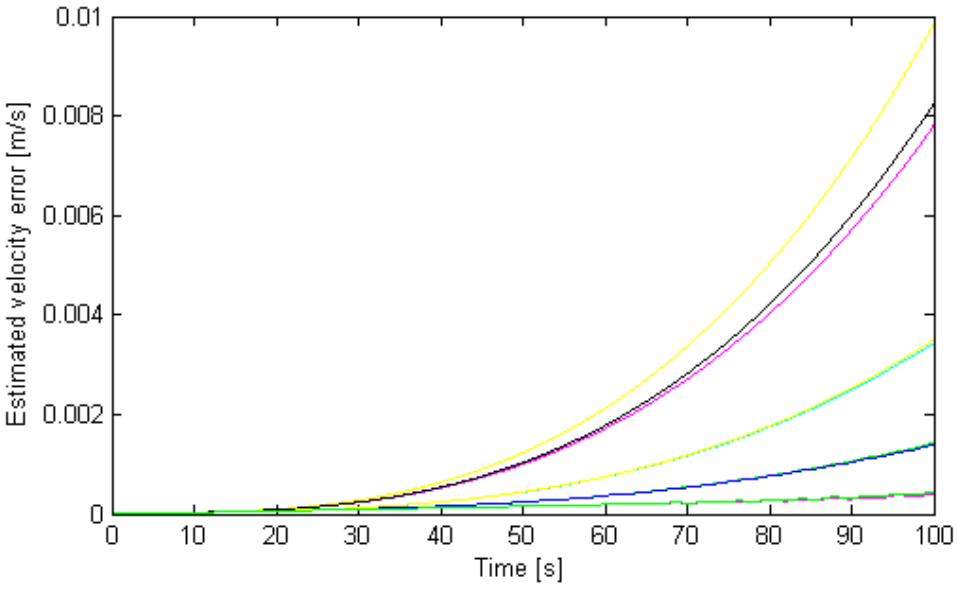

Figure 65: Estimated velocity error as a function of time. The maximum calibration scale factor error has been set at 10 ppm (the reader is referred to Annex B for additional information concerning the simulations).

The error increase in the estimated position and velocity is not proportional to the increase in the maximum scale factor error. This is consequence of the impact of an attitude error on the following trajectory estimations. This fact is described in section 4.3.1 . Therefore, the result of the sensor calibration errors test is positive.

7.1.4 Sensor temperature errors test

The sensor temperature error test consists in the definition of a temperature dependency in the sensor performance and in executing four simulations with different levels for the maximum temperature sensor error. The gyroscope characteristic that is going to be defined as a function of temperature is the scale factor. The scale factor function introduced in the model is the function that corresponds to the ISA of the Ariane V. The temperature dependence of the gyroscopes is not specified in the ISA datasheet. However, the maximum error induced by the temperature is among the available data [22]. The information is available in temperature intervals. In order to represent this data in Figure 66, we have assumed that the maximum interval error was in the boundary of the interval. The boundary selected is the farthest from the zero error temperature (24ºC approximately).

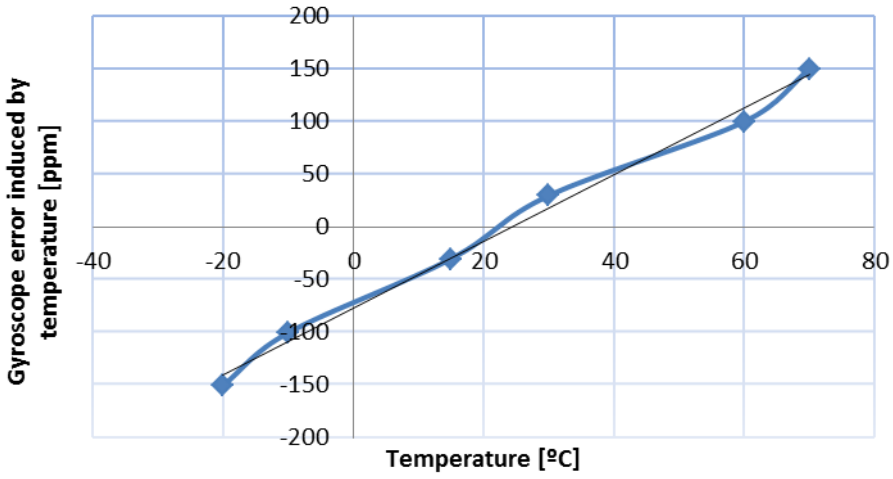

Figure 66: Temperature error as a function of temperature. In the ISA datasheet all the errors were defined as being positive. The choice of setting a positive or negative derivative does not affect the test results.

The linear regression fits sufficiently well to the real values. Its equation is:

$$E = 3.1643T - 76.469 \quad , \qquad \text{Eq. 73}$$

where E is the gyroscope error induced by temperature [ppm] and T is the ISA temperature. As a consequence, the scale factor is defined as a function of temperature. The four maximum temperature error defined values are: 0 1, 5 and 10 ºC. Figure 68 shows that the simulation with 1 ºC of maximum temperature error has better velocity results than the ideal simulation. This fact is consequence of the INS frequency and temperature induced errors cancelation.

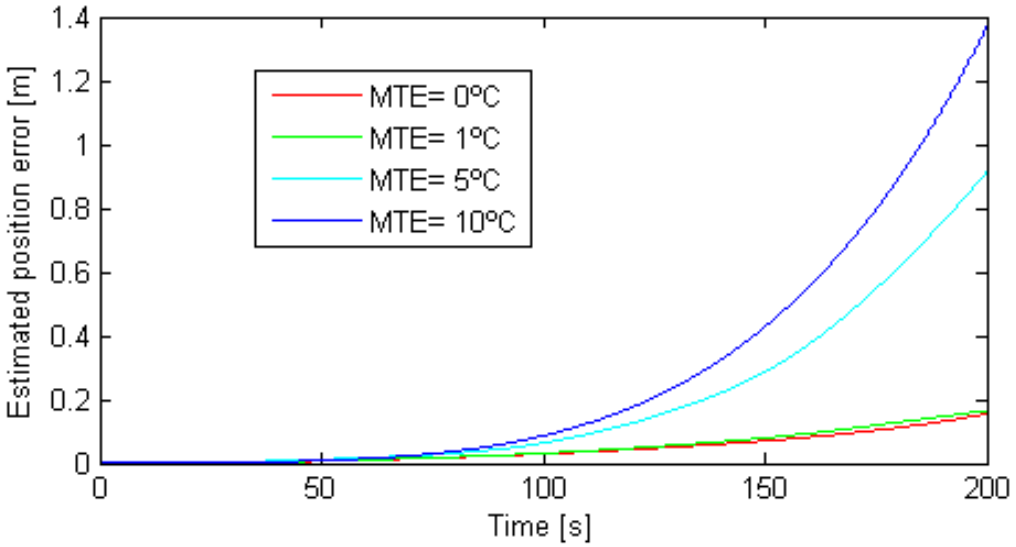

Figure 67: Estimated position error as a function of time and of maximum temperature error (MTE). The reader is referred to Annex B for additional information concerning the simulations.

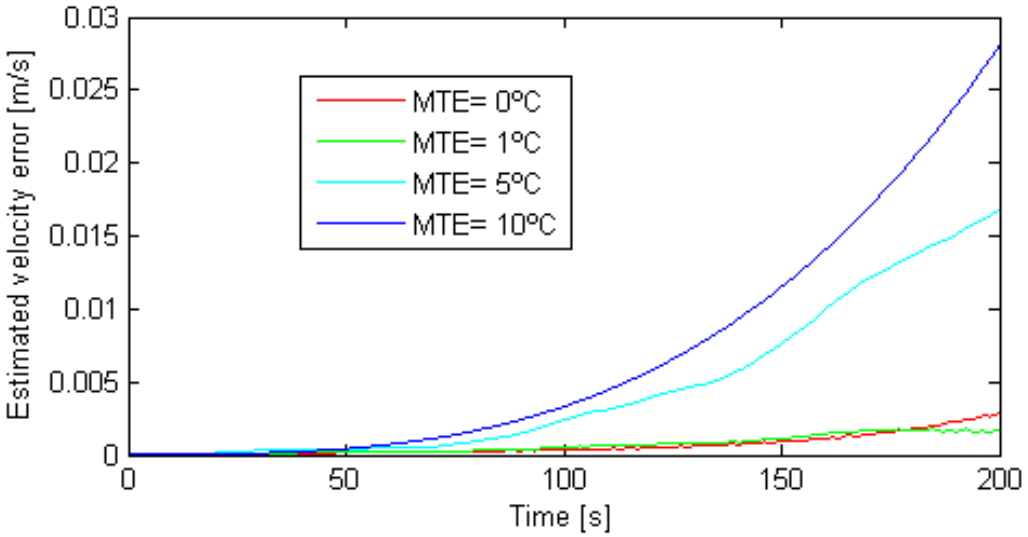

Figure 68: Estimated velocity error as a function of time and of maximum temperature error (MTE). The reader is referred to Annex B for additional information concerning the simulations.

The simulation results shown in Figure 67 and Figure 68 are as expected: the INS performance degrades when the maximum temperature error increases and the estimated velocity error increases with time more randomly than in previous simulations. As a consequence, the result of the sensor temperature error test is positive.

7.1.5 Sensor random walk test

The sensor random walk error test is performed with a set of simulations where the parameter of the random walk error has been set at 30 ppm. All the simulations have exactly the same inputs.

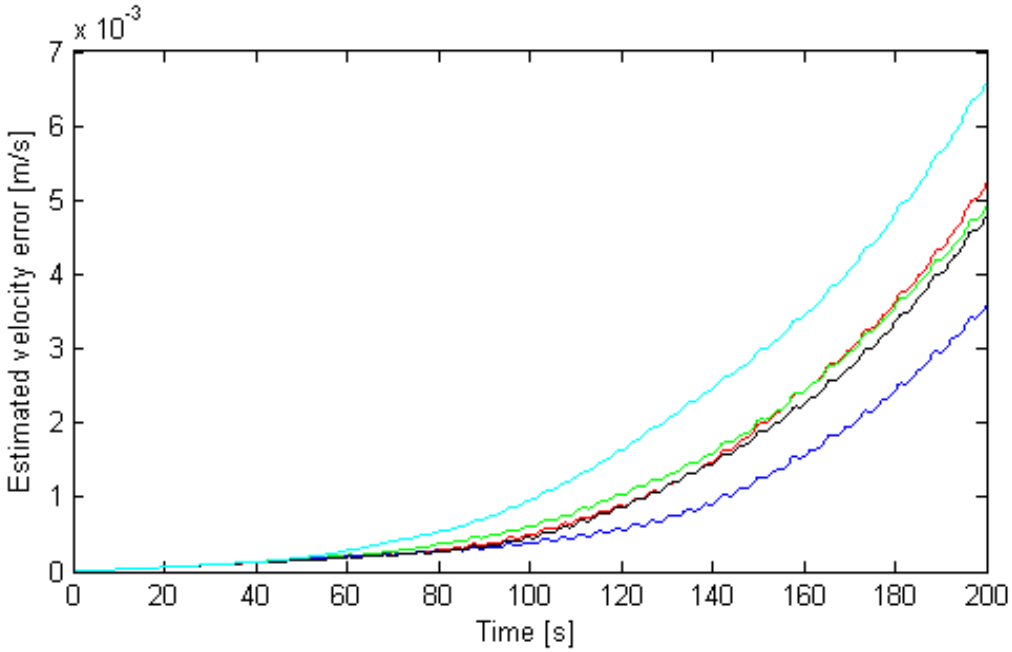

Figure 69: Estimated velocity error as a function of time. The random walk error has been defined as 10 ppm (the reader is referred to Annex B for additional information concerning the simulations).

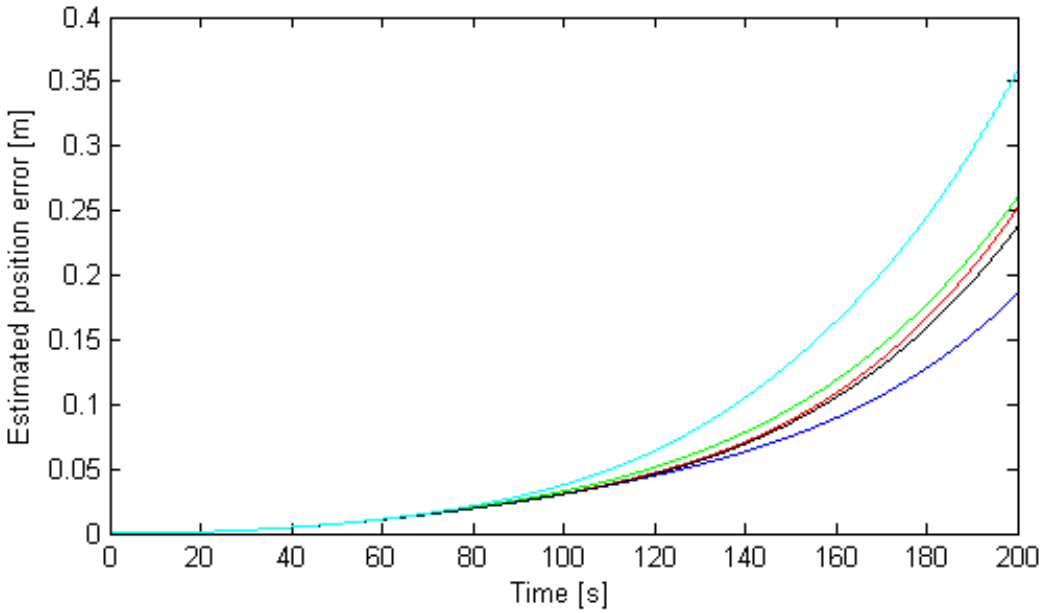

Figure 70: Estimated velocity error as a function of time. The random walk error has been defined as 10 ppm (the reader is referred to Annex B for additional information concerning the simulations).

Figure 69 and Figure 70 show how the random error affects the simulation results. The velocity error has a random component and, due to the error propagation in time, the estimated velocity value error difference between different simulations increases. Therefore, the result of the sensor random walk test is positive.

As a result of obtaining positive results to all the attitude tests, we can affirm that the INS model has been validated concerning the attitude.

7.2 Trajectory validation

The trajectory validation consists in comparing real flight data and the results of the simulation. The real flight data has been provided by GTD[31].

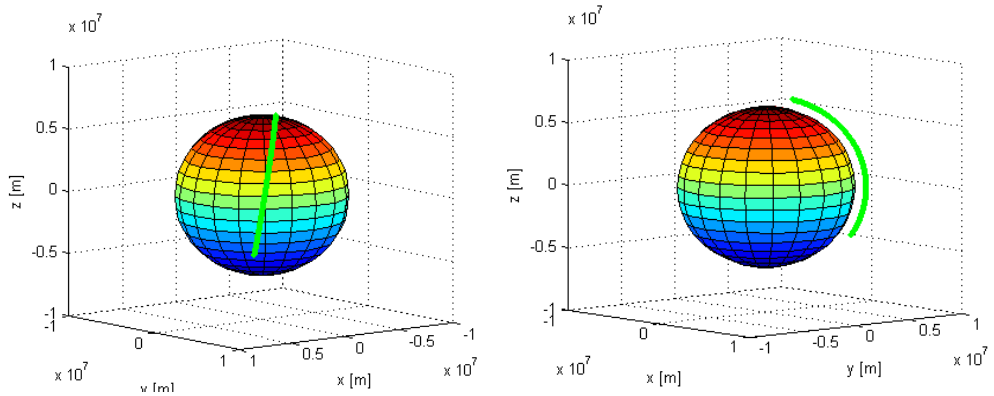

Figure 71: Two views of the real flight data provided by GTD [31]. The sphere is the Earth.

Figure 71 shows the trajectory used to validate the model concerning the INS trajectory. The trajectory is a high inclination orbit (i≈79º) with low eccentricity. The available data is the estimated position and velocity with a 10 Hz frequency. The velocity data frequency has been increased by interpolation with a cubic spline. Then, the position and acceleration have been computed by integrating and differentiating the obtained velocity. It has been checked that the computed position with spline is equal to the real flight estimated position. Figure 72 and Figure 73 show the interpolated and real flight data of the velocity and position components.

Sensor temperature errors test is not performed for the accelerometers because gyroscope and accelerometer temperature operations in the model are exactly the same.

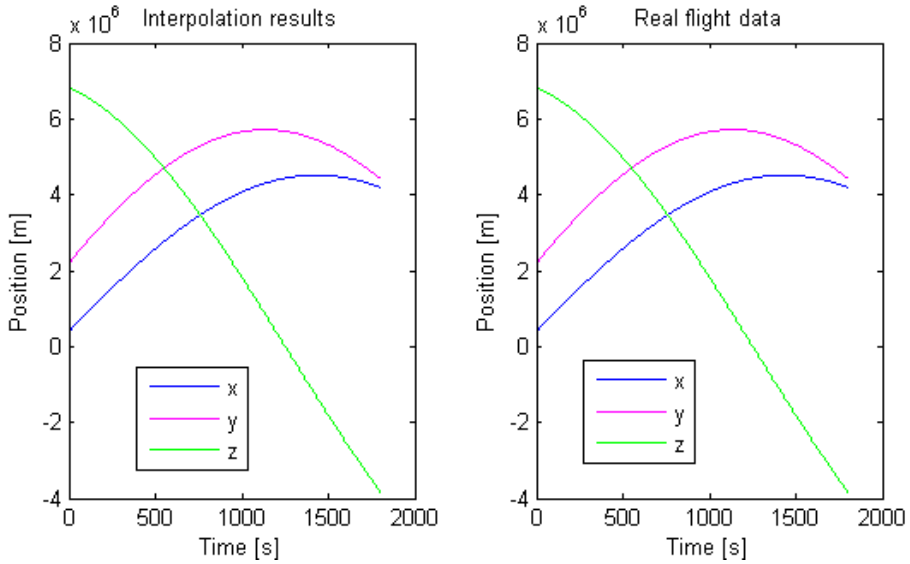

Figure 72: Position as a function of time. The two sets of results correspond to the velocity interpolation (left) and real flight data (right).

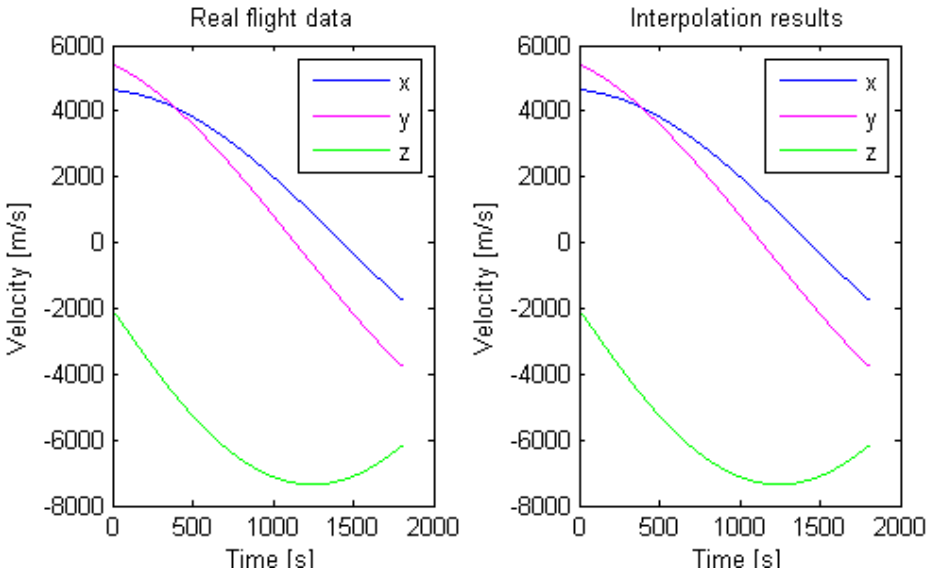

Figure 73: Velocity as a function of time. The two sets of results correspond to the velocity interpolation (right) and real flight data (left).

7.2.1 Ideal simulation test

The inertial sensors performance has been considered ideal. Nonetheless, the simulation is affected by the error associated to the gravity model used in the INS algorithm and to the INS acquisition frequency (200 Hz). It must be underlined that the gravity model used was evaluated by taking into account the INS-GNSS hybridization. As a consequence of the gravity error and the time interval evaluated, the error may be considerably bigger than in the attitude validation.

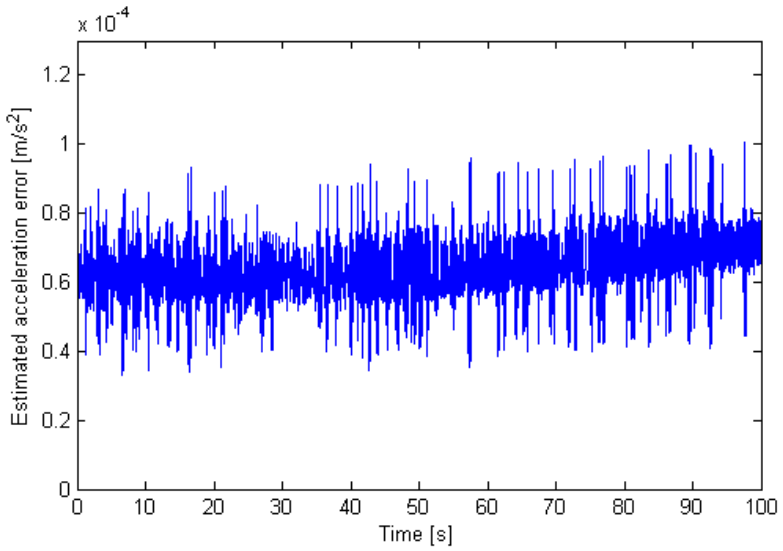

Figure 74: Estimated acceleration as a function of time. The figure is focused on the first 100 trajectory seconds into the flight in order to show the deviation and the random error components.

The results shown in Figure 74 can be divided into two components: a deviation and a random estimated acceleration error. The deviation is produced by the gravity model adopted in the INS algorithm. The random deviations are caused by the INS algorithm and by the resulting small delay. The small delay produces a random error because the acceleration introduced in the model also has a random component. This random component can be seen in Figure 75.

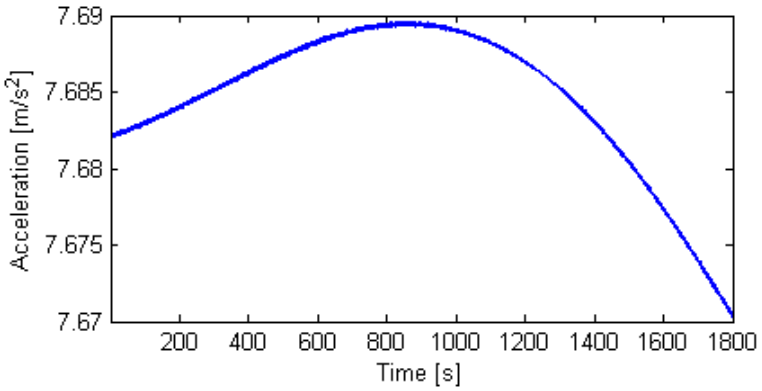

Figure 75: Acceleration defined in the model as a function of time.

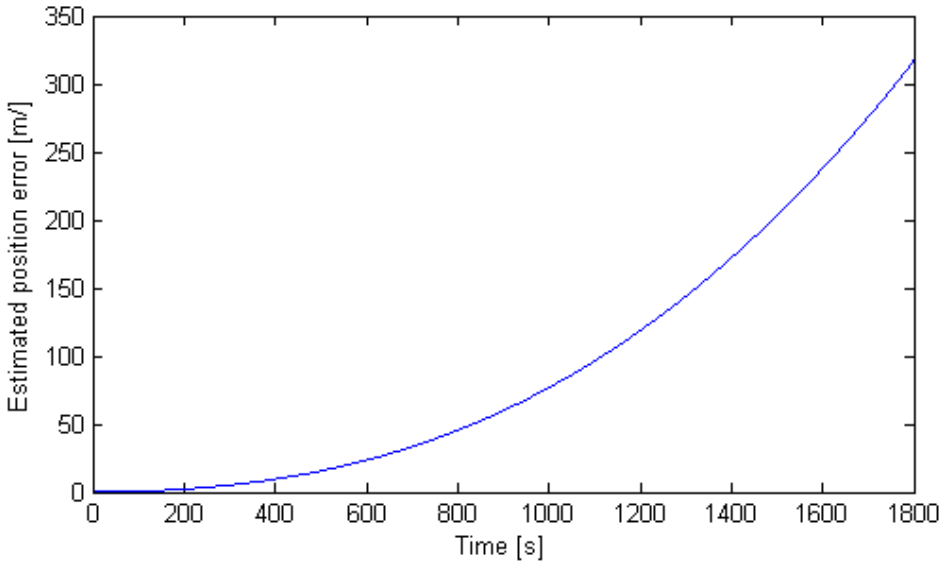

Figure 76: Estimated position error as a function of time. The results correspond to the simulation with ideal ISA.

If the initial acceleration error is integrated twice over time, the result is the estimated position error, which is 113.4 m at the end of the trajectory. This is not the value that appears in Figure 76 because the vertical channel instability must be taken into account. As a consequence of the gravity error over time, Eq. 63 from section 6.3 cannot be applied and the estimated position error cannot be computed analytically. Therefore, the ideal simulation test result has been considered positive.

7.2.2 Sensor random walk error test

In order to test the definition of the sensor random walk error, some simulations have been executed with different values assigned to the maximum random walk error: $3 \cdot 10^{-3}$ m/s^2, $3 \cdot 10^{-4}$ m/s^2 and an ideal ISA.

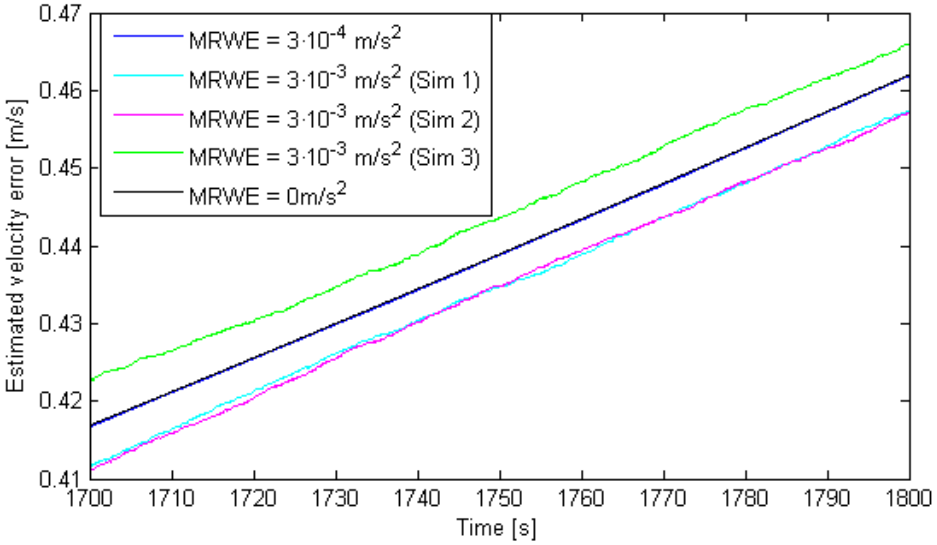

Figure 77: Estimated velocity error as a function of time. The results correspond to the last 200 seconds of the trajectory. MRWE is the maximum random walk error.

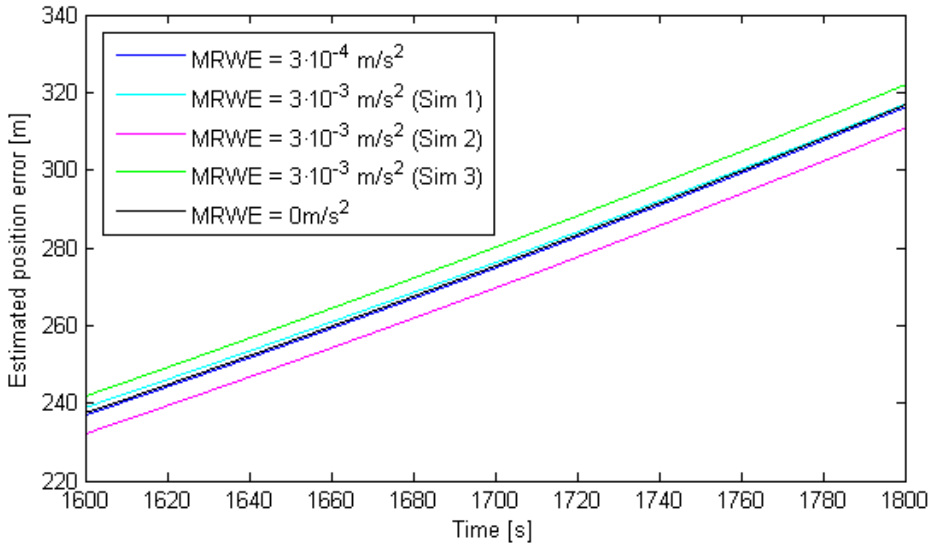

Figure 78: Estimated position error as a function of time. The results correspond to the last 200 seconds of the trajectory. MRWE is the maximum random walk error.

Figure 77 and Figure 78 focus on the last 200 seconds of the trajectory because the effect of random walk errors in the simulations is much smaller than the gravity approximation error. As it can be seen in Figure 77 and Figure 78, the sensor random walk error does not affect significantly the INS performance when it is set to $3 \cdot 10^{-4}$ m/s^2. However, when it is set to $3 \cdot 10^{-3}$ m/s^2 the deviations became important. Furthermore, it can be appreciated that the same simulations parameters lead to different simulation results. Therefore, the result of the test is positive, because the simulation results are the expected ones.

7.2.3 Sensor calibration errors test

The test on sensor calibration error test has been carried out by considering only the scale factor calibration error. In section 7.1 this decision has been argued for gyroscopes; the same consideration is valid for accelerometers. In this test all the simulations are executed with the same inputs. The maximum scale factor calibration error has been set to 0.3%, which is ten times bigger than in the ISA onboard Ariane V. In Figure 79 and Figure 80 the results corresponding to the ideal ISA simulation has been added in order to set a reference for the other results shown.

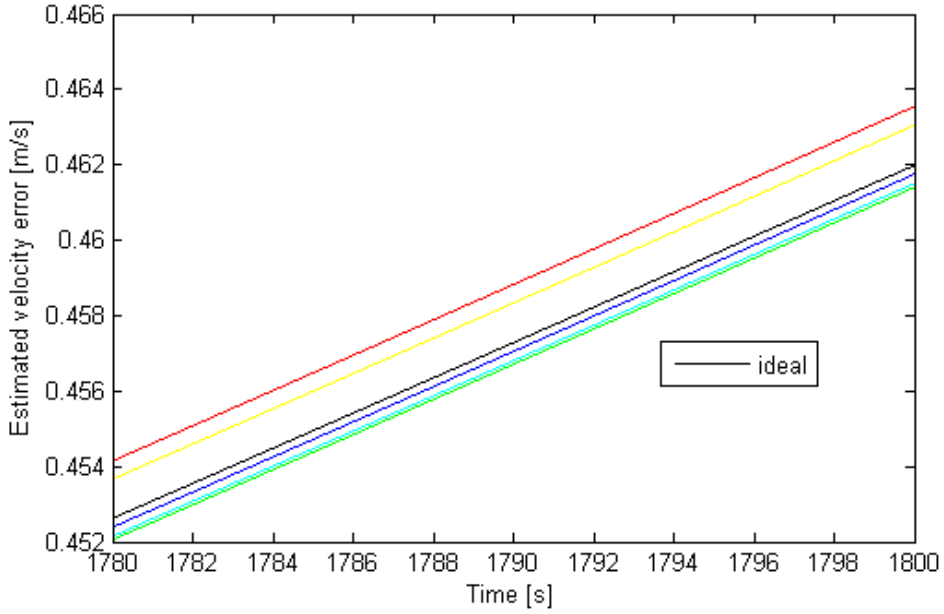

Figure 79: Estimated velocity error as a function of time. The results correspond to the last 20 seconds of the trajectory, and the simulations have been executed with a maximum scale factor error of 0.3%. The black curve corresponds to a simulation executed using an ideal ISA model.

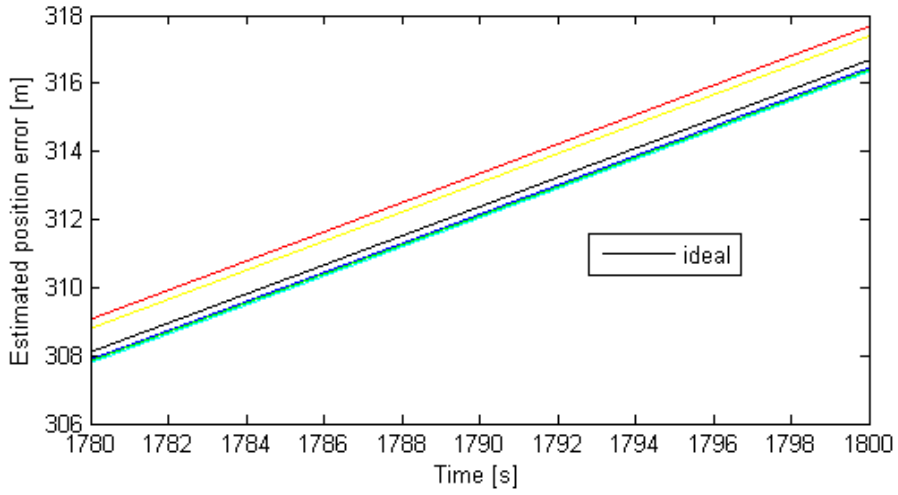

Figure 80: Estimated position error as a function of time. The results correspond to the last 20 seconds of the trajectory, and the simulations have been executed with a maximum scale factor error of 0.3%. The black curve corresponds to a simulation executed using an ideal ISA model.

Figure 79 and Figure 80 show how the scale factor calibration error modifies the estimated data. Moreover, in these figures it can be seen how, with the same model inputs, five simulations lead to five different results. Taking into account that Figure 79 and Figure 80 show the expected simulation results, it can be concluded that the result of the sensor calibration errors test is positive.

All the validation test results are positive. Then, we can conclude that the INS trajectory has been validated.

7.3 INS-GNSS hybridization validation

The validation of the hybridization cannot be carried out with experimental data as previously done with the trajectory validation. One reason is that there is no available information of any hybrid navigation system for launchers. Moreover, if such information was published, it should use the same type of hybridization. Another reason, as important as the first one, is that the GNSS model is inaccurate and incomplete. An accurate modelling of the GNSS performance is not in the scope of this project.

Therefore, the simulations illustrated in section 6.5 can be used as a validation data. The simulation results reflect the expected INS-GNSS hybridization performance. As a consequence, it has been decided that the hybridization validation result is positive.

8 Sensitivity analyses

The aim of this section is to quantify the effects of modifying precision of the initial conditions, the ISA accuracy and the navigation algorithm on the trajectory and velocity estimations.

One parameter at a time is modified. By default, the initial conditions error is zero, the ISA parameters are those listed in Table 10 and the navigation algorithm is as described in previous chapters. The INS, GNSS and temperature acquisition frequencies are 200, 1 and 0.5 Hz, respectively. The values of Table 10 have been taken from the utilisation manual of the Quasar 3000 [22] ISA. The temperature dependency is obtained by the same procedure detailed in section 7.1.4 . The maximum temperature error is set to 1.5 ºC.

GYROSCOPE		
Bias:	0.0112	[º/h]
Temperature coefficient:	0.0032	[º/h/ºC]
Bias error:	$4.5 \cdot 10^{-2}$	[º/h]
Scale factor error:	13.187	[ppm]
Temperature coefficient:	3.164	[ppm/ºC]
Maximum random walk error:	2.616	[º/h]
ACCELEROMETER		
Bias:	350	[µg]
Temperature coefficient:	0	[µg/ºC]
Bias error:	173	[µg]
Scale factor error:	291	[ppm]
Temperature coefficient:	0	[ppm/ºC]

Table 10: ISA parameters introduced in the model. They have been obtained from the Quasar 3000 utilization manual (not all pages are available) [22]. Parameters that are not available in the manual have been set to zero. There are no differences between inertial sensors of different axes.

8.1 Precision of the initial values

This sensitivity analysis is carried out in order to determine the performance degradation that causes the increase in the error in the definition of the initial position, velocity and attitude. The results of this section are important because they must be taken into account in the definition of the data transfer between the fighter and the host vehicle. Eventually, these results can impose a change in the currently defined release manoeuvre into a steadier manoeuvre.

8.1.1 Initial velocity error

Four simulations have been executed in order to determine how the initial velocity error affects the INS performance. The model inputs are all the same except for the initial velocity error.

Initial velocity error [m/s]	Maximum estimated position error [m]	Maximum estimated velocity error [m/s]
0	0.5	0.6
0.5	23.5	1.2
1	52	2
1.5	78	2.7
2	105	2.9

Table 11: Maximum estimated position and velocity errors as a function of the initial velocity error (consult Annex B for further information concerning the simulations).

Table 11 details the maximum estimated position and velocity errors as a function of the initial velocity error. The maxima are placed just before the first position correction in the case of the position error and before the first velocity correction in case of the velocity error. The estimated position and velocity results are exactly the same for all simulations twenty seconds after the first velocity correction. Therefore, initial velocity errors do not degrade the INS performance at the end of the trajectory.

8.1.2 Initial attitude error

The initial attitude error affects the INS performance during the entire trajectory. The last seconds of the trajectory are not taken into account in the analysis due to the trajectory definition problem explained in section 6.4 .

Initial attitude error [rad]	**Maximum estimated position error [m]**		
	Before position corrections	Before velocity corrections	From 390s to 3345 s.
0	0.52	1.21	$10 \cdot 10^{-4}$
0.005	69.74	84.4	$63 \cdot 10^{-4}$
0.01	139.8	168.3	$12 \cdot 10^{-3}$
0.05	684	830.6	$6 \cdot 10^{-2}$
0.1	1442	1717	0.12

Table 12: Maximum estimated position error as a function of the initial attitude error. It has been found interesting to divide the trajectory into three segments because the INS presents different performances (consult Annex B for further information concerning the simulations)

Initial attitude error [º]	Maximum estimated velocity error [m/s]	
	Before velocity corrections	From 390 to 3345 s.
0	0.6	$4.8 \cdot 10^{-3}$
0.005	42.1	$5.7 \cdot 10^{-3}$
0.01	84.3	$9.5 \cdot 10^{-3}$
0.05	415.4	$4.6 \cdot 10^{-2}$
0.1	858.7	$9.2 \cdot 10^{-2}$

Table 13: Maximum estimated velocity error as a function of the initial attitude error. It has been found interesting to divide the trajectory into two segments because the INS presents different performances (consult Annex B for further information concerning the simulations)

Table 12 and Table 13 detail the INS performance as a function of the initial attitude error. The results present large differences among trajectory segments. The error increases rapidly in parts of the trajectory where high acceleration accurs. When the velocity is corrected with GNSS data, the estimated velocity and position errors decrease rapidly down to error values that can be neglected in comparison with the previous errors. As a consequence, it could be profitable to anticipate the first velocity correction. Nonetheless, the optimization of the first velocity correction time must be done with a more precise value of the maximum attitude error and with the real Aldebaran nominal trajectory. Therefore, the analysis of the optimum time to start correcting the velocity with GNSS data should be executed in a more advanced project phase.

8.1.3 Initial position error

The effect of the initial position error does not disappear at the first position update. The reason is the gravity estimation with the estimated position. The gravity estimation error leads to velocity error, which is rapidly reduced when the velocity update starts.

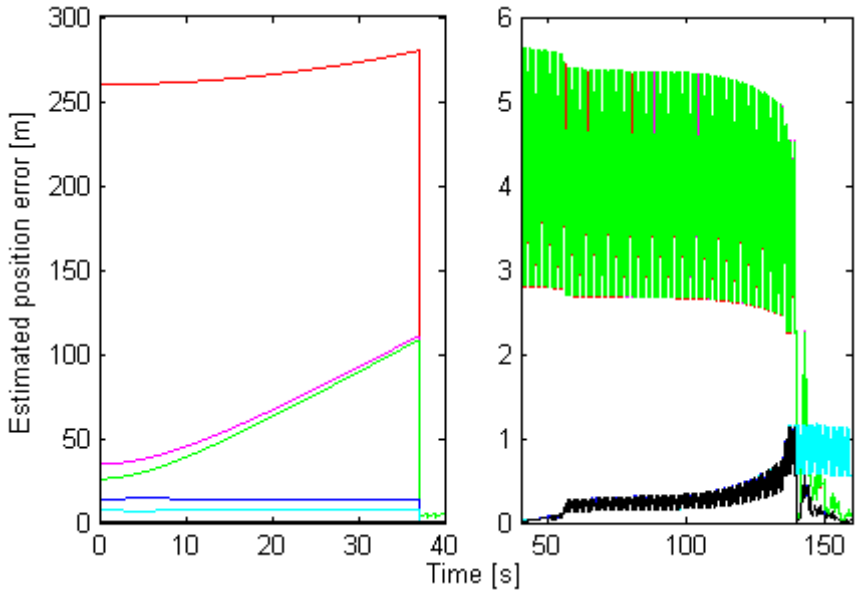

Figure 81: Estimated position error as a function of time. The two plots are focused on the first seconds of the trajectory because it is where the different simulations lead to different results. The defined initial position error is the estimated position value at t=0s (consult Annex B for further information concerning the simulations).

As it can be seen in Figure 81, the estimated initial position errors can have severe consequences on the INS performance. However, the GNSS position update reduces significantly the error and the velocity update reduces it to values similar to the estimated position error without initialization errors.

8.2 Sensor random walk error

In this section the errors due to accelerometers and gyroscopes random walks are going to be analysed separately. Since the simulation executed with the same random walk error leads to different results, it has been decided to execute the same simulation twice. All the sensitivity analyses referring to the sensor performance have been executed by considering only performance degradations of the properties defined by default. This decision was taken because the aim of the INS-GNSS hybridization is, in part, to reduce the INS weight. Lighter sensors commonly have worse performance than heavy sensors.

8.2.1 Accelerometers random walk error

The consequences of random walk errors on position can be seen in Figure 82 and Figure 83. Figure 84 and Figure 85 show the velocity error of the simulations carried out. Figure 82 and Figure 84 focus on the beginning of the trajectory, while the other two figures focus on a time period of the intermediate orbit. On the intermediate orbit the error introduced in the estimated velocity and position can be clearly distinguished.

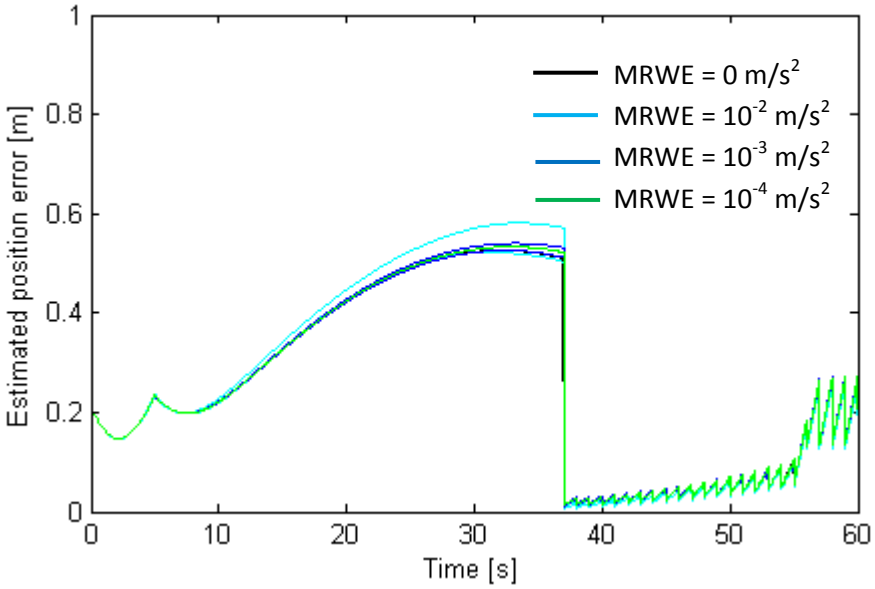

Figure 82: Estimated position error as a function of time. Two simulations have been executed with the same maximum random walk error, MRWE. Consult Annex B for further information concerning the simulations.

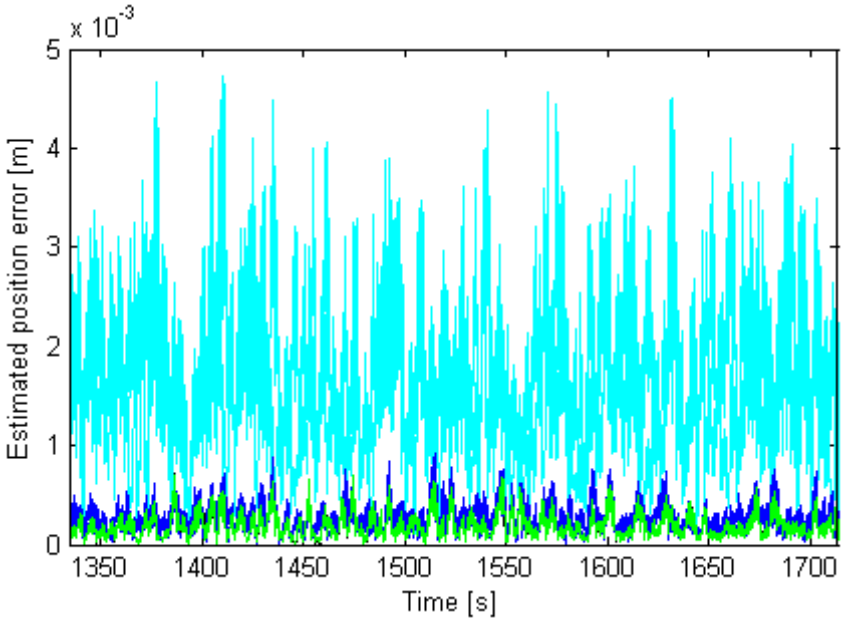

Figure 83: Estimated position error as a function of time. The results shown in this figure are the same than the ones shown in Figure 82. In this case the figure is refers to the intermediate orbit trajectory segment.

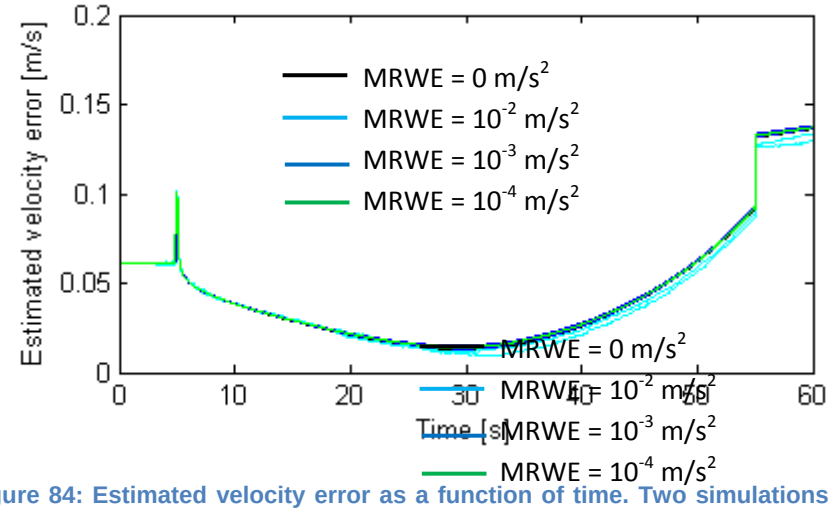

Figure 84: Estimated velocity error as a function of time. Two simulations have been executed with the same maximum random walk error, MRWE. Consult Annex B for further information concerning the simulations.

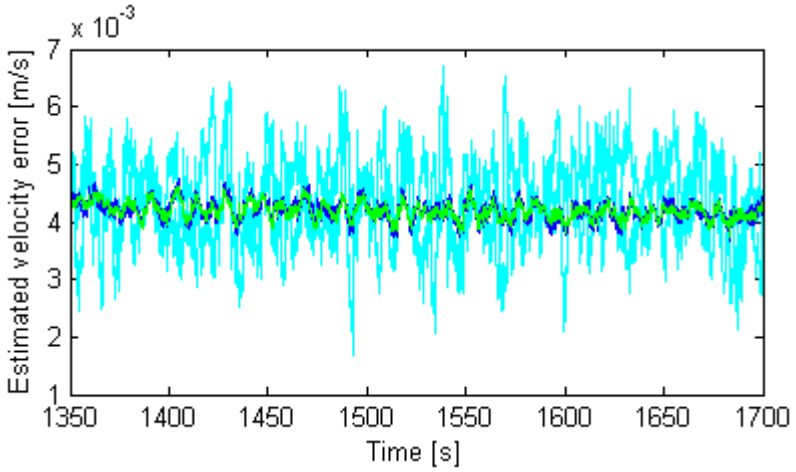

Figure 85: Estimated velocity error as a function of time. The results shown in this figure are the same than the ones shown in Figure 84. In this case the figure refers to the intermediate orbit trajectory segment.

Figure 82, Figure 83, Figure 84 and Figure 85 show that random walk errors values of 10^{-3} m/s^2 or 10^{-4} m/s^2 do not affect the INS performance significantly. Nonetheless, the 10^{-2} m/s^2 random walk error leads to considerable random deviations after the position and velocity corrections and to a performance deviation before velocity corrections.

8.2.2 Gyroscopes random walk error

INS sensitivity to gyroscope random walk error is analysed with a set of simulations that consists of three pairs of simulations and the simulation done with the default sensor specification. Each pair of simulations has a different value of the maximum random walk error. Figure 86 and Figure 87 show the results of the simulations executed.

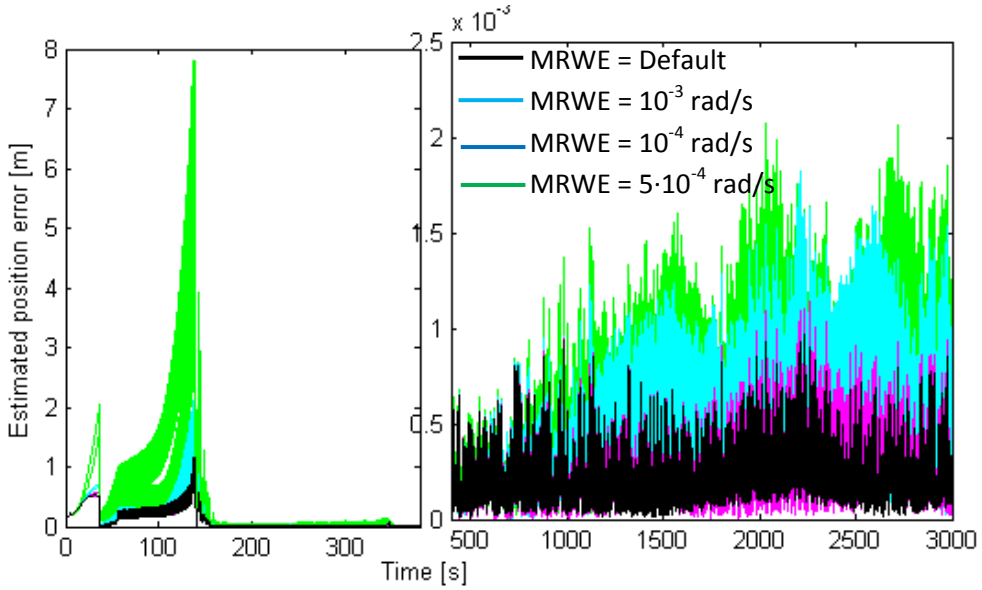

Figure 86: Estimated position error as a function of time and of the gyroscope maximum random walk error (consult Annex B for further information concerning the simulations). The figure has been divided in two parts in order to allow the results before and after the velocity update.

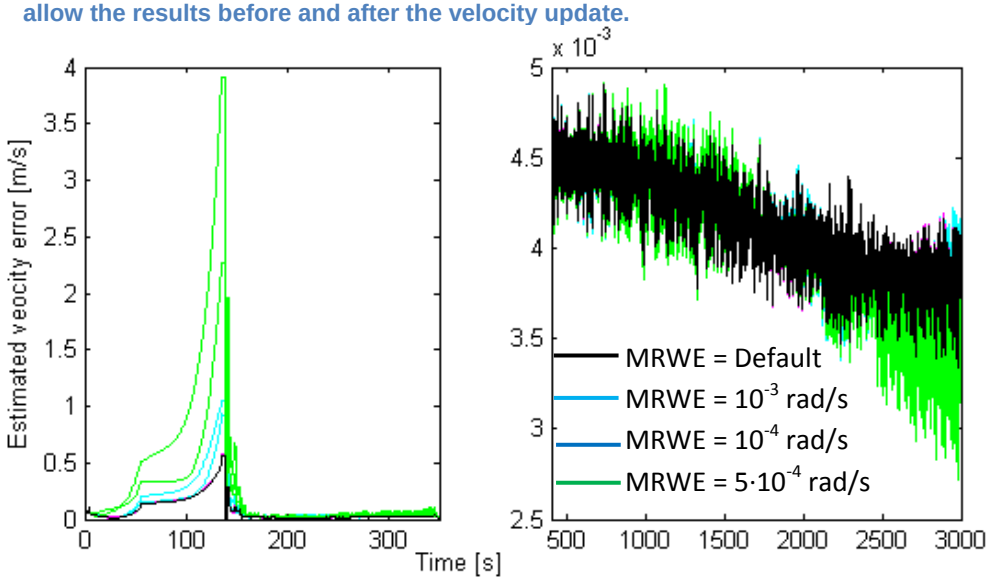

Figure 87: Estimated velocity error as a function of time and of the gyroscope maximum random walk error (consult Annex B for further information concerning the simulations). The figure has been divided in two parts in order to allow the results before and after the velocity update.

As has been remarked before, the same sensor can have different outputs with the same input. This fact is due to the random error. In Figure 86 and Figure 87 this effect can be seen in the same colour curves (same ISA), which are different. The difference between the same ISA curves is bigger in the cases that the maximum random walk error is bigger.

The gyroscope random walk error affects more the INS accuracy on the first 200 seconds of the trajectory than the accelerometer random walk error. However, on

the intermediate trajectory segment, the accelerometer random walk degrades more the INS accuracy than the gyroscope error.

8.3 Sensor bias error

The sensitivity of the INS to bias error is analysed by performing two simulations and comparing them with a simulation executed with the 'default' values.

8.3.1 Accelerometers bias error

The accelerometer bias errors affect the INS performance considerably before the first velocity first correction because the bias error adds an extra acceleration and it increases continuously the estimated velocity error.

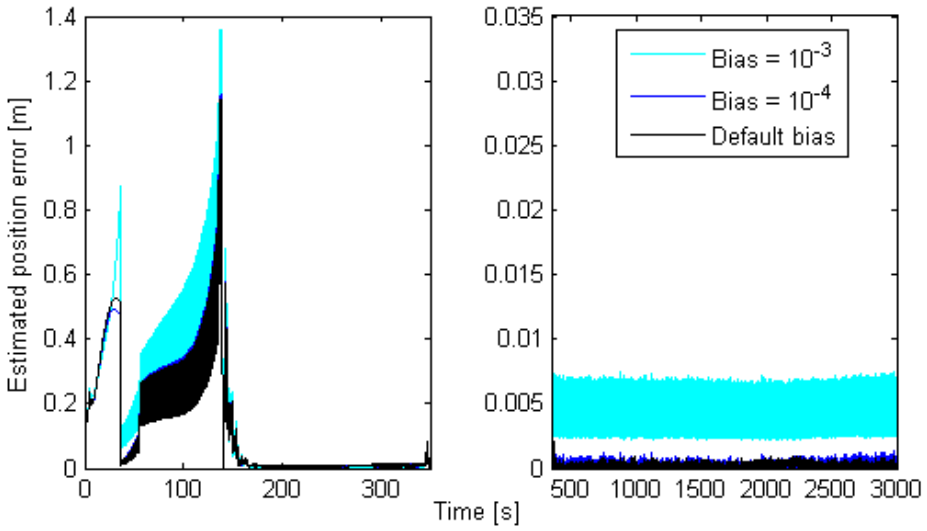

Figure 88: Estimated position error as a function of time and of the accelerometer bias error (consult Annex B for further information concerning the simulations). The figure has been divided in two parts in order to show the results before and after the velocity update. The bias error values detailed in the legend are expressed in m/s^2.

Figure 88 and Figure 89 show the results of three simulations carried out with thee ISAs that have different bias errors. The performance of the INS with 10^{-4} m/s^2 bias is barely affected compared to the default simulation. In contrast, the 10^{-3} m/s^2 bias simulation results are significantly worse than those from the other two simulations.

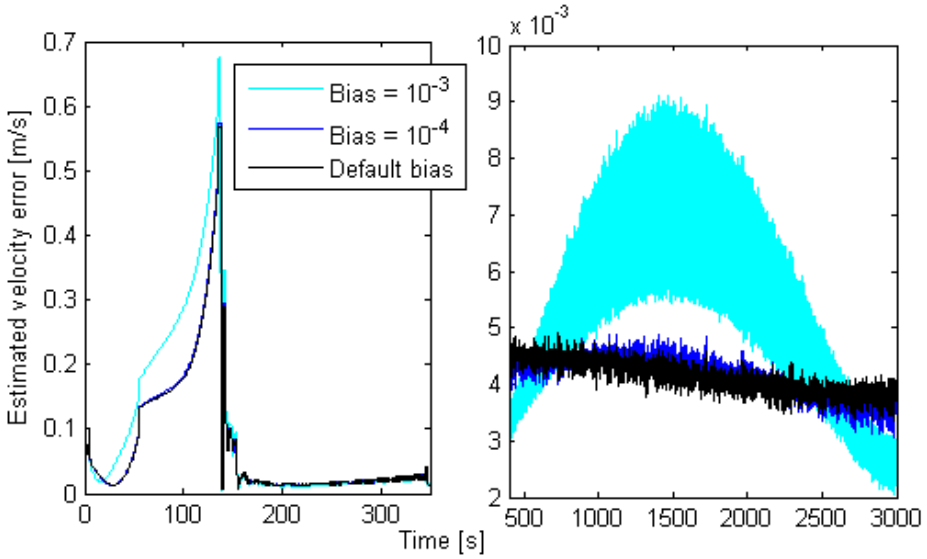

Figure 89: Estimated position error as a function of time and of the accelerometer bias error (consult Annex B for further information concerning the simulations). The figure has been divided in two parts in order to show the results before and after the velocity update. The bias error values detailed in the legend are expressed in m/s^2.

The accelerometer bias can have severe consequences on the first 200 seconds of the trajectory. Nonetheless, the velocity corrections reduce significantly the effect of the bias on the estimations. As a consequence, sensors that are not currently used for navigation because the bias uncertainty increases with time, could be used in hybrid navigation systems.

8.3.2 Gyroscopes bias error

The gyroscope bias error is more difficult to correct than the accelerometer bias error because in the model of this project the attitude is not corrected with GNSS data.

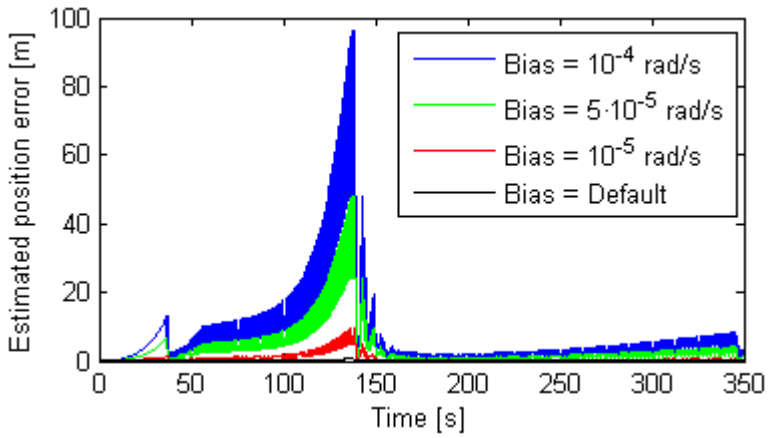

Figure 90: Estimated position error as a function of time and of the gyroscope bias error (consult Annex B for further information concerning the simulations). The figure limits to the first 350 seconds of the trajectory.

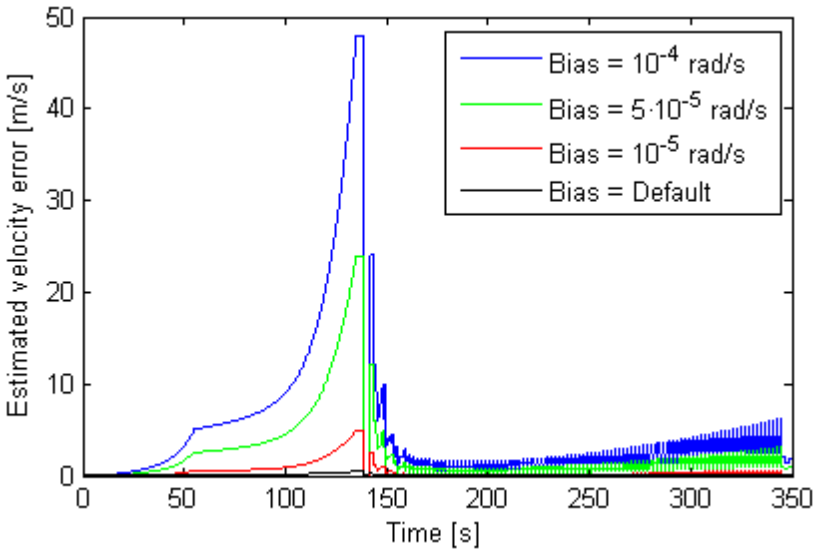

Figure 91: Estimated position error as a function of time and of the gyroscope bias error (consult Annex B for further information concerning the simulations). The figure limits to the first 350 seconds of the trajectory.

Figure 90 and Figure 91 show that the gyroscope bias error increases considerably the error of the first 350 seconds of the trajectory. As the attitude estimation error increases with time as a consequence of the bias, the estimation error increase rate increases with time. This effect can be seen in Figure 92, where the estimation errors are plotted in the intermediate trajectory segment. This analysis should be revised in later design phase because the attitude may be corrected with GNSS data. If the attitude corrections are not implemented in the final navigation algorithm, the gyroscope bias will be one of the most important sensor specifications.

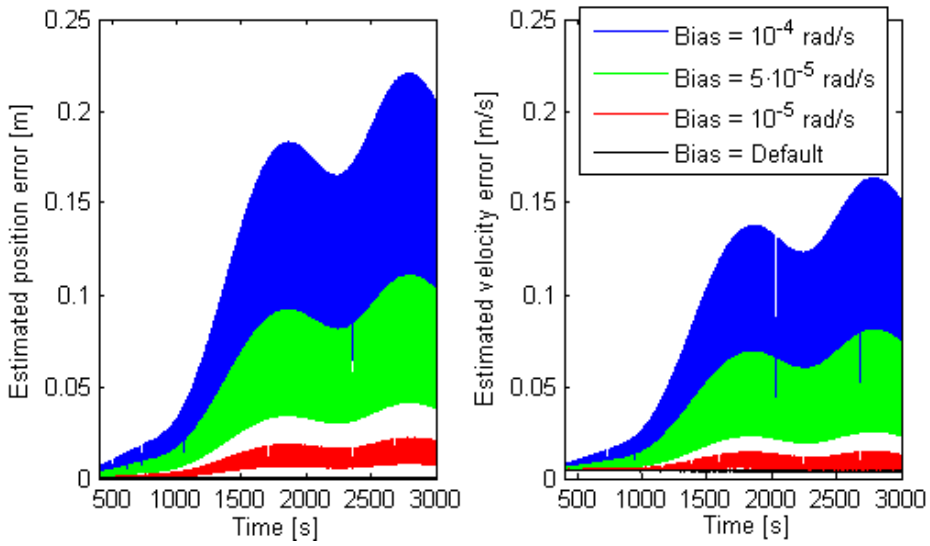

Figure 92: Estimated position and velocity errors as a function of time and of the gyroscope bias error (consult Annex B for further information concerning the simulations). The figure refers to the intermediate trajectory.

8.4 Sensor scale factor error

The sensor scale factor is the last sensor parameter whose effects on the INS performance are evaluated. The scale factor error, just like the bias error, is intrinsic to the sensor calibration.

8.4.1 Accelerometers scale factor

The accelerometer scale factor error produces an estimated trajectory error. The trajectory segment where this error is bigger is just before the first velocity correction.

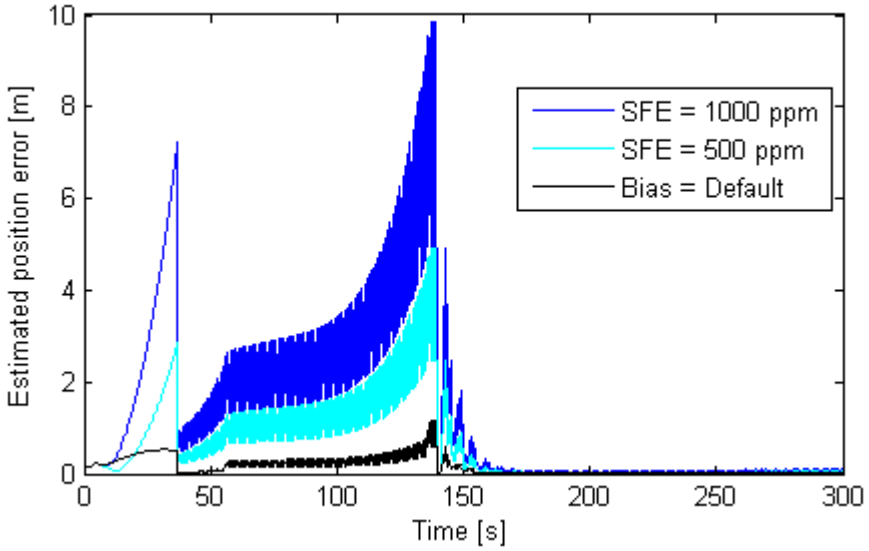

Figure 93: Estimated position error as a function of time and of the accelerometer scale factor error (consult Annex B for further information

concerning the simulations). The figure focuses on the first 300 seconds of the trajectory.

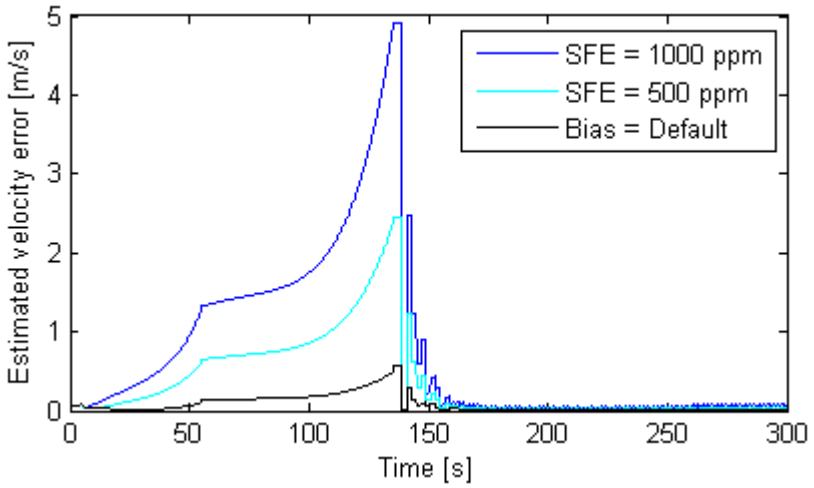

Figure 94: Estimated velocity error as a function of time and of the accelerometer scale factor error (consult Annex B for further information concerning the simulations). The figure focuses on the first 300 seconds of the trajectory.

The effect of the scale factor error is negligible at the trajectory segment where the velocity is corrected and the launcher motors are not operating. The reasons why the scale factor effect is negligible is that the accelerometers input is null and that the previous estimated velocity errors produced by the scale factor are mainly removed by the velocity correction.

8.4.2 Gyroscopes scale factor

The gyroscope scale factor error has an effect similar to the gyroscope bias error, which is an attitude error that increases the estimated trajectory errors increase rate. As a consequence, the estimated trajectory error at the end of the trajectory has the same shape as in Figure 92. However, it does not have the same magnitude because the consequences of the scale factor error are smaller than those corresponding to the bias error. This fact can be seen in Figure 95 and Figure 96, where the trajectory errors are shown as a function of time and of the gyroscope scale factor error.

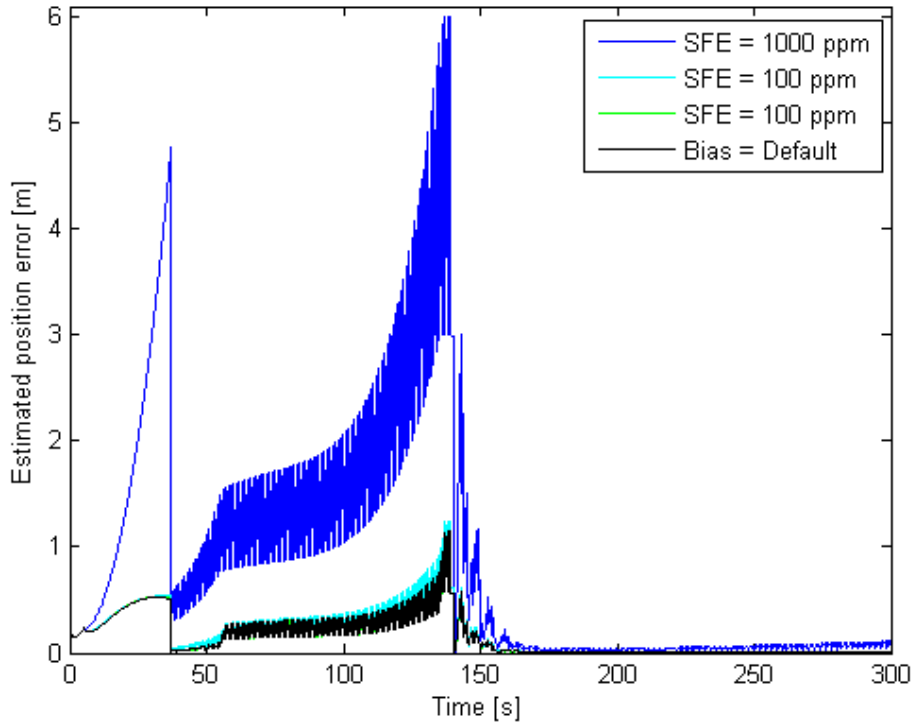

Figure 95: Estimated position error as a function of time and of the gyroscope scale factor error, SFE (consult Annex B for further information concerning the simulations). The figure focuses on the first 300 seconds of the trajectory.

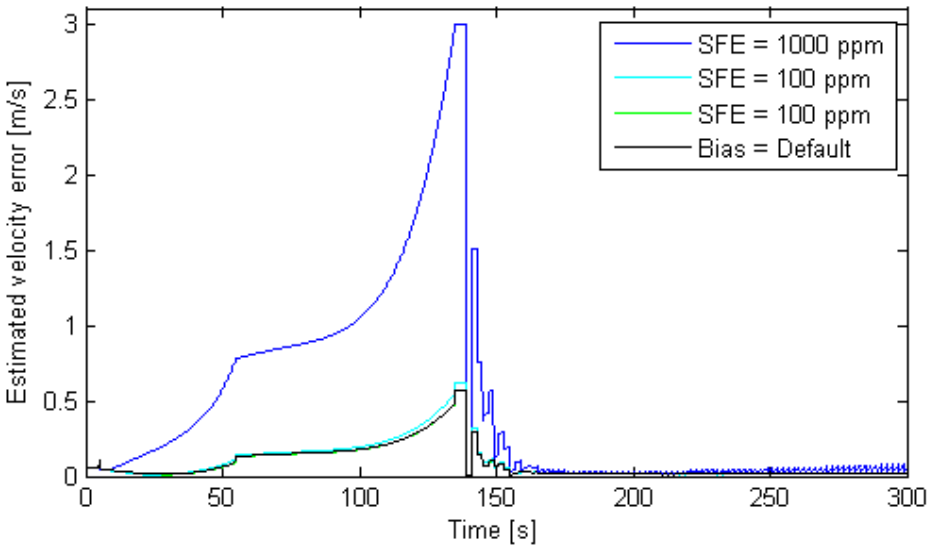

Figure 96: Estimated velocity error as a function of time and of the gyroscope scale factor error, SFE (consult Annex B for further information concerning the simulations). The figure focuses on the first 300 seconds of the trajectory.

8.5 Inertial navigation system frequency

As illustrated in section 6.4 , an increase in of the INS frequency reduces the estimation error produced by high acceleration or turn rate changes.

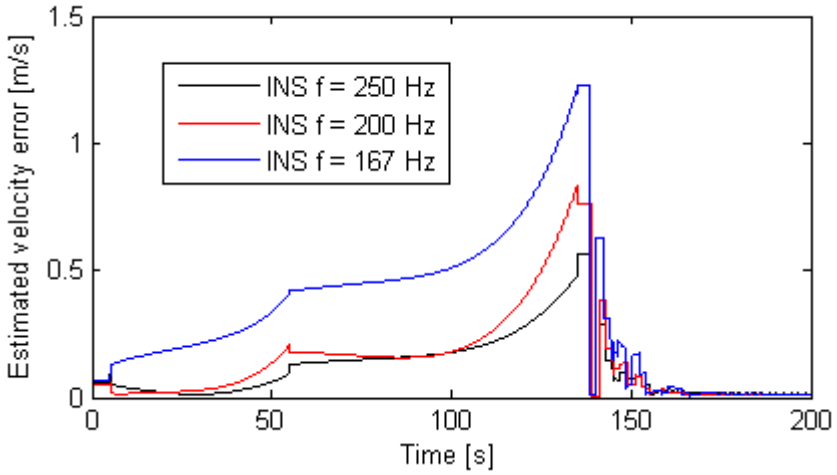

Figure 97: Estimated velocity error as a function of time and of the INS frequency. The calibration errors have been changed between simulations (consult Annex B for further information concerning the simulations). The figure focuses on the first 200 seconds of the trajectory.

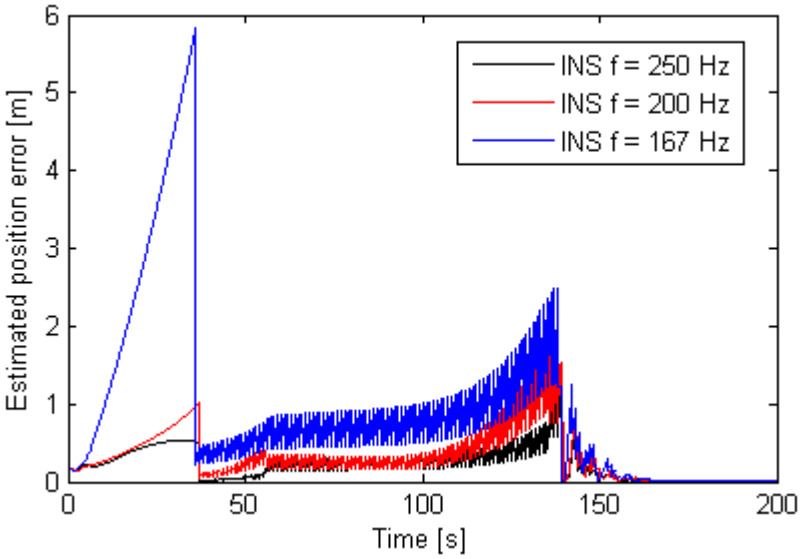

Figure 98: Estimated velocity error as a function of time and of the INS frequency. The calibration errors have been changed between simulations (consult Annex B for further information concerning the simulations). The figure focuses on the first 200 seconds of the trajectory.

As it can be seen in Figure 97 and Figure 98, 200 Hz is a proper frequency to use in the INS because frequency slightly increases the precision. However, if the frequency is reduced, the estimated trajectory error increase is significant.

8.6 Global navigation satellite system frequency

The effect of the GNSS frequency on the navigation performance is that the position and velocity updates are performed less frequently. The tested GNSS frequencies are all above 1Hz. The GNSS frequency of the Aldebaran launcher will be between 0.33 and 1 Hz [28].

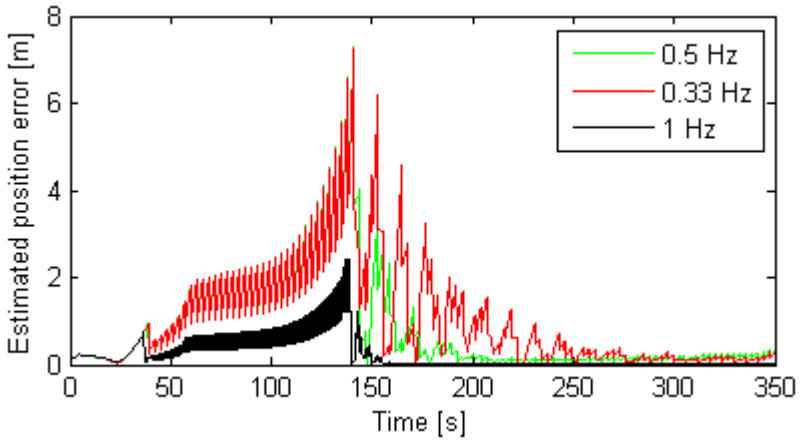

Figure 99: Estimated position error as a function of time and of the GNSS frequency (consult Annex B for further information concerning the simulations). The figure focuses on the first 350 seconds of the trajectory.

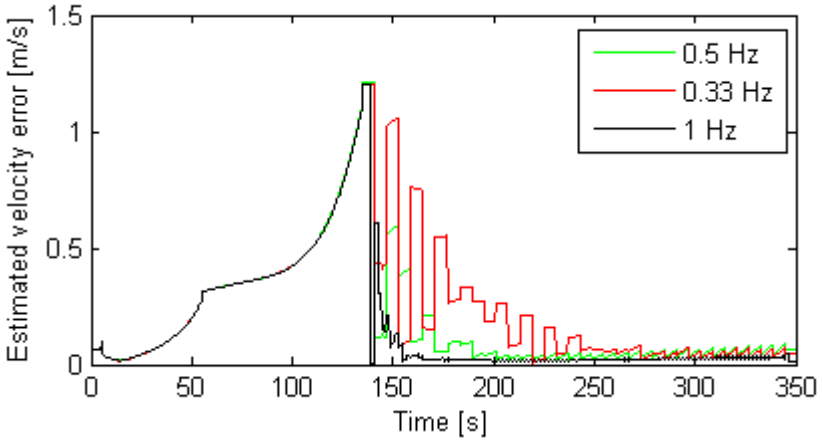

Figure 100: Estimated velocity error as a function of time and of the GNSS frequency (consult Annex B for further information concerning the simulations). The figure focuses on the first 350 seconds of the trajectory.

Figure 99 and Figure 100 show the performance of the INS as a function of the GNSS frequency. There are no appreciable differences between 0.5 and 0.3 Hz before the velocity correction. When the velocity is corrected, the 0.5 Hz result is slightly better. Nonetheless, the two frequencies imply INS performance degradation.

9 Conclusions

This study has modelled and analysed the performance of an inertial measurement unit on board a launcher. The model is particularized for the case of the Aldebaran launcher. Aldebaran is a system demonstrator. Its main objective is to be a commercial launcher and to promote, help and test the subsystem's improvements that should allow the design of the European next-generation launch vehicles. The developed model can be used to determine the inertial sensor requirements for a given mission. In this study the performance of the GNSS has not been modelled, because it is out of scope.

Sections 1 Justification and 3 describe the Aldebaran project and the relevant characteristics of the Aldebaran launcher. In section 3.2 , the reasons why is needed to model a hybrid navigation system are detailed. The main decisions regarding the design of the model have been detailed in sections 5.1 and 6.1 . The first action is the definition of the trajectory which has been divided into segments. In each segment the trajectory has been modelled by a specific function whose parameters have been adjusted boundary conditions.

The random error has been modelled with a dynamical model because the use of the modified Allan Variance method in some MEMS inertial sensors is still under study. Although the gravity model to be implemented is a requirement of the project, the effects of the gravity model on the INS performance have been analysed. A spherical harmonic expansion truncated at the truncated at the J2 zonal term has been found valid in the case of INS-GNSS hybridization. Without hybridization, the estimated gravity error causes the estimated position error to increase with time. Furthermore, the vertical channel instability makes the error grow more rapidly. The use of an external sensor aiming at reducing the vertical channel instability has been analysed and the conclusion drawn is that its implementation is not advisable The reasons are that the INS-GNSS hybridization reduces a lot the impact of the instability on the estimations and that the implementation of a new sensor affects the mass, volume and power budgets.

Section 7.1 describes the tests carried out in order to validate the model and illustrates the results of these tests. The model has been validated by means of three sets of tests. The first set of tests has validated the INS attitude performance by comparing the 'ideal' simulation results with the real attitude and by comparing the sensitivity to some parameters with the expected performance. The second set of tests has validated the INS trajectory performance. These tests consist in introducing a real launcher measured trajectory in the model and

performing some sensitivity analysis. The INS-GNSS validation is carried out by analysing the results of different types of integrations. The hybridization implemented in this model is an uncoupled system integration with position and velocity update, which has been found appropriated because it has more advantages than drawbacks, such as the hybridization cost.

The results presented in Section 8.1 show that an aerial launch can have severe consequences on the performance of navigation systems based exclusively on an INS. The initial position and velocity errors can have severe consequences on the navigation performance. However, when the position and velocity are updated, the errors are reduced rapidly. On the other hand, initial attitude errors cannot be reduced. However, their impact on the position and velocity estimations depends on the magnitude of the acceleration and the initial deviation. The largest benefits of using GNSS data for updating the position and velocity estimates lies in the fact that the maximum error before the corrections is, in most cases, orders of magnitude bigger than the maximum error when correcting velocity and position. The velocity correction with GNSS data is not applied in the model until t=137s. The reason is that large accelerations or attitude changes lead to INS instabilities; the navigation algorithm overcorrects the velocity error. The start time for applications of velocity corrections should be optimised once the trajectory definition has been improved.

Finally, the frequency sensitivity of the model has been analysed. The tested frequencies are similar to the Ariane V frequency (200 Hz) because the ISAs acquisition frequencies are defined by the ISA supplier. Usually, ISAs have two acquisition frequencies, the fast and the slow configuration. The fast configuration is usually around 200 Hz [22] [23] [25]. Due to the fact that increasing the frequency does not improve significantly the INS performance and that decreasing it degrades considerably the INS performance, it can be stated that 200 Hz may be a suitable frequency for the Aldebaran launcher. With the final trajectory a study on the INS frequency should be made in order to optimize the INS precision and the computational efforts.

Finally, the effects on the performance of the GNSS frequency have been analysed. The GNSS frequencies tested are 1, 0.5 and 0.33 Hz. The GNSS frequency of the Aldebaran launcher s expected to lie in this range[28]. The results show that the INS performance is similar in the 0.5 and 0.33 Hz case, but they are significantly worse than in the 1 Hz case. The degradation of the performance is important in this sensitivity analysis because the GNSS data is important to correct other parameters values.

In this project, we have implemented and validated an INS model in Simulink for the Aldebaran launcher. This model is the cornerstone of a brand new navigation system model that will evaluate the performance of navigation systems in a wide range of conditions and sensors.

10 Budget of the project

This section deals with the budget of the realization of the project “Study of the performance of an inertial measurement unit on board a launcher”. The budget has taken into account the software and the hardware employed and the author’s working hours. In this budget taxes are not taken into account.

GTD estimated the project working time in 800 man-hours, equivalent to 5 months. However, for several reasons, the final total number of hours is 850. Taking into account an average cost of 15€ per engineering work hour, the associated cost amounts to 12750€.

The hardware used is a laptop ASUS A55V. It has been used during 5.5 months, and its amortization period is 4 years.

The commercial software employed includes CATIA and Matlab®. CATIA has been used during one week, while Matlab® during three months. The version of CATIA version is *CATIAv5R17 & Abaqus® Student Edition*, whose use is free of charge because the author is a UPC student.

All the hardware and software costs are summarized in Table 14.

Element	Unit cost [€]	Amortization period [years]	Used period [months]	Estimated cost [€]
ASUS A55V	750	4	5.5	86
Matab®	100	1	3	25
CATIA	0	1	0.25	0
Microsoft Office Home & Student 2013	107	1	5.5	49
			TOTAL	160

Table 14: Cost of the software and the hardware used.

Table 15 summarizes all the project costs.

Element	Cost [€]
Engineering work cost	12750
Software	74
Hardware	86
TOTAL:	12910

Table 15: Summary of the project budget.

11 Acknowledgements

This work would not have been possible without the collaboration, guidance and patience of many people who has accompanied me through this project and through my university degree. This is why I want to address a few words to thank them their support.

I wish to thank Gisela Detrell and Elena Fantino for the guidance, monitoring and constant encouragement throughout the course of this project. I really appreciate their support; they have dedicated an enormous amount of time to help me improving this project.

I would also like to thank GTD for proposing this project. It has been really interesting to contextualize the model developed in the Aldebaran project.

Finally, I would also like to thank my family and my friends for their endless patience and confidence with me. I would like to specially mention Roser, for her support during all the tough times.

12. REFERENCES

Related to Aldebaran project:

1 Eric Louaas, Christophe Talbot, Joseph Berenbach (CNES), Pilar Gonzalez Gotor, Alejandro Ruiz Merino (CDTI), Jose Longo, Martin Sippel, Ludger Froebel (DLR), *ALDEBARAN: A "system" demonstrator for new generations of space transportation, now entering in the phase A*, IAC-09-D2.6.7

2 *GTD: Onboard Software Capabilities*, GTD, 2013.

3 Ludger Froebel (DLR), Christophe Talbot, Eric Louaas (CNES), Pilar Gonzalez Gotor, Alejandro Ruiz Merino (CDTI), *Aldebaran, A launch vehicle System Demonstrator*, presentation

4 Christophe Talbot, Eric Louaas (CNES), Pilar Gonzalez Gotor, Alejandro Ruiz Merino (CDTI), Ludger Froebel (DLR), *"ALDEBARAN", A launch vehicle System Demonstrator*, AIAA-RS7-2009-1005

5 Martin Sippel, Anna Lang, Etienne Dumont, Jens Gerstmann, Segio Montenegro (DLR), *Advanced Technology Upper Stages for Future Launchers*, IAC-10-D2.3.1

6 Farid Gamgami (DLR), *A trendsetting Micro-Launcher for Europe*

7 C. Talbot, C. Bonnal (CNES), *Air Launch Solutions for Microsatellites*

8 Joseph BERENBACH (CNES), *The Future Launchers Preparation*

Related to Ariane:

9 *Ariane 5 User's Manual*, Issue 5, Revision 1, Arianespace, July 2011

10 Jaques Breton, François Marquesene (Arianspace), *The Ariane family of launchers.*

Related to other launchers:

11 *Pegasus User's Guide*, Release 7.0, April 2010, Orbital

12 *Minotaur IV, V, VI User's Gide*, Release 2.0, June 2013, Orbital

13 Air launch aerospace corporation official website (http://www.airlaunch.ru), last visited on 16/11/2013

14 A. Karpov, R. Ivanov, M. Kovalevsky (ALAC), *Air launch aerospace international project*

Related to sensor types and sensor characteristics:

A-1. D.H. Titterton, J.L. Weston, *Strapdown Inertial Navigation Technology*, Second Edition 2004

A-2 Anthony Lawrance *Modern Inertial Technology – Navigation, guidance, and control*, Second edition, Springer, 1998

A-3 Mobinder S. Grewal, Lawrance R. Weill, Angus P. Andrews, *Global Positioning Systems, Inertial Navigation, and Integration*, Second Edition, Wiley, 2007

15 IEEE Standard 517, *IEEE standard specification format guide and test procedure for single-degree-of-freedom rate-integrating gyros*, 1974

16 BORTZ, J.E., *A new mathematical formulation for strapdown inertial navigation*, IEEE Trunsactions on Aerospace and Electronic Systems, 1971

17 SAVAGE, P.0, *Strapdown system algorithms*, AGARD Lecture Series No. 133: Advances in strapdown inertial systems, May 1984

18 Bin Fang, Xiaoqi Guo (Robotics Institute of Beihang University), *Modified Allen Variance Analysis on Random Errors of MINS*, 2013

19 Naser El-Sheimy, Haiying Hou, Xiaoji Niu, *Analysis and Modeling of Inertial Sensors Using Allan Variance*, IEEE Transactions on instrumentation and measurement , 2008

20 Dr. Walter Stockwell (Crossbow), *Angle Random Walk*

21 Steven Skiena, Department of computer Science State University of New York, *Lecture 9: Random Walk Model*, 2008

ISA datasheets:

22 Thales Avionics, *QUASAR 3000: Manuel d'utilisation et de maintenance*, A5E-MU-1432100B-101259 J14109AA (pages from 110 to 117)

23 CDL Inertial Engineering, *Minipos2 datasheet*, June 2012

24 Honeywell, E-SIGI Enhanced Space Integrated GPS/INS: INS with embed GPS Receiver and Mission Computer, June 2004

25 Honeywell, *SIGI Space Integrated GPS/INS: INS with embed GPS Receiver*, November 2000.

Related to earth models:

26 EUROCONTROL and IfEN, *WGS 84 Implementation Manual*, Version 2.4, February 12, 1998.

Information provided by GTD, Ingeniería de Sistemas y de Software, S.A.:

27 Eduard Diez Lledó (GTD), personal communication, 26/09/2013

28 Eduard Diez Lledó (GTD), personal communication, 09/12/2013

29 Eduard Diez Lledó (GTD), personal communication, 17/02/2014

30 Eduard Diez Lledó (GTD), personal communication, 20/02/2014

31 Eduard Diez Lledó (GTD), personal communication, 27/02/2014